Influence of oxygen annealing on structural and transport properties of pristine and $BaHfO_3$ nanocomposite $GdBa_2Cu_3O_{7-\delta}$ films

zur Erlangung des akademischen Grades eines

Doktors der Ingenieurwissenschaften (Dr.-Ing.)

von der KIT-Fakultät für Elektrotechnik und Informationstechnik
des Karlsruher Instituts für Technologie (KIT)

genehmigte

Dissertation

von

M. Sc. Ruslan Popov

aus Naberezhnye Chelny, Russische Föderation

Tag der mündlichen Prüfung: 17. Oktober 2022
Erster Gutachter: Prof. Dr. rer. nat. B. Holzapfel
Zweiter Gutachter: Prof. Alexey V. Pan, PhD

Kurzfassung

In den letzten Jahren hat sich gezeigt, dass beschichtete Leiter (CC), die eine supraleitende Hochtemperaturschicht enthalten, eine vielversprechende Lösung für die Entwicklung von Großanwendungen wie Motoren, Generatoren, Fehlerstrombegrenzern und supraleitenden Magnetspeichern darstellen. Eine der wichtigsten Voraussetzungen für solche Anwendungen ist die Fähigkeit, große Ströme bei verschiedenen Temperaturen und Magnetfeldern zu leiten. *RE*$Ba_2Cu_3O_{7-\delta}$ (*RE*BCO)-Supraleiter, insbesondere einer der ersten Vertreter dieser Familie, $YBa_2Cu_3O_{7-\delta}$, erfüllen diese Anforderungen, da sie hohe Übergangstemperaturen, hohe Übergangstemperaturen $T_c \approx$ 92-94 K und relativ große kritische Stromdichten J_c bei Flüssigstickstofftemperaturen besitzen, die typischerweise im Bereich von 2-6 MAcm^{-2} liegen.

Einer der Hauptvorteile von Supraleitern auf *RE*BCO-Basis, insbesondere in Form von Dünnschichten, ist das Vorhandensein einer großen Dichte von Defekten, die sich während des Wachstumsprozesses bilden. Diese Defekte sind verantwortlich für hohe J_c-Werte im Magnetfeld aufgrund der Wechselwirkung mit Flusslinien, die den Supraleiter in der "gemischten Phase" durchdringen. Daher besteht eine der Hauptstrategien zur weiteren Erhöhung von J_c darin, die Dichte der Defekte durch die Einführung von Sekundärphasen zu erhöhen, die als künstliche Pinning-Zentren bezeichnet werden.

Bei der gepulsten Laserabscheidung, der Methode für die Abscheidung dünner Schichten, die in der vorliegenden Arbeit verwendet wird, gibt es eine Vielzahl von Parametern wie Substrattemperatur (T_{sub}), Laserfrequenz (f), Sauerstoffdruck während der Abscheidung (pO_2) und Laserenergie (E_{las}), die im Mittelpunkt der Untersuchungen standen, wenn es um die Verbesserung der kritischen Stromdichten ging. In den letzten Jahrzehnten wurde gezeigt, dass eine kontrollierte Änderung der Abscheidebedingungen die Form und Dichte der Defekte in den *RE*BCO-Dünnschichten verändern kann. Daher widmet sich der erste Teil dieser Arbeit der Definition der optimalen Abscheidebedingungen für supraleitende $GdBa_2Cu_3O_{7-\delta}$ - Dünnschichten ohne und mit 2.5 Gew.% $BaHfO_3$ (BHO)-Nanopartikeln. Der Auswahlprozess basiert auf dem Vergleich von T_c, Kristallstruktur und Feldabhängigkeit von J_c bei verschiedenen Temperaturen. Für beide Systeme, das ursprüngliche und das BHO-Nanokomposit, sind T_{sub}=800 °C, f=10 Hz und pO_2=0,3-0,4 mbar optimale Wachstumbsbedingungen, die zu T_c-Werten im Bereich von 90-93 K und $J_c \approx$1.7-4.0 MAcm^{-2} führen.

Zusätzlich zu allen Abscheideparametern umfasst die Herstellung von supraleitenden *RE*BCO-Dünnschichten den Schritt der Sauerstoffglühung, der ebenso wichtig ist wie die Abscheidung selbst. In *RE*BCO-Supraleitern breiten sich die Ströme in den CuO_2-Ebenen

aus, und die Ladungsträger, in *RE*BCO Löcher, werden von CuO-Ketten bereitgestellt. Aus diesem Grund ist eine Sauerstoffglühung erforderlich, um eine ausreichende Sauerstoffdotierung zu erreichen und die supraleitende Phase zu bilden, da sich die REBCO-Dünnschicht unmittelbar nach der Abscheidung in der isolierenden Phase befindet. Obwohl verschiedene Aspekte des Sauerstoffglühens bereits ausgiebig untersucht worden sind, müssen noch einige Fragen geklärt werden. In der vorliegenden Arbeit versuchen wir, eines der Probleme bezüglich der Korrelation zwischen dem Sauerstoffglühverfahren, den Veränderungen der Defektmorphologie und den daraus resultierenden Transporteigenschaften zu beleuchten. Zu diesem Zweck betrachten wir zwei Systeme: unbehandeltes GdBCO und GdBCO+2.5 Gew.% BHO. Um den Einfluss der Sauerstoffglühung zu untersuchen, berücksichtigen wir vier Parameter: Glühtemperatur (T_{ann}), Glühzeit (t_{ann}), Sauerstoffdruck während der Glühung (PO_2) und Abkühlgeschwindigkeit (Q_{PLD}). Aufgrund der Unterschiede bei der Herstellung von GdBCO-Dünnschichten im Labor- und im Industriemaßstab vergleichen wir außerdem zwei Sauerstoffglühverfahren: *In-situ*-Sauerstoffglühen in der statischen Umgebung der PLD-Kammer und *Ex-situ*-Sauerstoffglühen im Ofen mit konstantem Sauerstoffffluss.

Bei der separaten Untersuchung jedes Parameters in einem unbehandelten und einem 2.5 Gew.% BHO-Nanokomposit-GdBCO-System konnten wir mehrere wichtige Merkmale beobachten:

1. T_{ann}: Beeinflusst in erster Linie die Stapelfehler in der GdBCO-Matrix. Beide Glühverfahren zeigen bei 450 °C (der niedrigste untersuchte T_{ann}) die höchsten J_c-Werte im Magnetfeld. Aufgrund der Einführung eines zusätzlichen Heiz- und Kühlschritts weisen die *ex – situ* geglühten GdBCO-Dünnschichten eine reichhaltigere Defektmorphologie auf und zeigen daher ein zweifach höheres J_c und F_p bei 10 K und 14 T.
2. t_{ann}: *Ex – situ* – geglühte GdBCO-Dünnschichten zeigen keine drastischen Abhängigkeiten der Struktur- und Transporteigenschaften von t_{ann}, während *in – situ* – geglühte Schichten mindestens 15 Minuten Glühzeit benötigen, um ein T_c über 77 K zu erreichen.
3. PO_2: Beeinflusst in erster Linie die Größe der Gd-reichen Nanopartikel in der GdBCO-Matrix.
4. Q_{PLD}: Höhere Abkühlraten führen zur Erhaltung von Stapelfehlern, wodurch möglicherweise Abkürzungen der Diffusionspfade bei der Sauerstoffglühung entstehen, die zu einem höheren J_c-Wert im Magnetfeld führen.
5. T_{ann} für *ex – situ* geglühtes GdBCO+2.5 Gew.% BHO: die BHO-Nanokomposit-GdBCO-Dünnschichten zeigen die höchsten J_c-Werte im Magnetfeld bei T_{ann}=700 °C.

Auf der Grundlage dieser Merkmale schlagen wir ein Modell vor, das die Glühparameter und die Mikrostruktur der GdBCO-Dünnschicht miteinander in Beziehung setzt. Nach diesem Modell können zwei Szenarien verwendet werden, um die Defektmorphologie und damit die Transporteigenschaften anzupassen:

1. Hohe T, hohe PO_2 mit anschließender Abkühlung auf Raumtemperatur: Dieser Weg bewahrt die in der GdBCO-Matrix vorhandenen Stapelfehler und reduziert die Dichte der Gd-reichen Nanopartikel.
2. Hohe T, niedrig PO_2 mit anschließender Abkühlung auf Raumtemperatur: Dieser Weg erhält die Gd-reichen Nanopartikel und reduziert die Dichte der Stapelfehler.

Abstract

In recent years, coated conductors (CC) containing a high – temperature superconducting layer have been shown to be a promising solution for the development of large-scale applications such as motors, generators, fault current limiters, superconducting magnetic storage devices. One of the major requirements for such applications is the ability to carry large currents at various temperatures and magnetic fields. *RE*$Ba_2Cu_3O_{7-\delta}$ (*RE*=Rare Earth, *RE*BCO) superconductors, in particular one of the first representatives of this family, $YBa_2Cu_3O_{7-\delta}$, meet these requirements since they possess high transition temperatures $T_c \approx$ 92-94 K and relatively large critical current densities J_c at liquid nitrogen temperatures, which are usually in the range 2-6 MAcm^{-2}.

One of the main advantages of *RE*BCO-based superconductors, especially in the form of thin films, is the presence of a large density of defects, which form during the growth process. These defects are responsible for high in-field J_c values due to the interaction with flux lines penetrating the superconductor in the "mixed phase". Therefore, one of the main strategies to further increase J_c is to increase the density of defects by introducing additional secondary phases, which are called artificial pinning centers.

Pulsed laser deposition, the main method for thin film growth used in the current work, has a variety of parameters such as substrate temperature (T_{sub}), laser frequency (f), oxygen pressure during deposition (pO_2), and laser energy (E_{las}), which were the main focus of the studies when it comes to improving critical current densities. In the last decades it was shown that a controlled change of deposition conditions can modify the shape and density of defects present in the *RE*BCO thin films. Therefore, the first part of this work is dedicated to determining the optimum deposition conditions for pristine and 2.5wt% $BaHfO_3$ (BHO)-nanocomposite $GdBa_2Cu_3O_{7-\delta}$ superconducting thin films. The selection process is based on comparison of T_c, crystal structure, and field dependence of J_c at various temperatures. In both systems, pristine and BHO nanocomposite, T_{sub}=800 °C, f=10 Hz and pO_2=0.3-0.4 mbar are optimum growth conditions, which resulted in T_c values in the range 90-93 K and $J_c \approx$1.7-4.0 MAcm^{-2}.

In addition to all deposition parameters, the preparation of *RE*BCO superconducting thin films includes an oxygen annealing step, which is as important as the deposition itself. In *RE*BCO-based superconductors, the currents propagate in the CuO_2-planes and charge carriers, in case of *RE*BCO holes, are provided by CuO-chains. Therefore, oxygen annealing is required to induce a sufficient oxygen doping level and form the superconducting phase, since right after the deposition, the *RE*BCO thin film is in the insulating phase. Even though various aspects of oxygen annealing have been extensively studied, few

questions still need to be addressed. In the current work, we attempt to shade a light on one of the problems regarding the correlation between the oxygen annealing procedure, changes in defect morphology, and resulting transport properties. To do so, we consider two systems: pristine GdBCO and GdBCO+2.5wt% BHO. To study the influence of oxygen annealing, we take into consideration four parameters: annealing temperature (T_{ann}), annealing time (t_{ann}), oxygen pressure during annealing (PO_2), and cooling rate (Q_{PLD}). In addition, due to differences in production of GdBCO thin films on lab and industrial scales, we compare two oxygen annealing approaches: *in-situ* oxygen annealing in the static environment of PLD chamber and *ex-situ* oxygen annealing in the furnace with constant oxygen flow.

Studying oxygen annealing in pristine and 2.5wt% BHO-nanocomposite GdBCO, we observed several important features on how each annealing parameter is modifying the defects:

1. T_{ann}: Predominantly affects the stacking faults in the GdBCO matrix. Both annealing approaches show the highest in-field J_c for 450 °C (the lowest T_{ann} investigated). Due to the introduction of additional heating and cooling steps, the *ex-situ* oxygen annealed GdBCO thin films have a richer defect morphology and, therefore, exhibit 2 times higher J_c and F_p at 10 K and 14 T.
2. t_{ann}: *Ex-situ* annealed GdBCO thin films do not show drastic dependencies of structural and transport properties on t_{ann}, while *in-situ* annealed films require at least 15 min of annealing to reach T_c above 77 K.
3. pO_2: Primarily affects the size of Gd-rich nanoparticles present in the GdBCO matrix.
4. Q_{PLD}: Higher cooling rates lead to the preservation of stacking faults, thus, possibly creating short cuts for oxygen diffusion during annealing and resulting in a higher in-field J_c.
5. T_{ann} for *ex-situ* annealed GdBCO+2.5wt% BHO: Compared to *ex-situ* annealed pristine GdBCO, BHO nanocomposite GdBCO thin films show the highest in-field J_c at T_{ann}=700 °C.

Based on these features, we propose a model that correlates the annealing parameters and the GdBCO thin film microstructure. According to this model, two scenarios can be used to tailor the defect morphology and, thus, the transport properties:

1. High T, high PO_2 annealing with consecutive cooling to room temperature: This path preserves the stacking faults present in the GdBCO matrix and reduces the density of Gd-rich nanoparticles.
2. High T, low PO_2 annealing with consecutive cooling to room temperature: This path preserves Gd-rich nanoparticles and reduces the density of stacking faults.

Contents

List of figures

List of tables

List of abbreviations

LTS	Low Temperature Superconductor
HTS	High Temperature Superconductor
*RE*BCO	Rare-Earth Barium Copper Oxide, $RE Ba_2Cu_3O_{7-\delta}$
YBCO	Yttrium Barium Copper Oxide, $YBa_2Cu_3O_{7-\delta}$
GdBCO	Gadolinium Barium Copper Oxide, $GdBa_2Cu_3O_{7-\delta}$
LN_2	Liquid Nitrogen temperature, 77 K
LHe	Liguid Helium temperature, 4.2 K
T_c	Transition temperature or critical temperature
PLD	Pulsed Laser Deposition
CSD	Chemical Solution deposition
T_{sub}	Substrate temperature
v_{dep}	Deposition rate
f	Laser frequency
pO_2	Oxygen pressure (thin film deposition)
T_{ann}	Annealing temperature
t_{ann}	Annealing time
PO_2	Oxygen pressure (annealing)
O	Orthorombic phase (orthorombic-I and orthorhombic-II)
T	Tetragonal phase
D	Diffusion coefficient
ξ	Coherence length

λ	London penetration depth
F_L	Lorentz force
F_p	Pinning force density
I_c	Critical current
J_c	Critical current density
IL	Irreversibility line
SF	Stacking fault
NP	Nanoparticle
APC	Artificial pinning center
BHO	$BaHfO_3$
B*M*O	Ba*M*O_3 (*M*=Hf, Zr, Ti, Sn)
XRD	X-ray Diffraction
AFM	Atomic force microscope
TEM	Transmission electron microscope
SEM	Scanning electron microscope

Acknowledgements

It is good to have an end to journey towards;
but it is the journey that matters, in the end

Ursula K. Le Guin.

My journey…looking back…it definitely was not an easy one. Many downs…fewer ups…Now, when I look back on the path which I passed, I am truly astonished by what it gave to me and what was achieved.

Everything has started long ago at the Institute for Technical Physics. My journey would not have been possible without Prof. B. Holzapfel, this is why, I am truly grateful that you accepted me as your PhD student, guided me on my way, and at one of the most difficult times of my journey, the help you provided was inestimable. Another person, who had a significant impact on my success as a PhD student, is Dr. Jens Hänisch. Thank you for all your help, long fruitful discussions, and your guidance. This journey could not have been pleasant without the people I met on my way…Roland, Tara, Shahab, Fabian, Nicolo, Pablo...I thank you from all my heart for bringing the joy on my path, especially Nicolo and Pablo. Nicolo, I think I will be remembering for a long time our beer tasting Saturdays. Pablo, countless nights I spent in the institute, doing measurements and trying to understand all the issues I had and countless mornings I spent in your office discussing all the possibilities, therefore, thank you for sharing your knowledge and helping me on my way. Institute for Technical Physics was my Alma Mater for all this time, and I would like to thank all wonderful people I met there: M. Erbe, S. Kauffmann-Weiss, K. Ackermann, M. Langer, S. Meyer, W. Freitag.

Now…my journey has come to an end and at this point, I would like to say that it would not be possible without the most important people in my life: my mother, Larisa Popova, I think you were constantly worried about me even more than I did, my father, Semen Popov, and my brother, Igor Popov. The journey was difficult, sometimes hardly bearable…but thank you for supporting me all these years. Without you, I would not be able to achieve my goals.

Karlsruhe, August 2022

Ruslan Popov.

1 Introduction

In 1911, a sharp drop within a few hundredths of a degree in the resistance of a mercury sample was discovered by the Dutch physicist H. Kammerligh-Onnes [1]. This new state of matter he later called "superconducting", thus, starting a new era in solid-state physics. Extensive search for superconductivity in the upcoming years has led to a discovery of the superconducting state in various metallic materials such as Pb, Sn, Al, Nb and many others.

Later, in 1933, W. Meissner and R. Ochsenfeld found that superconductors placed in an external magnetic field have the ability to completely expel it [2], thus, making superconductors not only a perfect conductor but also giving it perfect diamagnetic properties. In the upcoming years, other phenomena such as isotope and Josephson effects were observed. However, only in 1957, a microscopic theory of superconductivity [3], which is referred to as BCS theory of superconductivity, was developed. For this, Bardeen, Cooper and Schriffer received the Nobel Prize in 1972. According to BCS theory, electrons, during transition to the superconducting state, form new quasiparticles via phonon interaction, which is called Cooper-pairs.

After many years of stagnation, another breakthrough in the search for superconductivity appeared when in 1986 J. G. Berdnorz and K. A. Müller published their work on possible superconductivity above 30 K in a La-Sr-Cu-O compound [4]. Even though, at first, the scientific community was sceptical about this compound, when it was shown that La-Sr-Cu-O exhibits the Meissner effect, it created an explosive interest in the field of superconductivity. In 1987, C. W. Chu *et al*. [5] observed transition into the superconducting state at 92 K in an Y-Ba-Cu-O compound, thus, confirming the start of the new era of high-temperature superconductors which was founded by Berdnorz and Müller, due to the ability of operating at boiling temperatures of liquid nitrogen. The search for HTS materials has led to the discovery of $BiSrCaCu_2O_x$ with T_c of 105 K [6] and Tl-Ba/Ca-Cu-O with T_c up to 150 K [7] in 1988. In 1994, $HgBa_2Ca_2Cu_3O_{8+\delta}$ was discovered with transition temperatures around 135 K [8], which also could be increased up to 164 K by applying hydrostatic pressure [9], the record for a long time. Additionally, within the last decades it was shown that even conventional type superconductors such as MgB_2 can exhibit superconducting transition of 39 K. Nowadays, the record in T_c is held by carbonaceous sulfur hydride which goes into superconducting state at 288 K and 267 GPa of pressure [11].

Decades have passed since then, however, a theory which would explain the mechanism of HTS is still not established. Regardless of that, extensive research of $YBa_2Cu_3O_{7-\delta}$

(YBCO) and, *RE*$Ba_2Cu_3O_{7-\delta}$ (*RE*BCO, *RE*=Rare Earth)-based superconductors in general, has led to understanding of many electromagnetic and structural features of these compounds. *RE*BCO-based superconductors belong to the type-2 family. This family of superconductors, compared to type-1, at elevated magnetic fields go into the mixed or Shubnikov state, when the magnetic field is penetrating the superconductor in the form of quantized fluxes or Abrikosov vortices each bearing $\Phi_0=h/2e=2.07\cdot10^{-15}$ Wb magnetic field. Another feature of *RE*BCO-based superconductors is related to the structural variations during the preparation. For example, in case of *RE*BCO-based superconducting thin films, a large variety of defects is formed during thin films deposition, which in turn participate in flux pinning and prevent the Lorentz force from moving fluxes, which causes the current dissipation. Therefore, a large variety of growth-related defects are crucial for increasing the critical currents of the superconductors.

High T_c (higher than LN_2) and J_c are two of the main parameters that attracted attention of researchers around the world to *RE*BCO compounds. Nowadays, *RE*BCO-based superconductors have a high potential for such applications as motors, generators, fault current limiters and superconducting electronics. For engineering applications, especially coated conductors, I_c is one of the most important characteristics. I_c can be enhanced either by increasing the thickness of the superconducting layer or by increasing the J_c. Since J_c depends on the interaction of vortices with defects, within last decades many studies have shown that J_c can be increased 2-5 folds by introducing artificial pinning centers into the *RE*BCO thin film matrix [12-14]. Additionally, recent works have shown that the size, shape and distribution of these APCs can be modified by the deposition parameters [15], thus, allowing to tailor the desired pinning morphology for a certain application i.e., range in temperature, field and orientation. Regardless of the preparation conditions of *RE*BCO-based superconductors, another, possibly the most crucial, step is oxygen annealing. Oxygen annealing plays an important role, since after the deposition *RE*BCO has a tetragonal crystal structure and is an insulator. Therefore, oxygen annealing is required to introduce additional oxygen and form the orthorhombic phase, which is superconducting. Since the discovery of YBCO superconductors, the majority of studies regarding oxygen annealing issues were dedicated to oxygen diffusion in YBCO single crystals and thin films [16-19], the anisotropy of the diffusion coefficient and its dependence on annealing temperature [20-24], as well as oxygen stoichiometry and its correlation with T_c [25-27]. Another issue related to the oxygen annealing is understanding the phase stability and conditions for formations of the secondary phases acting as artificial pinning centers (APC). In recent years, phase diagrams of partial oxygen pressure versus inverse temperature (pO_2-1/T) for YBCO and GdBCO thin films were defined [27, 29]. However, during more than 30 years of research on *RE*BCO-based superconductors, questions about the correlation between oxygen annealing parameters and defects morphology and, thus, resulting transport properties, have remained open. Attempts to shed light on this issue were the main motivation for this doctoral research.

This doctoral thesis mainly consists of 8 Chapters. Chapter 1 gives a brief history of superconductivity and motivation for this work. Chapter 2 is dedicated to the main phenomena in HTS as well as an overview of the recent studies on the *RE*BCO-based superconducting thin films. Chapter 3 presents the basics of pulsed laser deposition as well as the main characterization techniques such XRD, AFM and SEM, used for thin film characterization. Chapter 4 shows the results of our studies on influence of deposition conditions on structural and transport properties in pristine and $BaHfO_3$ nanocomposite GdBCO thin films. Chapters 5 and 6 show how the oxygen annealing parameters such as annealing temperature (T_{ann}), annealing time (t_{ann}) and oxygen pressure (PO_2) can modify the defect morphology during *in-situ* and *ex-situ* oxygenation of pristine GdBCO thin films and their influence on transport properties. Chapter 7 is dedicated to our studies on *ex-situ* oxygen annealing of $BaHfO_3$ nanocomposite thin films. Finally, the main conclusions of this work are summarized in Chapter 8.

2 Basics of high temperature superconductivity

$GdBa_2Cu_3O_{7-\delta}$ similar to $YBa_2Cu_3O_{7-\delta}$ belongs to the family of *RE*BCO-based superconductors and, therefore, in this chapter, based on the previous studies on YBCO compound, we will give an overview of the main structural features of GdBCO superconductors. Section 2.1 is dedicated to an introduction to the structure of GdBCO as well as the influence of rare earth ion size and oxygen content and its ordering on structural and superconducting properties. Section 2.2 gives a short overview of the magnetic properties, flux pinning and its influence on the transport properties. Section 2.3 presents which types of defects are present in *RE*BCO-based superconducting thin films as well as those which can be artificially introduced into its matrix.

2.1 *RE*BCO-based superconducting thin films

2.1.1 Influence of the rare earth ion size and crystal structure of GdBCO superconductors

Since the discovery of the superconducting transition at 92 K in $YBa_2Cu_3O_{7-\delta}$ by Wu *et al.* [31], extensive studies were done in order to identify the crystal structure of YBCO to get closer to understanding of the mechanism of superconductivity in these compounds. In addition to all investigations of YBCO crystal structure, scientists were also looking at possible rare-earth ion substitutions for Y and what effect it might have on the structural and superconducting properties. In 1987, H. Asano *et al.* [32] showed that independent of the rare-earth ion size, all *RE*BCO-compounds crystallize in an oxygen-deficient perovskite structure. Compared to YBCO, GdBCO has larger lattice parameters due to larger ionic radius. Later, in 1994, Y. Xu *et al.* [33] in their work on influence of Ga and Zn substitution in *RE*BCO-based superconductors have shown that the transition temperature has a slightly increasing linear dependence on the rare-earth radius. Due to the rapid development of different growth techniques, it was observed that compared to YBCO thin films, GdBCO can be considered to have several advantages and, therefore, based on these advantages GdBCO was chosen as a main material for studies of structural and superconducting properties in this doctoral research. According to the studies of K. Takahashi *et al*. [34], GdBCO have the following advantages:

a) With the increase of the film thickness, GdBCO shows much lower ratio of a-axis oriented grains compared to YBCO
b) As a results of the first advantage, with the increase of the film thickness from 200 nm up to 2 µm GdBCO usually exhibits 2 times larger self-field J_c than YBCO
c) GdBCO possesses a higher melting temperature, which in addition can provide better growth due to the absence of the large particles during the deposition.

As mentioned above, since GdBCO and YBCO belong to the same family of *RE*BCO-based superconductors and have similar crystal structure, the description of GdBCO is based in the previous studies on crystal structure of YBCO. GdBCO can be described as distorted, oxygen-deficient layered perovskite in the form ABO_3 [35-37]. In case of GdBCO, A cations are Gd and Ba, while B anions are Cu. The perovskite cubic unit cell is tripled along the *c*-axis and Gd and Ba are stacked in Ba-Gd-Ba sequence [38], with Ba atoms slightly shifted towards the centering Gd atom [35]. In GdBCO, Gd is coordinated to 8 oxygen atoms which form a square prism, and Ba is coordinated to 10. Due to such coordination, compared to ideal perovskite structure, GdBCO is oxygen-deficient. Oxygen is missing from the central Gd layer and from the *a*-axis in the basal plane. Additionally, while Gd and Ba have +3 and +2 valence respectively, Cu has a mixed valence of +2 and +3 (+2 in the Cu-O chains, +3 in the CuO_2 planes) to provide the charge neutrality. Therefore, in GdBCO there are 5 crystallographically independent oxygen sites. Cu(1) (valence +2) is located at the center of the rectangle formed by 2 O(1) and 2 O(4) atoms and forms Cu-O chains along the *b*-axis. Cu(2) is square-pyramidally coordinated with 2 O(2), 2 O(3) in the *a* and *b* plane and one O(4) along the *a*-axis [38, 40] and form CuO_2 sheets (see Fig. 2.1).

2.1.2 Tetragonal to orthorhombic phase transition of GdBCO

Shortly after the discovery of superconductivity at 92 K in YBCO, it was identified that the phase $YBa_2Cu_3O_{7-\delta}$ with δ varying between 0 and 0.2 is responsible for such high T_c. The crystal structure described in subsection 2.1.1 has an orthorhombic symmetry and belongs to P_{mmm} space group. However, extensive research on the YBCO compound showed that the crystal structure and superconducting properties are highly dependent on the oxygen content. In turn, oxygen content is dependent on the annealing parameters such as temperature, duration, oxygen pressure and quench rates. In the large variety of X-ray diffraction and neutron powder diffraction studies [37, 41-44], in order to identify the position of oxygen atoms, the oxygen content of YBCO was varied by annealing at various temperatures. J. Jorgensen *et al.* [41] in their studies of structural and superconducting properties of orthorhombic (O) and tetragonal (T) YBCO identified the structure for YBCO with $\delta \approx 0.3$-0.7. Additionally, the same group showed that YBCO annealed at

T_{ann}=700 °C [41] experiences an order-disorder transition in which disordering of oxygen atoms leads to the destruction of one-dimensional CuO chains. Moreover, they were able to determine that this transition depends on T_{ann} and PO_2, and most of the time, appears around 7-δ=6.5 stoichiometry. Due to such an order-disorder transition and removal of oxygen from Cu-O chains (O (1) sites), the symmetry of YBCO is changing from O to T with the space group $P_{4/mmm}$. In the same year, in the work on metamorphic phases of YBCO, Y. Nakazawa *et al*. [45-46] showed that it is possible to prepare YBCO with different crystal structures by varying T_{ann} and PO_2 with a quench following the oxygen annealing. They showed that with increasing T_{ann}, orthorhombic-I (O-I) YBCO first undergoes transition into orthorhombic-II (O-II) crystal structure due to oxygen out-diffusion [41], and then into T phase. One of the important features of T crystal structure (see Fig. 2.1) is the absence of O(1) oxygen sites, since oxygen is mostly removed from Cu-O chains.

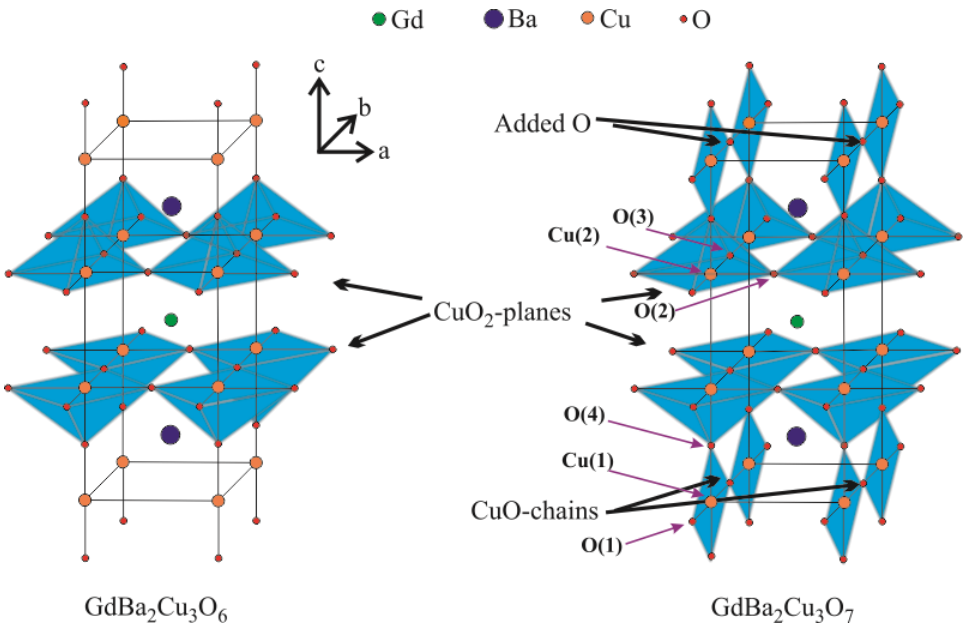

Figure 2.1: Crystal structure of $GdBa_2Cu_3O_6$ (T phase) and $GdBa_2Cu_3O_7$ (O-I phase).

One of the most prominent features, which appear during O-T transition is the change of the lattice parameters. J. Jorgensen *et al*. [41] as well as E. D. Specht *et al*. [47] have shown that during a set of transitions from O-I to O-II and O-II to T, which are controlled by T_{ann} and PO_2, the *c*-axis lattice parameter as well as the unit cell volume increase gradually with increasing T_{ann}, while *a* and *b* lattice parameters experience more drastic

changes. In the O phase, the *b*-axis lattice parameter is larger compared to the *a*-axis lattice parameter; however, at the transition to the T phase, both parameters equalize. Since the main parameters that control these variations in lattice parameters are temperature and oxygen pressure, the transition from O to T is also dependent on those. At low PO_2, the transition appears at lower T_{ann}, while higher pressures lead to the observation of the transition at higher T_{ann} [47]. Nevertheless, in most of the studies related to T-O phase transitions in YBCO, the O-to-T phase transition corresponds to $YBa_2Cu_3O_{6.5}$ with $\delta=0.5$ stoichiometry. This phase still exhibits orthorhombic symmetry and can be represented as 2 YBCO unit cells together, with O atoms missing on the border Cu-O chain of these 2 cells, meaning that only half of the Cu-O chains are filled.

2.1.3 Dependence of T_c and *c*-axis lattice parameter on oxygen content

In the previous subsection, we discussed the influence of oxygen content on the crystal structure of *RE*BCO-based superconductors on the example of YBCO. As mentioned above, the lattice parameters vary with the oxygen content, which will be thoroughly considered in this subsection. Another important feature related to oxygen content it is its influence on the superconducting properties of *RE*BCO-based superconductors.

In the studies on oxygen stoichiometry, R. J. Cava *et al.* [25] have shown that T_c has a non-monotonic dependence on the oxygen content. In particular, the $0<\delta<0.2$ range is characterized by a slight reduction of T_c with increasing δ. This region is quite often called "90 K – plateau". Increasing δ up to 0.3 leads to a rapid decrease of T_c with consequent plateau appearing for $0.3<\delta<0.5$, which is called "60 K – plateau". Further increase of δ brings another rapid decrease of T_c to 0 around $7-\delta=6.4$. A similar behavior to "90 K – plateau" in the range between $7-\delta=6.85-7$ has been observed by V. Breit *et al.* [48]. In their work, they attribute such changes in T_c to Cu-O chains, which act as charge reservoir in cuprate oxide superconductors. In a variety of studies of O-T transition in YBCO [41, 44] by neutron powder diffraction it was shown that with the reduction of oxygen content in YBCO, oxygen is mainly removed from Cu-O chains, which again indicates that Cu-O chains play a crucial role for the superconductivity in YBCO. According to these studies, superconductivity occurs mainly in 2 – dimensional CuO_2 planes. Metallic behavior of those results from the excess of charge holes, which are provided by the 1 - dimensional Cu-O chains. During oxygen out-diffusion, the unit cell of YBCO experiences a phase transition from O-I to O-II and consequently to T. Therefore, the 2 – plateau behavior, which appears in the oxygen-content dependence of T_c is related to the O-I and O-II phases. In some other studies [44, 49], the possibility of a larger variety of crystal structures, not only O-I and O-II, was suggested as a main reason for the reduction of T_c and the 2 plateaus. Additionally, the presence of the 2 – plateau behavior seems

heavily depend on the thermal history of the superconductor. For example, in the studies of quenched YBCO samples [50], such 2 – plateau behavior was not observed. Another group [28, 51] discovered that 2 – plateau behavior is present both in bulk samples and in thin films. Similar to changes of T_c at various δ, the same dependence is shown by the *c*-axis lattice parameter. As shown with XRD powder diffraction, the *c*-axis lattice parameter has a linear dependence on δ [43, 51, 52].

2.1.4 Oxygen diffusion in *RE*BCO-based superconductors

Since oxygen diffusion plays a crucial role both for the symmetry of the crystal structure and for the superconducting properties of *RE*BCO compounds, therefore, it is compulsory to understand the mechanism of oxygen diffusion in order to prepare the samples with the highest T_c as well as best transport properties. As mentioned in subsection 2.1.3, oxygen content and crystal structure are controlled by such annealing parameters as T_{ann}, t_{ann}, PO_2, and the quench rate from the annealing temperature. The majority of studies regarding oxygen diffusion are focused on defining the temperature dependence of the diffusion coefficient. 1 dimensional diffusion can be described by the 2nd Fick's law:

$$\frac{\partial}{\partial x}\left(D\frac{dC}{dx}\right)=\frac{\partial C}{\partial t} \tag{2.1}$$

where C – concentration of diffusing species, x – space coordinate, t – time of diffusion, D – diffusion coefficient [26]. The diffusion coefficient is measured as a time dependence of some property and describes a diffusion under a gradient of chemical potential. In this case, the sample is equilibrated under a certain oxygen pressure PO_2. Another possibility is the measurement of the tracer diffusion coefficient D^*, which describes diffusion in an absence of a gradient of chemical potential. D^* can be calculated from the fitting of the depth profile of ^{18}O from secondary-ion mass spectrometer (SIMS). Chemical diffusion and tracer diffusion coefficient are related as

$$D = D^*(1+\frac{\partial \ln\gamma}{\partial \ln c}) \tag{2.2}$$

where the expression in the parentheses is the thermodynamic factor and γ – activity coefficient of the diffusant.

Oxygen diffusion in single crystals and bulk ceramics:

Since *RE*BCO superconductors exhibit non-equivalent positions of oxygen in their crystal structure, it was of high importance to study if the oxygen diffusion exhibits anisotropic features. Bredikhin *et al*. [20] have shown in their studies on oxygen diffusion in single crystals that it is an anisotropic process. Investigation of oxygen diffusion by SIMS at

400 °C and 800 °C shows that at low temperature, the process is 2 – dimensional with a large difference in diffusion coefficients in *ab*-plane and *c*-direction. Depth fitting of SIMS profiles gave $D_{ab} = 3*10^{-12}$ cm^2s^{-1} and $D_c = 4*10^{-17}$ cm^2s^{-1} at 400 °C and at 800 °C $D_{ab}=7.8*10^{-9}$ cm^2s^{-1} and $D_c=6.2*10^{-11}$ cm^2s^{-1}. Such behaviour of the oxygen diffusion process they relate to the possibility that at low temperatures only oxygen in chains is exchangeable, while at high temperatures oxygen exchange appears via oxygen in chains combined with jumps to the oxygen sites in CuO_2 planes. Another important feature of oxygen diffusion in single crystals was observed by H. F. Poulsen *et al*. [53] in the work on bulk diffusion kinetics in YBCO. From neutron powder diffraction they were able to determine that O-I and O-II crystal structure have different domain sizes, which, as they suggest, can affect the oxygen in-diffusion at low temperatures, due to the complicated nature of the oxygen in-diffusion process, which includes surface reactions (adsorption, dissociation, migration) with diffusion along grain boundaries, microcracks, twin-domain boundaries and in the bulk. J. R. La Graff *et al*. [17, 54] discovered that the diffusion coefficient in YBCO depends on the oxygen concentration. By means of electrical conductivity measurements on a series of samples in the range 450 °C - 850 °C they showed that both in the single crystal and in polycrystalline specimen *D* was increasing with the increase of δ. In the consequent work on theoretical aspects of oxygen diffusion in YBCO single crystals [54], they have concluded that the concentration dependent oxygen diffusion results from defect-defect interactions, and oxygen diffusion is more favourable along *b*-axis. Additionally, even though the structural and superconducting properties are affected by the rare-earth ion size, M. Kläser *et al*. [55] have shown in their work on the oxygen diffusion in *RE*BCO single crystals that *D* is independent of the rare-earth ion size. Comparing time constants for in- and out-diffusion they concluded that the microstructure might have a bigger influence on *D*. Later, P. Diko *et al.* [56] confirmed this observation in their thermogravimetric studies of top-seeded melt-grown YBCO superconductors. Micro-cracks, which were appearing during the oxygenation process, showed to be responsible for shortening the necessary oxygenation time.

In addition to all experimental works which focus on the determination of the tracer or chemical diffusion coefficient also numerical studies were conducted. Most of the calculations of oxygen diffusion coefficients are based on the so called asymmetric next-nearest neighbour Ising model (ASNNNI). In this model, only diffusion in the Cu-O basal plane is taken into consideration since diffusion in ceramics has been shown to appear mostly via the *ab*-plane. Using Monte-Carlo simulations based on ASNNNI, E. Salomons and D. de Fontaine [57] have investigated the difference in the tracer and chemical diffusion coefficients. According to their studies, in basal plane of YBCO, diffusion of oxygen takes place via thermally activated jumps between neighbouring sites in the lattice. Additionally, they have shown that diffusion along Cu-O chains is the fastest, and interchange of atoms is the most important mechanism for oxygen diffusion. The ratio between diffusion along Cu-O chains and perpendicular to the chains has been

shown to be as large as 10. A similar method was used by A. Pekalski and M. Auslos [58], who showed that there is a clear difference in the tracer diffusion coefficient in the low and high temperature regions. This behaviour they related to the difference in the activation energies. In the low temperature region, due to long range order of YBCO, atoms have little energy, and the most probable way of diffusion is along *b*-direction, which corresponds to the conclusion of Ref. [26]. At high temperatures, ordering is worse or completely absent; combined with high energies available, oxygen can diffuse not only along Cu-O chains, but also by changing rows. J.-S. Choi *et al.* [59] have shown in their theoretical work several features that correspond well to the previous experimental works mentioned above. One of their main observations is that *D* is dependent on the oxygen density and long-range ordering: *D* increases with decreasing oxygen concentration in O phase, while in T phase *D* increases with increasing oxygen concentration. Both regions exhibit a sharp transition between each other. In the same work, they concluded twin boundaries have a drastic influence on oxygen diffusion, since at twin boundaries it is much faster than in bulk. This conclusion corresponds to the observation of H. Tuller *et al*. [16] that intrinsic disorder is the dominant source of mobile oxygen defects contributing to the oxygen diffusion.

Oxygen diffusion in thin films:

While in the bulk specimens oxygen diffusion appears to be a rather 2 – dimensional process, due to low *D* along *c*-axis direction and oxygen diffusion in and out predominantly along *ab*-plane, in thin films diffusion process have similarities and differences. W. A. M. Aarnink *et al*. [60] have shown in their studies on oxygen transport in *c*-axis oriented YBCO thin films that oxygen out-diffusion, similar to bulk superconductors, is a 2 – D process and no out-diffusion appears along *c*-axis direction. In their model of the diffusion process, thin films are assumed to have short circuits which in case of YBCO and *RE*BCO thin films can be present by growth spirals, screw dislocations, point defects and out-of-phase domains. These short circuits play an active role in the diffusion process. A. Michaelis *et al.* [19] discovered that oxygen out-diffusion is dependent on the film thickness, which indicates that it clearly has a bulk mechanism, while in-diffusion is independent of thickness and is more dominated by surface/grain boundary diffusion mechanisms. Even though results of [19] contradict those of [60], in case of [60] surface exchange has not been taken into consideration, and, possibly, consideration of different defects that act as short circuits affect the interpretation of the observed features. Later, L. Chen *et al.* [61] have shown that surface exchange kinetics have a high impact on the oxygen diffusion too. According to their model, the most probable diffusion pathways in YBCO can be either surface activation on the grains, diffusion along grain boundaries and then into the bulk, or activation on the grain boundaries and then diffusion into the bulk, similar to the previous path. After diffusion into the bulk, the bulk stoichiometry is adjusted accordingly by a rapid diffusion along the *ab*-plane. P. Cayado *et al.* [62], on the

example of CSD grown thin films, have shown that surface reactions are the limiting factor in the kinetics of oxygen exchange process. The model for oxygen diffusion reminds that of [61], with the difference that native surface and threading dislocations play a role of "chimneys" for oxygen. According to the studies of P. Cayado *et al.* [62], O_2 molecules are chemisorbed at the free surface, then molecules diffuse into existing defects leading to dissociation into O^{2-}. If ions are near the pores or dislocations, vertical diffusion into the bulk takes place, which is followed by the diffusion in the *ab*-plane.

Considering the diffusion mechanism in bulk samples and in thin films, it is clear that oxygen diffusion has a clear anisotropic behaviour with predominant diffusion along *ab*-plane; however, in case of thin films, in addition to the bulk diffusion surface exchange processes as well as the microstructure of the film play an important role.

Another important feature, related to the oxygen diffusion, are the thermal limitations. E. F. Span *et al*. [21] have shown that oxygen can diffuse into YBCO films for $T \geq 300$ °C, while at 200 °C no detectable amount was observed even after 200 min. N. Chikumoto *et al*. [63] acquired slightly different results, that already at 350 °C the oxygen mobility becomes very slow.

2.1.5 pO_2-$1/T$ phase diagram

Since the processing parameters of *RE*BCO-based superconductors are heavily influencing the final structural and superconducting properties, it is important to build the phase diagram besides the studies of the diffusion process, which would allow to control and improve the production processes. As mentioned in subsection 2.1.2 and 2.1.3, the oxygen content can be controlled by T_{ann} and PO_2 and hence the phase diagrams describing the changes in crystal structure and phase formation is pO_2-$1/T$, also regarding the thermally activated nature of diffusion. T. B. Lindemer *et al*. [27] analysed in studies of non-stoichiometry in YBCO available data in order to create a phase diagram for YBCO similar to E. D. Specht *et al*. [47] in their studies of the influence of oxygen pressure on the O-T transition. Such a phase diagram includes stability lines for the *RE*BCO compound, T-O-II transition line as well as O-II to O-I. Since GdBCO thin films are the main material used in the current work according to [29], the stability line for GdBCO can be divided into 2 regions:

1. 20-100 mTorr:

$$\log pO_2[\text{Torr}] = 10.85 - 13880/T[\text{K}] \tag{2.3}$$

Below this region, GdBCO thin films decompose into a mixture of Gd_2O_3 and liquid phase.

2. 1-10 mTorr:

$$\log pO_2[\text{Torr}] = 9.264 - 12150/T[\text{K}] \quad (2.4)$$

Below this line, GdBCO decomposes into a mixture of Gd_2O_3, $GdBa_6Cu_3O_y$ and liquid phases. Additionally, at the higher pressure regions, GdBCO decomposes into a mixture of Gd_2BaCuO_5 and liquid phases [29, 64].

2.2 Flux pinning in high temperature superconductors

2.2.1 Type-I and type-II superconductors

One of the most prominent characteristics of superconductors is their behavior in external magnetic field. Most of the elemental low temperature superconductors (LTS) belong to a group of type-I. These are characterized by the sharp transition to the normal phase when magnetic field exceeds a threshold field H_c. In 1957, based on the Ginzburg-Landau theory, Abrikosov [65] showed the possibility of another behavior, which he called type-II superconductors. The nature of superconducting material can be characterized by magnetic field penetration depth λ and coherence length ξ, distance at which a pair of charge carriers form the Cooper pair. Both these parameters are dependent on the temperature:

$$\lambda \sim (1 - T/T_c)^{-\frac{1}{2}} \quad (2.5)$$

$$\xi \sim (1 - T/T_c)^{-\frac{1}{2}} \quad (2.6)$$

According to the Ginzburg-Landau theory, the ratio of these 2 characteristics:

$$\kappa = \frac{\lambda}{\xi} \quad (2.7)$$

called “Ginzburg-Landau parameter” and superconductors follow the criteria:

$$if\ \kappa < \frac{1}{\sqrt{2}}, superconductor\ is\ type - I \quad (2.8)$$

$$if\ \kappa > \frac{1}{\sqrt{2}}, superconductor\ is\ type - II \tag{2.9}$$

Compared to type-I, which expels magnetic field till H_c, type-II superconductors exhibit the "Meissner effect" only till a smaller magnetic field H_{c1}. In fields higher than H_{c1}, type-II transitions into the "mixed phase". This, also called Shubnikov phase, is characterized by the penetration of magnetic field into the bulk of the superconductor in the shape of magnetic field quanta or "vortices". During further increase of magnetic field, the type-II superconductor transitions into normal phase at H_{c2} (see Fig. 2.2).

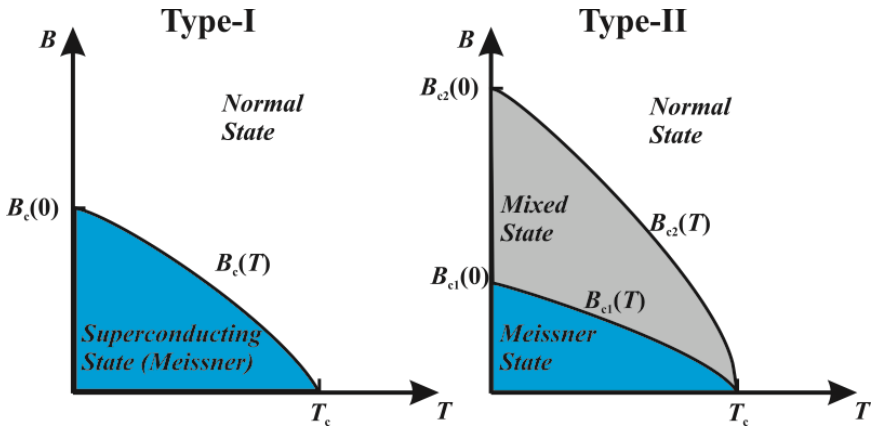

Figure 2.2: *B-T* phase diagram for type-I and type-II superconductors.

2.2.2 Vortices

Each flux line carries magnetic field flux of Φ_0=2.067·10^{-15} Wb and can be represented as a normal core of cylindrical symmetry elongated along external magnetic field and of size 2ξ (see Fig. 2.3). Around this cylinder, screening currents are flowing, and magnetic field created by these currents is directed along the cylinder and hence external magnetic field [66]. The density of superconducting electrons is reducing to 0 over the distance ξ, while the magnetic field increases from 0 to $2B_{c1}$ over distance λ. In type-II superconductors, penetration of vortices is energetically favorable, since due to existence of normal/superconducting interface, the free enthalpy is reduced. In addition, vortices in type-II superconductor form a hexagonal vortex lattice in the absence of the disorder. The density of vortices is increasing with increasing external magnetic field. Close to H_{c2}, the normal cores of the flux lines start to overlap, and superconductor goes into normal state [67-69].

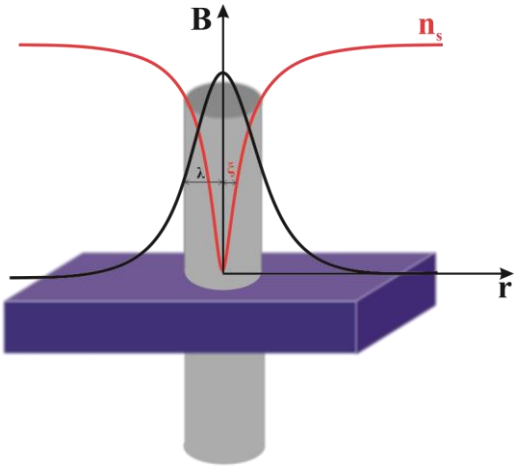

Figure 2.3: Visual representation of a vortex

2.2.3 Flux pinning and critical current density

One of the most interesting phenomena in type-II superconductors, when external field exceed H_{c1} and vortices start to penetrate a bulk of superconductor, is flux pinning. When an external current is applied to the vortex system, the flux lines move under Lorentz driving force. Lorentz force density and external current are related as:

$$\vec{F}_L = \vec{J} \times \vec{B} \tag{2.10}$$

Within perfectly homogeneous materials, the movement of the vortices is counteracted only by the friction force:

$$\vec{F}_\eta = -\eta \times \vec{v} \tag{2.11}$$

where v is the steady-state velocity of the vortex system. Therefore, in such system the dissipation appears due to finite electric field $\vec{E}$, which results from the flux motion [70].

$$\vec{E} = \vec{B} \times \vec{v} \tag{2.12}$$

From electric field and current density, we can define the power which is dissipated in the system and the dissipation-free superconducting current is lost. However, one of the advantages of HTS, in particular *RE*BCO-based superconductors, is the presence of large density of inhomogeneities and defects. Vortices interact with defects, and due to pinning

of the vortices, the dissipation-free superconducting current can be recovered. In this case, the driving Lorentz force is balanced by the average pinning force:

$$\overrightarrow{F_p} = \vec{J} \times \vec{B} \tag{2.13}$$

Such dissipation-free state exists only for $\overrightarrow{F_L} \leq \overrightarrow{F_p}$. Therefore, the critical current density J_c at which vortices are still pinned to the defects can be found from balancing F_p and F_L:

$$F_L = F_p, \qquad F_p = J_c \cdot B \rightarrow J_c = \frac{F_p}{B} \tag{2.14}$$

Equation of the Lorentz and pinning force densities, in order to describe properties of type-II superconductors, was first proposed by Bean [71] in his *critical state model*. Later, this model has become a basis for the description of flux pinning phenomena. The critical state can be presented as:

$$\overrightarrow{J_c}(B) \times \vec{B} = -\vec{F_p}(B) \tag{2.15}$$

Therefore, to describe the pinning mechanism it is required to define the pinning force density. The pinning force density can be presented as [72]:

$$F_p = \eta L f_p = -\eta L \Delta W / x \tag{2.16}$$

Where f_p – pinning force per unit length of pinned flux line, ΔW – work done in moving unit length of flux line from a pinning center to the nearest position, x – effective range of the pinning interaction, L – total length of flux line per unit volume that is directly pinned, η – efficiency factor. These quantities in equation (2.16) are influenced by several factors:

A) ***Nature of the pinning centers:*** The strength of interaction between vortex and pinning center (PC) depends on the difference in superconducting properties. If PC cause a small change in κ, then it is "$\Delta\kappa$ – pinning", while non-superconducting PC shows "normal pinning".

B) ***Wavelength of the microstructure:*** The situation, when the size and spacing exceeds λ, is referred as "magnetic interaction". In case, either size or spacing between PCs is lower than λ is referred as "core interaction". Not important for HTS due to large λ.

C) ***Size of the pinning center:*** PC can exceed the inter-vortex distance at several dimensions.

Based on the parameters, it is possible to determine behavior of the pinning force density and the mechanism of flux pinning.

2.2.4 *H-T* phase diagram

In HTS in the mixed phase, the state of flux lines is strongly dependent on their interaction with defects, one of the simple ways to describe the behavior of HTS at various fields and temperatures is *H-T* phase diagram. The phase diagram for *RE*BCO-based superconductors (see Fig. 2.4) has 3 main areas, which are common for all type-II superconductors:

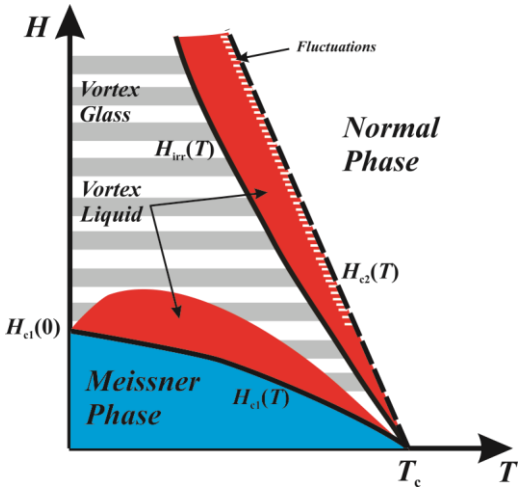

Figure 2.4: *H-T* phase diagram of *RE*BCO-based superconductor on the example of YBCO based on the results of [70].

1. Meissner phase ($H<H_{c1}$): the area at which magnetic field is expelled from the superconductor
2. Mixed phase ($H_{c1}<H<H_{c2}$): magnetic field penetrates into a superconductor in the shape of flux lines
3. Normal phase ($H \geq H_{c2}$): superconductor transition into normal state

One of the main parts of *H-T* phase diagram in the mixed phase is the irreversibility line (IL). IL separates *vortex-glass* and *vortex-liquid* areas [70]. *Vortex-glass* state can be visualized as a system of vortices which maintain only a short-range order, as in a glass, with the absence of the movement of the vortices. With the increase of *H* or *T*, the thermal fluctuations of vortices start to amplify, which leads to the loss of the short-range order and motion of the vortices around entire sample. This phase is called *vortex-liquid* [69]. Another important feature of the phase diagram is that the vortex-glass state can be destroyed not only by the increase in temperature, but by reduction of magnetic field as well (see Fig. 2.4). Such behavior appears since reduction of *H* leads to an increase in the

inter-vortex distance, which eventually exceeds London penetration depth and melting of the short-range order of the vortex glass. However, in case of YBCO superconductors, such area is narrow and hard to detect [70].

2.3 Defects in HTS

2.3.1 Classification of defects

*RE*BCO-based superconductors, as well as other HTS materials, contain large densities of growth-related defects. These impurities and defects highly affect the flux pinning properties in the "mixed phase" and are responsible for various pinning regimes and changes in the resulting J_c.

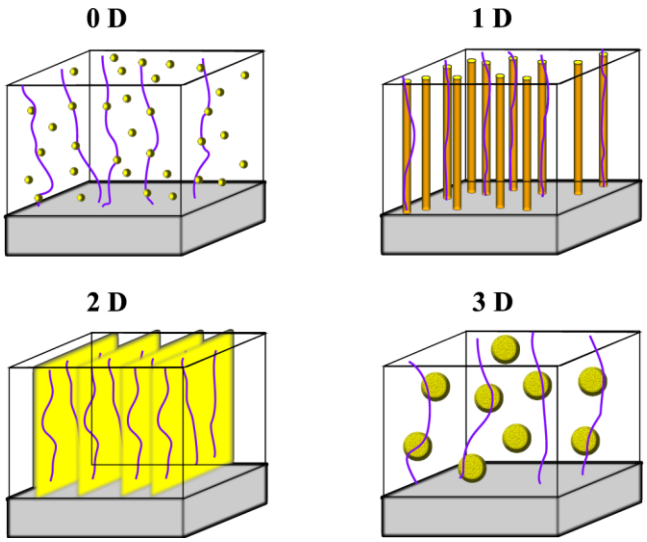

Figure 2.5: Defects of various dimensionalities.

Since the changes in ξ over the impurity is one of the main factors for the flux pinning, in comparison with ξ defects can be divided into 4 groups [73] (see Fig. 2.5):

1. **0 D:** defect size does not exceed ξ in any direction. Impurities, oxygen vacancies, inclusion belong to this group.
2. **1 D:** Defect size exceed ξ in 1 dimension. This group of defects includes dislocations which can appear during thin film growth and can be produced by sub-

strate decoration. Another representative of this group, which shown its effectiveness in improving flux pinning, is columnar defects. Such defects can be produced by heavy ion-radiation or, in case of PLD grown thin films, they are formed during thin film growth.

3. **2 D:** Defect size exceed ξ in 2 dimensions. This group includes twin boundaries, which appear during tetragonal to orthorhombic phase transition due to strain release, interfaces, multilayers, small grain boundaries, anti-phase boundaries as well as stacking faults.
4. **3 D:** This group consist mostly of nanoparticles and secondary phases.

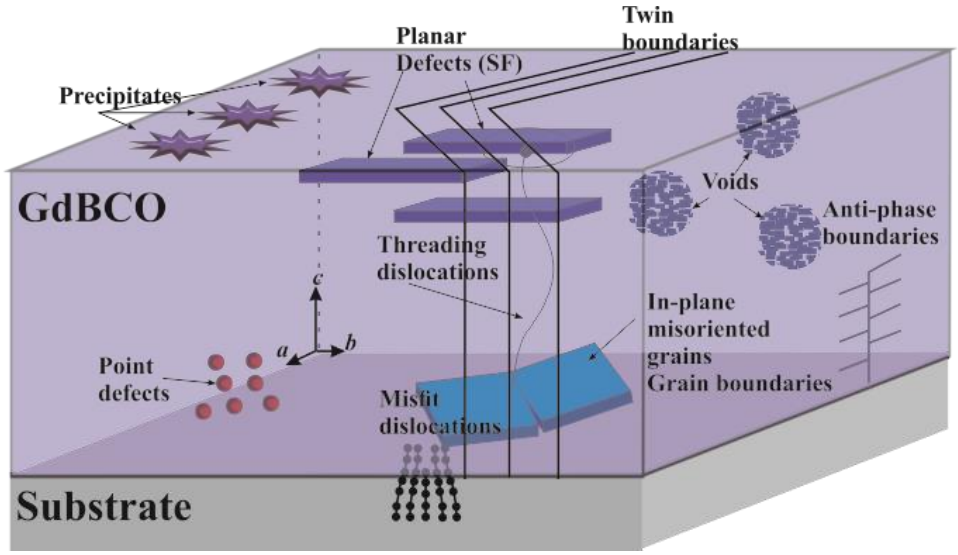

Figure 2.6: Growth related defects in YBCO.

Other classifications which can be assigned to defects are growth-related defects and artificial pinning centers (APCs). Growth related group consist of defects with all possible dimensionalities such as vacancies, dislocation, SF, twin boundaries, grain boundaries, anti-phase boundaries, nanoparticles and the main feature of those is presence of those in pristine *RE*BCO thin films (see Fig. 2.7). APCs group can contain columnar defects, nanoparticles as well as multilayers. Introduction of such defects into *RE*BCO thin films requires additional modifications of the deposition process. For example, in case of PLD grown thin films, the *RE*BCO target should contain certain amounts of secondary phases or multiple targets of different materials are used, which is also the case for creation of multilayer structures.

2.3.2 Role of 1D linear defect in pristine *RE*BCO thin films

Large variety of defects, which are formed during the deposition process and those introduced artificially, strongly affect the results J_c, its behavior at various temperatures, magnetic fields and magnetic field orientations. In recent years, it has been shown that 1D linear defects, such as edge dislocations (ED), play utmost important role and are the main reason for high J_c in pristine *RE*BCO thin films [74-77]. Additionally, a model based on the ensemble of ED gives the closest fit to field dependence of J_c and J_c anisotropy behavior.

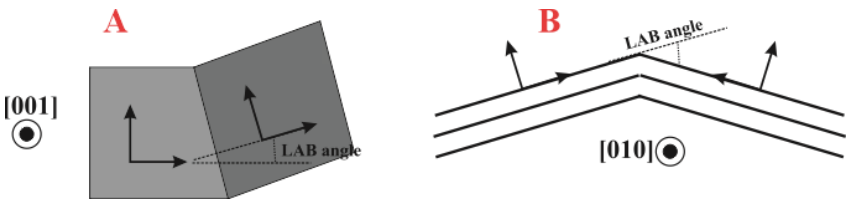

Figure 2.7: Schematic representation of low-angle grain boundaries (LAB) in REBCO thin films. A) [001]-tilt LAB, B) [010]-tilt roof-type.

During the thin film deposition, at the initial stage, when the thickness reaches few unit cells, it has been shown that YBCO film on MgO substrate exhibits spiral-topped islands [78-79]. Compared to other substrates like $SrTiO_3$, YBCO has a larger lattice mismatch with MgO, which is the reason for island type film growth. In addition, these islands may have a small angular misalignment between each other. During further deposition, coalescence of growth islands takes place, which leads to formation of low-angle grain boundaries (LAB) [80]. Most common LAB, which have been observed in *RE*BCO-based films, are [001]-tilt LAB, [010]-valley or roof-top LAB and [100]-twist LAB (see Fig. 2.7).

As shown in [78-79], LAB contain the edge dislocation cores and during the deposition form ED. In pristine *RE*BCO thin films, the density of ED can reach values of 10^{11} lines per cm^2. ED in pristine *RE*BCO-based thin films form domain walls [74, 81] with point-like defects in intradomain space (see Fig. 2.8). These ensembles of ED with point-like defects are responsible for high J_c as well as the appearance of large peak around *c*-axis direction on the $J(\theta)$ dependencies [75-77]. Another important feature, which is also related to the thin film deposition, it is formation of stacking faults (SF) and dislocation loops around them (see Fig. 2.8). Dislocation loops participate both in flux pinning when magnetic field is parallel to the *c*-axis and parallel to *ab*-plane [82]. Moreover, in the

recent years it was shown that the density of ED is dependent on the deposition conditions and may be modified by such parameter as the deposition rate [83].

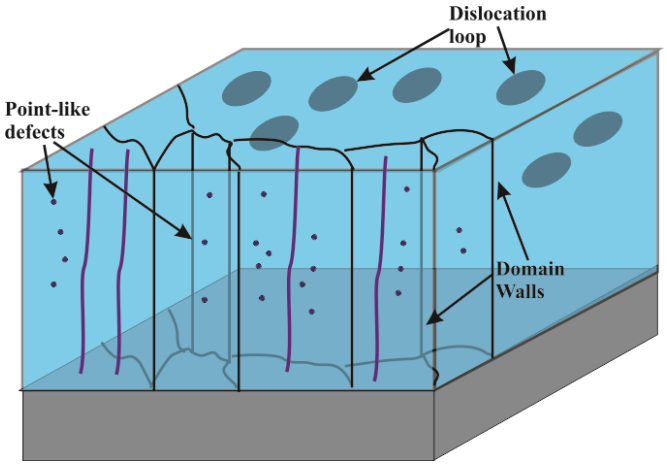

Figure 2.8: Low-angle grain boundaries (LAB) in *RE*BCO-based superconducting thin films.

2.3.3 Pinning regimes

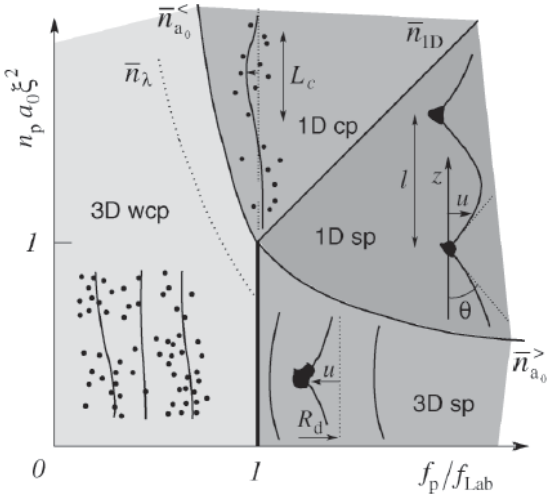

Figure 2.9: Various pinning regimes in HTS. Reprinted Fig. 1 with the permission from G. Blatter, V. B. Geshkenbein and J. A. G. Koopman, Weak to strong pinning crossover, *Physical Rev. Let.* Vol. 92, No. 6, p. 067009, 2004 [84]. Copyright 2022 by American Physical Society.

Pinning centers which are present in *RE*BCO matrix can be characterized by several parameters: n_p – random pins density, u_p – pinning energy, f_p – maximum pinning force, r_p – distance between pins. Depending on these parameters and the vortex density, which depends on the external magnetic field, various pinning regimes can be realized [84]: collective pinning and strong pinning. In accordance with the studies of G. Blatter *et al.* [74], several scenarios can be realized in HTS at fixed magnetic field (see Fig. 2.9):

1. Small f_p: collective pinning regime (3 D wcp).
2. $f_p > f_{Lab}$ ($f_{Lab} = r_p\sqrt{\frac{4\pi B}{\Phi}\varepsilon_0\varepsilon_1}$, Labush criterion): system is in the lattice strong pinning regime (3 D sp).

These 2 scenarios appear if the density of pins n_p is small.

3. Increase in n_p: system goes into single-line strong-pinning regime (1 sp)
4. Further increase in n_p: single-line collective pinning regime (1 D cp).

2.3.4 Requirements for tailoring the pinning morphology

Due to existence of such large variety of defects which can be produced in *RE*BCO matrix, one of the questions which comes alongside is the range of applicability of each type of the defect. *RE*BCO-based superconducting thin films, which are incorporated into coated conductors (CC), have a variety of applications. However, due to different operating regimes the pinning morphology needs to be adapted for that. As of now, 3 major operation regimes are used for CC [85]:

1. **High T, low H:** This operating regime includes applications such as cables, fault current limiters, transformers. For these applications, pristine *RE*BCO superconducting thin films with growth related defects show sufficient performance.
2. **Moderate T, moderate H:** This operation regime includes motors, generators, superconducting magnetic storage devices.
3. **Low T, high H:** This regime mostly includes MRI, NMR, and rotors.

Therefore, depending in what regime *RE*BCO-thin films will be operating, pinning centers have to be adjusted.

Due to the existence of a large variety of compounds, one would assume that the whole periodic table of elements can be used to create artificial pinning centers. However, there are strict requirements for the compounds which can be used as APC [86]. First and foremost is the amount and stability of the compound, since large amounts of secondary

phases might poison the surrounding *RE*BCO matrix and degrade the superconducting and transport properties. Second criteria is the difference in the cell parameters of *RE*BCO superconductor and secondary phase, since small difference in the cell size can allow growth of larger density of misfit dislocation and further increase J_c.

Following these criteria, in the last decades, it was shown that the most effective PC for improving J_c are $BaSnO_3$ [87-90], $BaHfO_3$ [91-96], $BaZrO_3$ [12-15, 97-100] and $BaTiO_3$ with perovskite type crystal structure. Also, $BaYNbO_3$, $BaYTaO_3$ and combination of both [101-103] called double perovskite. Additionally, depending on the growth method for thin films, *RE*BCO-based thin films containing various NPs such as RE_2O_3 and RE_2BaCuO_5 [104-109] have been proved to be effective for J_c improvement. Another important issue, which scientist are trying to solve nowadays, and which affects the applications, is the anisotropy of J_c. One of the goals is to achieve isotropic behavior of J_c. Possible solution of this issue can be a combination of APC with various dimensionalities [110].

3 Experimental thin film deposition and characterization

For engineering applications, one of the most important parameters is the I_c of the superconducting layer. Two main ways exist to increase this parameter: either by increasing the thickness of the superconducting layers or by increasing the critical current density J_c. In this work we mostly focus on the 2nd way: improvement of the J_c. To achieve the highest possible values and to study correlations between J_c and growth conditions it is necessary to make sure that high-quality thin films are obtained in a reproducible manner. Hence, structural and transport characterization is an important step in each study of *RE*BCO-based superconducting thin films.

This chapter presents the main experimental techniques for characterizing the structural and transport properties of pristine and BHO nanocomposite GdBCO superconducting thin films. Section 3.1 is devoted to the pulsed-laser deposition setup for thin film preparation as well as a description of setups used during the last important thin film preparation step, such as oxygen annealing. Section 3.2 is dedicated to the main tools for structural characterization such as x-ray diffractometry, scanning-tunneling microscopy, atomic-force microscopy, and transmission-electron microscopy. In Section 3.3, we will discuss inductive J_c measurement, which is a powerful tool during the optimization process, photolithography and wet chemical etching, which are necessary steps for measurements of the transport properties, as well as different aspects of the transport properties characterization such as T_c measurements, definition of the irreversibility line and anisotropy of J_c.

3.1 Pulsed laser deposition of GdBCO thin films

3.1.1 Characteristic features of the PLD process

Among various physical (molecular-beam epitaxy, pulsed laser deposition, reactive co-evaporation by deposition and reaction process) and chemical (chemical solution deposition, chemical vapor deposition, metal organic chemical vapor deposition) deposition techniques used for thin films preparation, PLD is one, which allows the growth of high-quality oxide thin films. The first mention of PLD for thin film preparation appeared in 1964 in the work of H. M. Smith and A.F. Turner [111] after the invention of pulsed ruby lasers. Since then, PLD was extensively used and developed for research purposes in

different areas of solid-state physics. The PLD process has several features which separate it from other deposition methods and gives advantages for preparation of oxide thin films or chemically complex materials [112]:

1. *Stoichiometric transfer of the material from target to the substrate:* Non-thermal erosion of the target material and initial high heating rates allow films to have similar composition to the target. Additionally, the laser beam source is located outside of the vacuum chamber which in turn gives higher degrees of flexibility.
2. *Thin film deposition from the highly energetic plasma beam:* High kinetic and excitation energies can allow the thin film deposition at lower T_{sub} and, moreover, can assist the formation and chemical reactions appearing on the substrate. In case of PLD, low vacuum chamber pressures help to avoid impurities in the films, while in CVD and MOCVD techniques, the film growth is facilitated by using volatile compounds of the elements of interest and these precursors are introduced into the chamber, where they can react or decompose, and the chemisorbed materials form the film. However, incorporation of decomposed volatile elements into the films still might appear, which in turn will reduce its quality.
3. *Ability of reactive deposition in ambient gases:* Since the PLD does not require electron beam evaporators or filaments for the deposition, different background gases can be used during the deposition process, which has led to the growth of high-quality thin films of multicomponents materials such semiconductors, ferroelectrics, other ceramic materials and, moreover, allows formation of the meta-stable and novel phases.
4. *Formation of multilayered epitaxial heterostructures:* Standard PLD setups allow the placing of several targets into the vacuum chamber with an option of the alternating targets during the deposition process. Hence, thin films with multilayered structure combining different materials can be grown. With the ability to control the deposition near atomic levels, multilayered thin films with the continuous crystal structure can be grown.

Despite the numerous advantages of the PLD for thin films preparation, several drawbacks are present as well:

1. *Large size particulates and growth-related defects:* Due to tremendous number of different parameters during the deposition process, particles with size ranging from few nm up to 100 μm can be present in the films, which is a serious issue during the lithographical processing of the thin films. Additionally, crystallographic defects, due to bombardment of the substrate surface by high energetic ablation particles, combined with impurities, which might be present in the target, can affect the resulting films and worsen its properties.

2. *Film thickness and its uniformity:* In the PLD process, the laser beam is tightly focused on a small spot, which leads to the typical elongated shape of the plasma plume and its forwarded direction. Hence, the thickness uniformity of the films can be affected. R. K. Singh *et al.* [113] showed, that the thin films have the maximum thickness near the area perpendicular to the target irradiated spot and it drops exponentially with increase of the distance from that spot.

On the fundamental level, the PLD process can be divided into 5 stages: 1. Laser beam absorption by the target; 2. One-dimensional expansion of the plume during the laser irradiation; 3. Adiabatic expansion into vacuum or background gas; 4. The plasma plume slows down in the background gas; 5. Ablated atoms/ions recollections on the substrate surface and film growth [114]. Processes 1 and 2 appear during the pulse duration on the ns-timescale and others (3-5) – after the pulse termination.

1. *Laser beam absorption by the target:* The absorption of the laser beam energy by the target material leads to an intense heating of the surface layers. Atoms, ions, and electrons are ejected from the solid. The initial ejection depends on a) the laser parameters: pulse energy density, pulse duration, shape and wavelength; b) temperature dependent optical material parameters such as reflectivity and absorption coefficient; and c) thermophysical properties of the target: heat capacity, density, thermal conductivity [115].
2. *Interaction between ablated material and laser irradiation:* At this stage, within the ns-pulse duration, a further interaction appears between the ablated material and the laser beam. Partially ionized plasma, which is formed on the 1st stage, absorbs the laser irradiation by the means of electron-ion collisions, photoexcitation and inverse bremsstrahlung, hence, increasing the level of ionization. Such processes take place only close to the target. A continuous absorption of the incident radiation forms a plasma with ions of all the components of the target and in ratios not deviating from the original.
3. *Adiabatic expansion into vacuum or background gas:* After termination of the laser pulse, no electrons or ions are evaporated and injected into the inner edge of the plasma. At this point, the thermal energy is rapidly converted into kinetic energy and due to presence of pressure gradients in initial plasma an adiabatic expansion appears. Additionally, a pressure gradient is responsible for the anisotropy of expansion and, hence, for the forward direct nature of the plasma plume.
4. *The plasma plume slows down in the background gas:* Similar to stage 3, the pressure gradients move the plasma plume toward the background gas, and, at the same time, the background gas acts as a confining tool for the plasma on the distances where the initial plasma pressure is significantly reduced and influencing

the angular distribution of ions in the plume. Thus, forming a common elliptical shape of the plume.

5. *Ablated atoms/ions recollection on the substrate surface and film growth:* Finally, atoms of the plasma plume arriving at the substrate surface stick to it and therefore, participate in the film growth. To provide stoichiometric transfer from the target to the films, atoms of all components must be available in a desirable ratio on the film growth points. However, since the kinetic energies of species in the laser ablated plasma are high, additional processes such as atom/ion reflection, sputtering of the film atoms by the ablation atoms and implantation of arriving atoms may take place which can change the stoichiometry of the resulting thin film.

3.1.2 Thin film growth mechanism

When the particles first arrive at the substrate surface, the growth process starts. There are 4 mechanisms of the film growth (see Fig. 3.1): a) layer-by-layer growth or Frank-van der Merve mode, b) island growth or Volmer-Weber mode, c) layer plus island growth or Stranski-Krastanov mode and d) step-flow growth. Each of these growth modes was observed during *RE*BCO thin film deposition.

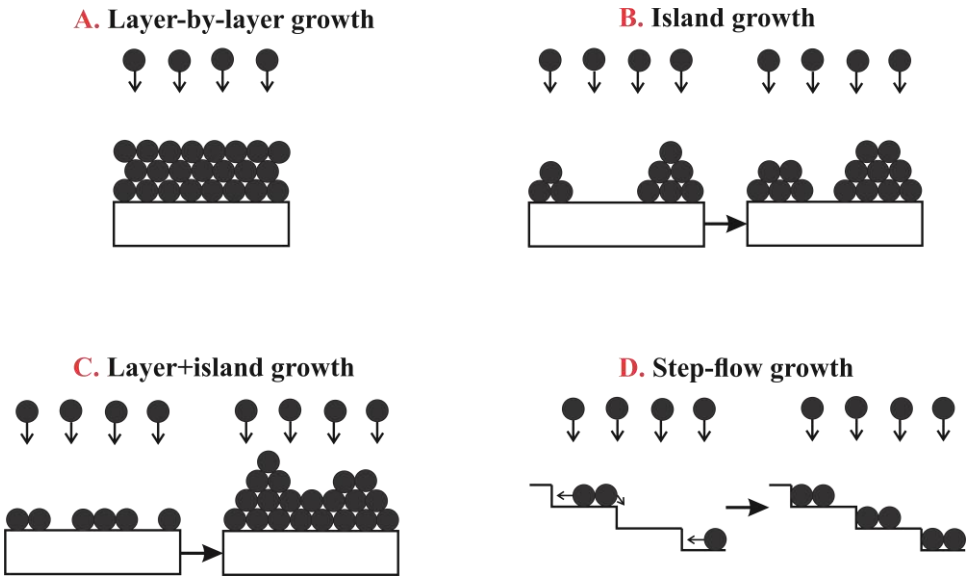

Figure 3.1: Film growth mechanisms: A) Frank-van der Merve growth mode, B) Volmer-Weber growth mode, C) Straski-Krastanov growth mode, D) step-flow growth mode.

In their studies of the PLD-YBCO thin films growth on $SrTiO_3$ substrates, J. Burger *et al.* [116] observed 2D islands growth mode with formation of growth spirals. During deposition of 1 and 2 monolayers of YBCO, the growth is dominated by the lateral growth of 1 YBCO unit cell high nuclei in *ab*-direction. Additionally, clusters with the size 45-70 nm and height up to 6 nm were observed. The density of clusters and nuclei stayed unchanged during transition from 1 monolayer to 2. On the stage of 10 monolayers, the substrate is fully covered by the film and individual terraces with granular structure are observed. These fine granular structures consist of coalescent 2D islands with narrow grooves. The film growths laterally in *ab*-direction by attaching the new material to terrace edges. The density of nucleation sites becomes lower. Additionally, new growth fronts might appear on this stage which are responsible for spiral growth formation due to incoherent merging of these growth fronts. Similar 2D island growth mode was observed for 2 nm thick YBCO thin films deposited on as-polished MgO substrate by K. H. Wu *et al*. [117]. However, 2D behavior changes into 3D islands growth with increasing the film thickness from 2 nm to 50 nm. Moreover, in their studies it was shown that the growth mode for YBCO thin films can be changed by the annealing of MgO substrate or change from MgO to $NdGaO_3$. Step-flow growth mode was observed for YBCO thin films deposited on annealed MgO substrates. In this case islands with larger size, compare to as-polished MgO, nucleate on the edge of the atomic steps formed during annealing. The surface morphology stays unchanged with the increase of the film thickness. On $NdGaO_3$ substrate, the growth process starts as 2D layer with consequent change to 3D island growth mode with the increase of the films thickness. Such changes possibly appear due to dislocations mediated growth. Other factors that might be responsible for the change of the growth mode are the deposition rate and substrate temperature as well as the type of *RE*BCO. Compared to common 2D island growth with spirals formation in YBCO, A. Eulenberg *et al*. [118] noticed after optimizing the deposition conditions for $NdBa_2Cu_3O_7$ thin films that these samples had most likely layer-by-layer growth due to absence of growth spirals and smoother surface. Such growth behavior they attributed to the difference of ionic radii of Y^{3+} and Nd^{3+}, hence, difference in diffusion rates and, additionally, larger target-heater distances used for $NdBa_2Cu_3O_7$ thin films which means a lower kinetic energy of the species in the plume and hence lower surface mobility.

3.1.3 PLD setup

A commonly used PLD setup for oxide thin film deposition (see Fig. 3.2) consists of the following parts: i) laser source, ii) focusing laser beam lense iii) target of the desired material and carousel rotation motors, iii) heater, iv) turbo pump and gas inlet for sustaining the background gas during the deposition process. The real view of the vacuum chamber as well as plume, used during the deposition and substrate glued on the heater are present on Fig. 3.3. In order to fix the substrate on the heater, TED Pella Inc. colloidal

silver was applied to the non-polished side of the substrate, avoiding contamination of the substrate surface and concomitant re-evaporation and diffusion effect into the film. In the commonly used experimental setups for *RE*BCO-based superconducting thin film deposition, excimer lasers are widely used for material ablation. Compared to Nd:YAG laser, excimer laser possess longer pulse durations, larger beam cross-sections as well as the possibility to operate at lower wavelengths.

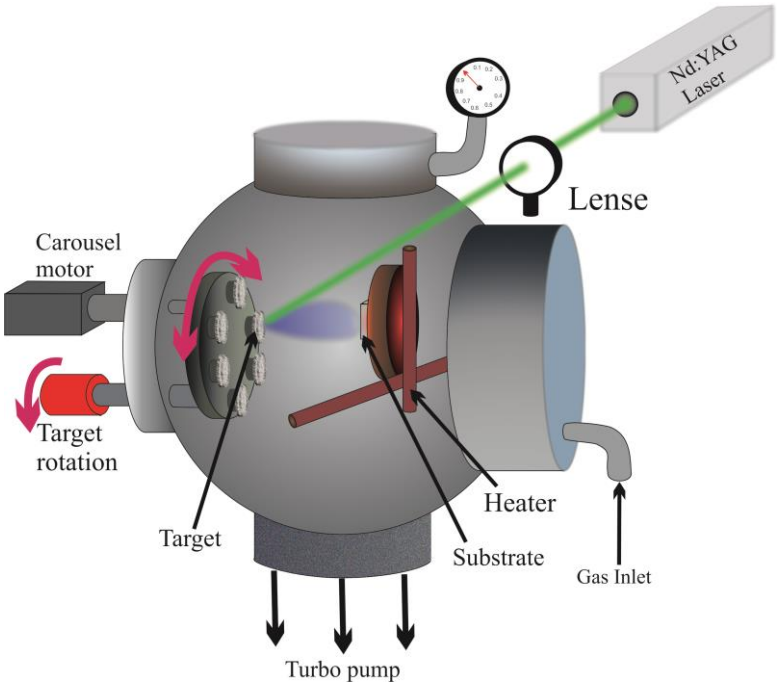

Figure 3.2: PLD setup for deposition of GdBCO superconducting thin films.

However, in the recent years it was shown that high-quality *RE*BCO thin films can also be prepared with 3rd or 4th harmonic Nd:YAG laser [119-122]. The advantages of using a Nd:YAG laser for *RE*BCO thin film preparation are reduction of preparation costs due to lower operation costs of these lasers, safer operation by avoiding usage of gases such as KrF and a better uniformity of the beam with higher energies per pulse. During the deposition process, the propagating beam from 3rd harmonic λ=355 nm Nd:YAG laser is focused by a lens to a round spot of 2 mm diameter on the target, which leads to ablation of the target material. For YBCO thin films, G. Koren *et al*. [123] showed that to achieve lower normal state resistance, higher T_c and smoother surfaces it is necessary to operate at lower wavelength such as 193 and 248 nm. Due to the dependence of the absorption

coefficient on the laser beam wavelength, at lower wavelengths, stronger absorption occurs in the thinner surface layers leading to a hotter plasma plume with finer materials pieces. Due to safety precautions, λ=355 nm was used for the deposition. Another important laser beam parameter is the laser energy density which not only controls the correct stoichiometric distribution of the particles in the plume but is also responsible for the deposition rates. In the studies of PLD-grown YBCO thin films, B. Dam *et al.* [124] showed that the laser energy density needs to exceed 1 Jcm^{-2} otherwise the stoichiometry of the film changes to Y-poor and Cu-rich. For GdBCO thin films, 80 mJ laser energy was used which led to an energy density of 2.5 Jcm^{-2}, far above the threshold. Opposite to the target, the heater with the glued substrate is located in 50 mm distance. For uniform ablation of the material from the whole target, the target is rotated and scanned under the laser irradiation constantly during the deposition. A pump provides the vacuum of 10^{-4} mbar. Additional mass flow controllers connected to the gas inlet are regulating the O_2 background pressure during the deposition process, which allows the deposition between 0.1 and 0.8 mbar O_2. Both target-heater distance and pO_2 are crucial parameters during the deposition process. For each target-heater distance there is a fixed optimum pO_2. Moreover, such adjustment is required since, small distances and large pO_2 can cause damage of the films due to bombardment of the growing film with high energetic ions, while too large distances result in low deposition rates and deterioration of the films due to the lack of the surface activation by moderately energetic ions [125]. Additionally, both parameters regulate the area on the substrate where the films grow. R. K. Singh *et al.* [113] showed that the YBCO film thickness decreases exponentially on a distance of 1 cm from the center and, moreover, the composition is also experiencing the variation away from the center of the substrate.

For pristine GdBCO thin films, a hot-sintered target with density of 99 % was bought from Adelwitz Technologiezentrum GmbH. For BHO nanocomposite GdBCO thin films, hot-sintered GdBCO targets with density of 97 % containing 2.5 wt% of BHO were prepared by Oxolutia SL. Each film was deposited using 6000 pulses, which resulted in a film thickness in the range 220-270 nm. Except the above-mentioned geometrical (target-heater distance, beam spot size), laser (laser energy per pulse, wavelength) and pressure (pO_2) parameters, the main deposition parameters, which affect the resulting thin film properties, are substrate temperature T_{sub} and deposition rate v_{dep}, which can be controlled by the laser frequency in combination with target-heater distance and pO_2. T_{sub} is controlling the diffusion processes, which take place during the film growth, therefore, at low T_{sub} the interdiffusion of species is restrained, while at high values unnecessary substrate-film interactions might appear. Influence of the deposition parameters on structural and transport properties in pristine and BHO nanocomposite GdBCO superconducting thin films will be discussed in detail in Chapter 4, and here we will present a list of the deposition parameters used for thin film preparation (see Table 1).

Table 3.1: Main deposition parameters used for pristine and BHO nanocomposite GdBCO thin films.

Compound	T_{sub}, °C	f, Hz	pO_2, mbar	E, mJ
GdBCO	780-840	10	0.4	80
GdBCO+BHO	780-840	10, 5, 2	0.4	80

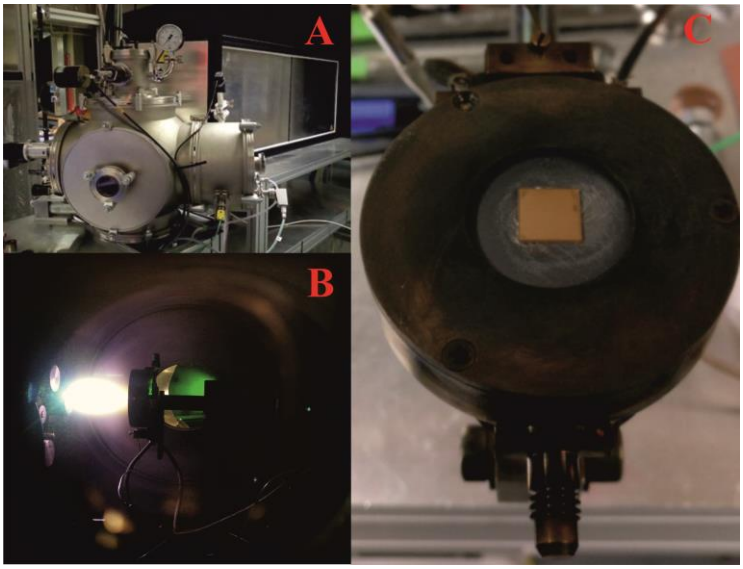

Figure 3.3: A) PLD chamber with the laser housing; B) Plasma plume during thin film deposition; C) Heater with the glued MgO substrate.

3.1.4 *In-situ* and *ex-situ* oxygen annealing

In the subsection 2.3, the influence of oxygen annealing on superconducting and structural properties was discussed. For *RE*BCO-based superconducting thin films, oxygenation is an important step during the deposition process. Therefore, to study how oxygen annealing changes the structural and transport properties in pristine and BHO nanocomposite GdBCO thin films 2 approaches were used.

3.1.4.1 *In-situ* oxygen annealing

To perform a systematic study of the *in-situ* oxygen annealing, the main 3 oxygen annealing parameters such as annealing temperature (T_{ann}), annealing time (t_{ann}) and O_2 pressure during annealing (PO_2) were taken into consideration. All GdBCO thin films were deposited at 800 °C, 10 Hz, 0.3 mbar and 80 mJ (Fig 3.4 – 1, A-B-C transition). After the

deposition, the small oxygen partial pressure was kept during cool down with the rate 10 °Cmin^{-1} to T_{ann} (Fig. 3.4 – C-D) which was in the range between 780 °C and 450 °C. On the next step, the oxygen was introduced into the chamber to create a pressure in the range from 0.1 to 1 bar (Fig 3.4 – D-E). After oxygenation from 5 to 60 min at corresponding T_{ann}, all films were cooled down to RT in the oxygen atmosphere (Fig. 3.4 – E-F).

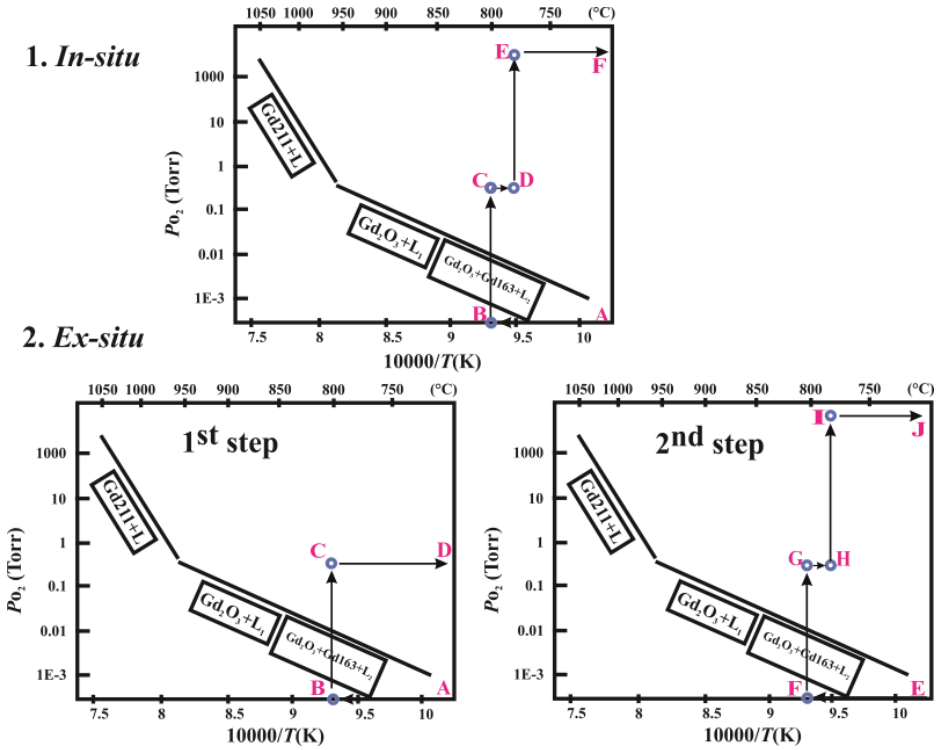

Figure 3.4: Example of *in-situ* and *ex-situ* oxygen annealing with T_{ann}=780 °C and t_{ann}=10 min based on the phase diagram proposed by J. W. Lee *et al*. [29]. Blue circles correspond to different steps of oxygen annealing. 1.Point A-B-C represent heating to 800 °C and thin film deposition at 800 °C and 0.4 mbar. C-D-E-F represents cooling to T_{ann}, oxygen annealing and consecutive cooling to RT. 2. A-B-C-D represents heating to 800 °C, thin films deposition 800 °C and 0.4 mbar and cooling to RT. E-F-G-H-I-J represent heating to 800 °C in Ar, cooling to T_{ann} in mixture of Ar and O_2, oxygen annealing and consecutive cooling to RT.

3.1.4.2 *Ex-situ* oxygen annealing

For *ex-situ* oxygen annealing, compared to *in-situ* case, due to absence of the direct connection between the vacuum chamber and tubular furnace, a 2 step process was

applied. On the first step (see Fig. 3.4), the film is deposited at 800 °C, 10 Hz, 0.4 mbar and 80 mJ (Fig. 3.4-2: A, B and C). Then, the sample is cooled down to RT in the presence of the background oxygen gas (Fig. 3.4 - transition C-D). After removal from the vacuum chamber, on the second step, the sample is placed into tubular furnace, where it is heated to 800 °C in Ar with a rate of 1200 °Cmin^{-1} (Fig 3.4 – E-F). Then, to create similar conditions to cooling in the PLD chamber, a flow of the mixture of Ar and O_2 is applied, followed by cooling to T_{ann}. After reaching T_{ann} of interest, this mixture is exchanged by a 2000ml/min pure oxygen flow where it is oxygenated for t_{ann} and cooled down to RT. To study the influence of the *ex-situ* oxygen annealing, annealing parameters such as T_{ann}, t_{ann} and PLD chamber cooling rate (Q_{PLD}) were taken into consideration.

3.1.5 Pulsed laser deposition on single crystals

For large scale applications, mentioned in Chapter 2, *RE*BCO-based superconductors together with certain buffer layers are usually deposited on commercially available tapes such as Rolling Assisted Biaxially Textured Substrates (RABiTS) or Hastelloy tapes with Ion Beam Assisted Deposition of MgO buffer layer (IBAD-MgO). However, in the current work, to gain a clearer understanding of the subtle changes appearing in the microstructure of PLD-grown GdBCO thin films upon changing the oxygen loading procedure, it was decided to deposit on $LaAlO_3$ (100) and MgO (100) single crystals produced by CrysTec GmbH. The main reason for this is the introduction of various heating and cooling steps during the oxygen annealing. Such heat treatments can possibly cause the formation of new phases at the GdBCO - buffer layer interface if the GdBCO thin film is grown on tape. Additionally, the defects that are present in the GdBCO film on single crystal are usually also present in those on tapes.

3.2 Structural characterization

3.2.1 X-ray diffractometry

One of the rapid techniques for thin films characterization is X-ray diffractometry (XRD). XRD is a non-destructive method which allows to analyze the crystal structure of the material, phase purity and presence of secondary phases, and determine the unit cells size. The main principle of operation of the XRD is based on constructive interference of x-rays. When 2 X-rays are incident on a crystalline material (see Fig. 3.5-A) they are reflected by atomic planes (*hkl*). If the phase difference due to scattering on atomic planes satisfies Bragg's law (Eq. 3.1) interference occurs. By changing the angle of the incident X-ray beam a diffraction spectrum of diffraction intensity can be recorded.

$$n\lambda = 2d_{hkl}\sin\theta \tag{3.1}$$

For GdBCO thin films characterization, a Bruker D8 XRD was used. Such diffractometer has an option of performing measurements in Bragg-Brentano geometry (see Fig. 3.5-B). The sample is placed in the middle of goniometer on the rotating platform, while x-rays from the source irradiate the sample under angle θ and with detection of all scattered radiation in the range 2θ. In case of thin film, the θ-2θ measurements allow to detect (00l) planes parallel to the substrate surface as well as presence of the secondary phases. The X-rays are generated by a copper target with the wavelength 1.54 Å (CuK_α radiation). X-ray patterns are recorded in the 2θ range between 10° and 120° with a step size of 0.02°.

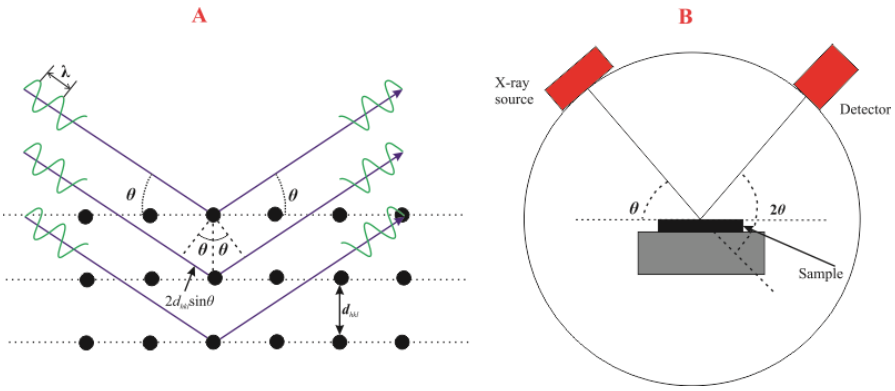

Figure 3.5: A) Bragg's law for constructive interference of x-rays; B) Bragg-Brentano geometry for θ - 2θ scan of XRD

3.2.1.1 *c*-axis lattice parameter calculation

Identification of the *c*-axis lattice parameter is very important for *RE*BCO-based superconducting thin films, as mentioned in Chapter 2, due to its correlation with the oxygen content of the films and, hence, with superconducting properties. Determination of the *c*-axis lattice parameter was based on the approach developed by J. B. Nelson and D. P. Riley [126]. This method requires inclusion of the peaks with both low and high Bragg angles and, therefore, gives an accurate determination of the unit-cell size with the inclusion of all systematic errors which appear during the measurements.

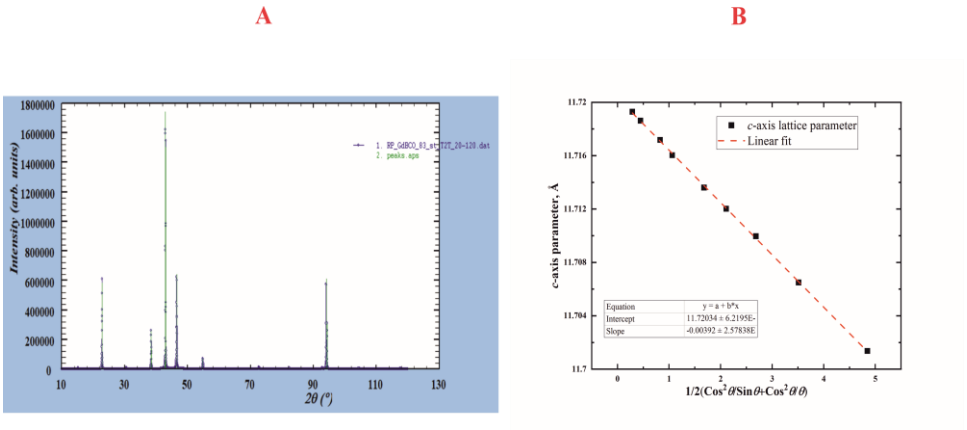

Figure 3.6: A) Peak positions identification using "FullProf Suit"; B) Linear fit for the dependence of the *c*-axis lattice parameter from Nelson-Riley function

The whole calculation procedure consists of following steps:

1. Identification of all GdBCO (00*l*) peak positions using "FullProf Suit" software (Fig. 3.7-A)
2. Calculation of Nelson-Riley function (Eq. 3.2) values for each peak position

$$\frac{1}{2}\left(\frac{\cos^2\theta}{\sin\theta}+\frac{\cos^2\theta}{\theta}\right) \tag{3.2}$$

3. Calculation of *c*-axis parameter for each diffraction peak using Brag's law for interplanar space determination (3.3) and relation between interplanar space with lattice parameters (3.4)

$$d=\frac{\lambda}{2\sin\theta} \tag{3.3}$$

$$\frac{1}{d^2}=\left(\frac{h^2}{a^2}+\frac{k^2}{b^2}+\frac{l^2}{c^2}\right)\rightarrow c=ld\ (h=0,k=0) \tag{3.4}$$

4. Linear fit and determination of the *c*-axis lattice parameter from the extrapolation of the linear fit to 0 (Fig. 3.6)

3.2.1.2 Nanoparticles size estimation

The crystalline size of secondary phases present in the *RE*BCO thin films matrix can be estimated using the Sherrer equation [127] (3.5) with the assumption that all particles have spherical shape and microstrain is negligible.

$$\tau = \frac{K\lambda}{\beta_S \cos\theta} \tag{3.5}$$

Where τ – nanoparticle size, K – dimensionless constant and taken equal to 0.9 with the assumption of spherical shape of the nanoparticles, λ – x-ray wavelength, β_s – the broadening of x-ray peak or FWHM (in radians), and θ – is the Bragg's angle.

3.2.2 Transmission electron microscopy

For applications of *RE*BCO-based superconducting thin films in the development of the new technologies, the superconductor must have the highest J_cs with good in-field performance. Therefore, it is crucial to understand the correlation between microstructure, resulting J_cs and the deposition conditions. Compared to non-destructive XRD, which gives general view of the microstructure, phases, and cell size, TEM has the advantage due to its high resolution and the ability to investigate even the finest details of the material.

In this work, to obtain the TEM images of the film microstructure, one set of the samples were sent to Dr. Hannes Rijckaert in the frame of collaboration between Superconducting thin films group at the Institute from Technical Physics and SCRiPTS group in the University of Ghent, and to Dr. Lukas Grünewald from Laboratory of Electron Micoscopy, Karlsruhe Institute of Technology. A Cs-corrected JEOL JEM 2200FS device, operated at 200 kV, and an uncorrected FEU Titan^3 80-300, operated at 300 kV were used to study the defects in pristine and BHO nanocomposite GdBCO thin films. For the measurements, the films were prepared by cutting a cross-sectional lamella via the Focused Ion Beam (FIB) technique in an FEI Nova 600 Nanolab and an FEI Strata 400S Dual Beam FIB-SEM. The lamella were extracted using the in-situ lift out procedure with an Omniprobe extraction needle. Depending on the angle between the incident beam and the detector, different contrast modes can be used for imaging the samples. TEM images of GdBCO thin films were made in bright field (BF) and low angle annular dark field (LAADF) contrasts due to their sensitivity to defects and strain.

3.2.3 Surface characterization

In combination with XRD and TEM, study of the thin films 'morphology can give additional insight into microstructure of the *RE*BCO-based superconductors and, hence, to understanding of the flux pinning. Therefore, scanning electron microscopy (SEM) and atomic force microscopy (AFM) were used in this work to investigate the surface of the GdBCO thin films.

3.2.3.1 Scanning electron microscopy

SEM is one of the widely used microscopes since it is not only a fast method to check the surface morphology but combined with energy dispersive X-ray microscopy (EDX) can provide information about composition of the sample. Secondary electrons (SE) mode (image is reconstructed by detecting electrons removed from the sample) was used for acquiring surface images.

In this work, during the investigation of the influence of deposition conditions in pristine GdBCO thin films, a Tabletop SEM SH-5000M with imaging by SE and maximum magnification of 100000 was used for fast check of the surface morphology. The operating voltage was in the range 5-15 kV with probe current 110 µA.

3.2.3.2 Atomic force microscopy

Another method for surface morphology investigation is the atomic force microscopy (AFM). AFM allows accurate and non-destructive measurements of different variety of samples (from organic to metals) in air or liquid at nanoscale. AFM consists of 4 main parts (see Fig.3.7) which are used for creation of the surface image in a raster pattern. A cantilever with the AFM probe (tip with the height of few µm) is moving across the features of the sample surface. A laser beam directed on the surface of the cantilever and photodetector are used to track the changes in height. Additional feedback loop is responsible for maintaining the constant interaction force. There are 3 main AFM measuring modes: 1. Contact mode (tip is in constant contact with the surface); 2. Tapping mode (cantilever is oscillating at the resonance frequency and moving in proximity with the surface); 3. Non-contact mode (tip is oscillating at resonance frequencies and moves in few nm distance from the surface).

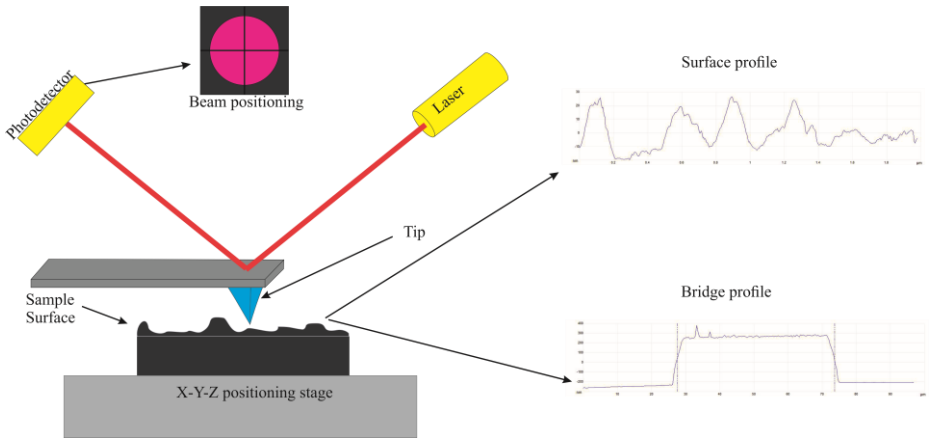

Figure 3.7: AFM working principle

In this work, a Dimension Edge AFM from Bruker was used to study the surface morphology of pristine and nanocomposite GdBCO thin films. All images were made in ScanAsyst peak force tapping mode. 2×2 μm and 20×20 μm areas with 0.1 Hz frequency of the tip movement were used for each GdBCO sample.

Thickness measurements: Bridge width and films thickness measurements of structured samples (see section 3.3) were performed at AFM. Compared to surface measurements, high resolution of the image is not mandatory, therefore, scan area of 100x100 μm with frequency 0.5 Hz were used (see Fig. 3.7). The post-processing and dimensions calculation were done in NanoScope Analysis software.

3.3 Electrical characterization

Due to variety of *RE*BCO-based superconducting thin films applications it is crucial to define not only the field dependence of J_c but also the anisotropy of it. Definition of J_c can be done electrically or inductively. In this work, J_cs of the GdBCO thin films were measured inductively on CryoScan from Theva GmbH and electrical transport properties characterization was performed on Physical Properties Measurement System 14 T (PPMS). PPMS allows a wide range of the transport measurements, in particular, resistance and I-V curves which was a focus of this work. The advantage of the PPMS is that transport measurements can be done in the 4 – 300 K temperature range, 0 to 14 T magnetic field and 5 nA to 0.5 A current range for rotator system and 2 A for puck.

3.3.1 Photolithography

For transport properties characterization due to current limitations of PPMS 14 T, it is necessary to lower current flowing through the sample only to the small bridges. Therefore, it is required to structure the samples using photolithography and wet chemical etching.

On the first stage, all GdBCO samples were cleaned by acetone and 2-isopropanol. Afterwards, the sample was placed into spinning device (see Fig. 3.8 for whole etching process) where 2-4 droplets of AZ 5214 E photoresist from Merck Performance Materials GmbH were applied. To provide uniform coating of the film by a photoresist, the sample is spun with 4000 rotations/min for 30 sec, then another 30 sec with 1000 rotations/min, and 30 sec with 4000 rotations/min again. On the next stage, the film is baked at 100 °C for 2 min before exposure to the UV light. To create 50 μm wide bridges, a special mask was used with irradiation time of 18 sec by UV light. On the final stage, all samples are

kept in the developer for 15 sec. This time was enough to fully develop the bridges due to thickness of the films in the range of 200-270 nm. After developer, all samples were etched in 0.06 % nitric acid for 15 to 30 sec with consequent cleaning in ultrasonic bath with acetone to remove the photoresist. Between exposure to the developer and after etching in acid, the films were kept in distilled water for 5 sec to stop the development and etching process.

***Gold* coating:** After photolithography, the films were fixed on the heater of the PLD chamber (see Fig. 3.3) by using a special mask. After evacuating the chamber to pO_2=0.002 mbar, 15000 pulses at 10 Hz frequency and 100 mJ laser energy were used in order to deposit gold from the gold target.

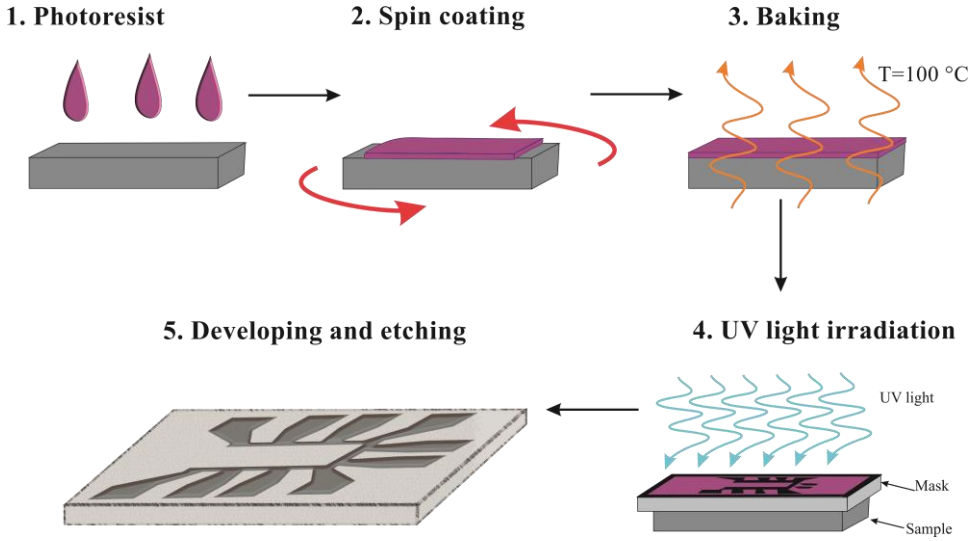

Figure 3.8: Photolithography and wet chemical etching used to structure GdBCO thin films into 50 µm wide bridges.

3.3.2 Inductive J_c measurements

Non-destructive and fast measurements of J_c at 77 K can be done inductively at a commercially available CryoScan from Theva GmbH. This system allows to create a J_c map of samples with different sizes (from 1×1 cm up to 10×1.2 cm). The principle of the CryoScan operation is based on the response of the sample to a small excitation by AC currents. A small coil (see Fig. 3.9), which can be freely positioned on the film surface is inducing an AC current into the sample. AC currents are responsible for appearance of shielding currents which are screening the magnetic field as far as the current is below

the critical value. When the critical current density is exceeded, a signal distortion occurs (see Fig 3.9). These distortions can be detected directly in the coil, and by calibrating the measurements system by resistively measured films and subsequent thickness adjustments the J_c of the film can be determined.

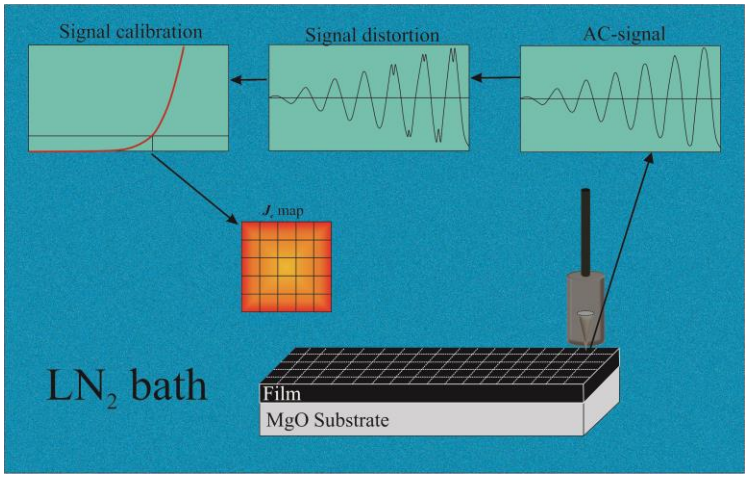

Figure 3.9: Theva GmbH Cryo Scan operation principle

3.3.3 Transition temperatures

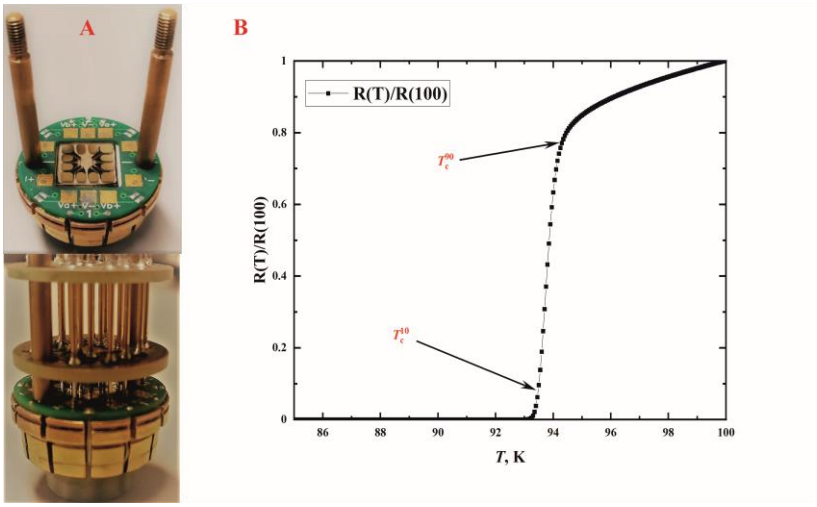

Figure 3.10: A) Puck with the GdBCO thin film, B) Definition of T_c

Both for applications and, especially, for oxygen annealing studies, T_c plays an important role due to its correlation with the oxygen content. T_c of GdBCO thin films were measured on the bridges in PPMS 14 T. Structured samples with the gold contacts are placed on the puck with the press contacts on top (see Fig. 3.10 - A). To define the transition temperatures, the resistance is measured in an 85-100 K temperature range for most of the samples with a temperature step of 0.05 K and a constant current of 100 µA however, some films required cooling down to 70 K. The transition temperature is defined at 10 % of the normal state resistance (see Fig. 3.10 - B).

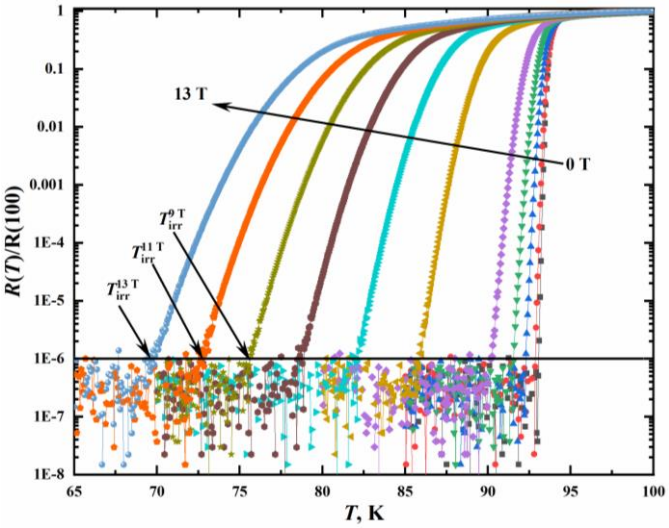

Figure 3.11: Definition of the irreversibility temperatures from R(T) measurements at 0-13 T magnetic fields

3.3.4 Irreversibility line

The irreversibility line, which represents the transition between vortex liquid and vortex glass states, was measured resistively on the PPMS 14 T. Similar to T_c measurements, the temperature dependence of the resistance was measured at 0 to 13 T magnetic fields with step of 2 T and constant current of 100 µA. The temperature range was previously adjusted for each field from 60-100 K at 13 T to 85-100 K at 0 T. The irreversibility temperature was defined as the point where R(T)/R(100) reaches 10^{-6} (see Fig. 3.11). In addition, it is important to point out that the values of irreversibility temperatures, obtained for each sample, may vary depending on the measurements technique [148].

3.3.5 Field and angular dependence of J_c

3.3.5.1 Field dependence of J_c

Similar to T_c and the irreversibility line measurements, the field dependence of the J_c is measured resistively. The voltage drop across the bridge is measured as a function of the transport current. From resulting I-V curves (see Fig. 3.12) the J_c values can be calculated.

Figure 3.12: Example of J_c calculations

In HTS, the voltage is gradually rising near J_c due to different phenomena such as flux creep and inhomogeneous distribution of J_c. Therefore, different methods exist for determination of J_c from I-V characteristics [148], however, in this work only *electrical field criterion* was used. According to this criterion, J_c is defined by the current at which the electric field reaches a certain value. Most used criterion is 1 μVcm^{-1}. To define the field dependence of J_c, I-V curves were measured for magnetic fields in the range 0-9 T for pristine and 0-14 T for BHO nanocomposite GdBCO thin films and the J_c corresponding to a certain magnetic field is calculated. The magnetic field was changed with the step of 0.5 T in the range 5 to 9 T, 0.2 T in the range 0.2 to 4.8 T and 0.02 T between 0 and 0.1 T. Additionally, all samples were placed with the *c*-axis of the film parallel to the magnetic field.

3.3.5.2 J_c anisotropy

Angular dependence of J_c can be measured resistively by installing a rotator (see Fig. 3.13) into PPMS 14 T. Similar to the field dependence measurements, I-V curves were measured in maximum Lorentz force configuration for different angles between magnetic

field and *c*-axis of the sample. In the range of 165°-260° I-V curves were measured with the steps of 5° and between 260° and 280° with steps of 1°. The magnetic field for all samples was set to 1, 3 and 7 T.

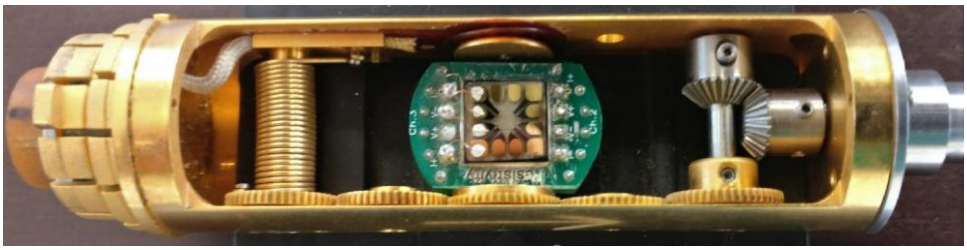

Figure 3.13: Rotator with the sample which was used for anisotropy measurements

4 Dependence of structural and transport properties on deposition parameters in pristine and $BaHfO_3$ nanocomposite $GdBa_2Cu_3O_{7-\delta}$

One of the advantages of *RE*BCO-based superconducting thin films is the high J_c which appears due to the large variety of defects present in *RE*BCO matrix and participating in the pinning of the flux lines. Therefore, to acquire the highest possible J_c, it is necessary to understand the correlation between deposition parameters and defects forming in *RE*BCO, and which defect morphology is the most advantageous for certain applications.

In this chapter we will present the results on influence of deposition conditions such as oxygen partial pressure during the deposition (pO_2), deposition rate (v_{dep}), which is controlled by the laser frequency, and the substrate temperature (T_{sub}) on structural and transport properties in pristine (Section 4.1) and BHO nanocomposite (Section 4.2) GdBCO superconducting thin films.

4.1 Structural and transport properties of pristine $GdBa_2Cu_3O_{7-\delta}$ superconducting thin films

4.1.1 Influence of oxygen partial pressure on superconducting and structural properties

The background gas during thin films deposition plays an important role since it is not only responsible for the coverage area but also for kinetics and the composition of the film. Gd, Ba and Cu cation ablated from the target can oxidize during multiple collisions with the background gas, thus, forming compounds for Gd123 phase. Additionally, the pressure which is created by the background gas combined with the deposition/substrate temperature regulates the phase stability. Regarding all these reasons, pO_2 was chosen as a first deposition parameter to investigate its influence of structural and transport properties.

To exclude influence of all other deposition parameters, GdBCO thin films were deposited at 820 °C, 10 Hz, 80 mJ (2.5 Jcm^{-2}) on $LaAlO_3$ (100) substrates. The oxygen partial

pressure was varied between 0.2 and 0.5 mbar. After the deposition, GdBCO thin films were cooled to 800 °C with 10 °Cmin^{-1} where they are oxygenated for 10 min in 400 mbar oxygen atmosphere with consequent cooling till RT. Similar oxygen annealing route was used for all samples to exclude influence of oxygen annealing on structural and superconducting properties.

4.1.1.1 Superconducting and structural properties

In large variety of studies [128-132], GdBCO films show T_c in the range 92-94 K. Table 4.1 shows that in our case, the highest T_cs are achieved in samples deposited at 0.4 and 0.5 mbar with a small difference of 0.4 K in values (see Table 4.1 and Fig. 4.1-A). Compared to 0.4 and 0.5 mbar samples, lower pO_2 films show drastic decrease of ≥4 K in the transition temperatures. The lowest T_c is achieved at pO_2=0.2 mbar (see Fig. 4.1 and Table 4.1). This sample also has a 2 step behavior in the transition region, which appears due to presence of inhomogeneities in the GdBCO matrix. Such behavior of R(*T*) was also reported by C. De Vero *et al*. [129] for 1μm thick GdBCO thin films deposited at low pO_2.

Table 4.1: Basic superconducting and structural properties of GdBCO thin films deposited at 0.2-0.5 mbar.

pO_2, mbar	0.2	0.25	0.3	0.4	0.5
T_c, K	81.7	87.0	88.2	92.0	92.4
c-axis, Å	11.76	11.76	11.74	11.72	11.71

XRD patterns for GdBCO thin films (see Fig. 4.1-B) show that at higher pO_2 all samples have GdBCO (00*l*) peaks with additional peaks from Gd_2O_3 nanoparticles. However, at low pO_2 one can notice a decrease in the intensity of the GdBCO peaks ((008) nearly disappears at 0.2 mbar). Additionally, all samples have an oxygen content in the optimal range. Thus, since the oxygen annealing process was the same for GdBCO thin films considered in this subsection, structural changes, which appear in the XRD patterns, are caused only by variation of pO_2. Judging from the T_c and XRD behaviour, it is possible that at low pO_2 the reduction of kinetic energies of the species in the plasma plume affects the surface activation (see Chapter 3) which is participating in the formation of the GdBCO film. Additionally, considering that minor changes appeared in *c*-axis lattice parameters, the reason for the reduction of T_c also could be strain effects, which are caused by large defects, secondary phases and inhomogeneous oxygen distribution.

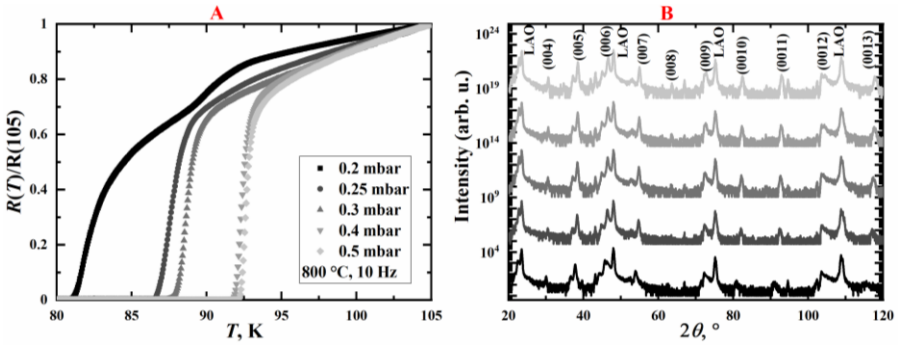

Figure 4.1: A) R(T) dependence, B) XRD patterns for GdBCO thin films deposited at pO_2=0.2-0.5 mbar.

SEM analysis of the GdBCO thin films grown at 0.2-0.5 mbar pO_2 (see Fig. 4.2) shows that all samples have round-shaped droplets on the surface, which are common for *RE*BCO thin films. At 0.2 mbar, the density of the particulates is the lowest compared to pO_2 = 0.3 – 0.5 mbar. As shown in the studies of D. S. Misra and S. B. Palmer [133] on droplet formation in PLD-grown YBCO thin films, ablation of the target by more than 100 pulses leads to an erosion of the target surface and cone formation in the ablated area. These cones favour the extraction of larger particulates, thus, leading to the droplets on the film surface. These droplets have similar stoichiometry to YBCO film [134] and their size and density are affected by the laser energy density.

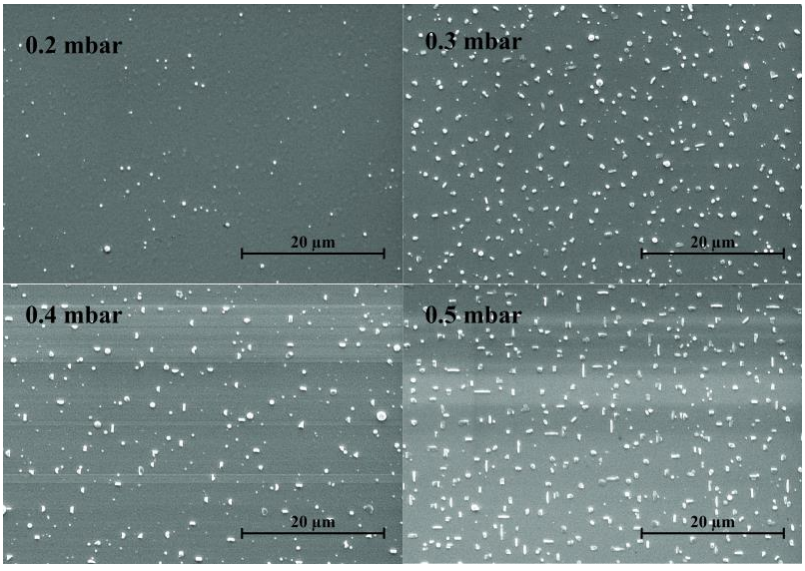

Figure 4.2: SEM images of GdBCO films deposited at pO_2=0.2-0.5 mbar.

The shape of the precipitates becomes stripe-like at 0.4 mbar, and it is clearly seen at 0.5 mbar. Such shape of the precipitates often attributed to the formation of the a-axis grains in the film. Although, the a-axis peaks have not been observed in the XRD pattern, this might be due to low fraction of them in the film and appearance only on the film surface. Other possibility might be that pO_2=0.5 mbar is the border value for our experimental PLD setup after which the fraction of a-axis grains will grow in the GdBCO matrix and will lead to a further deterioration of the structural and superconducting properties. Since, pO_2 is the main parameter, which was changed, variation in size and density we attribute to different thermodynamics caused by it.

4.1.1.2 Self-field J_c dependence on pO_2

Inductive J_c maps (see Fig. 4.3-E) show that with increase of pO_2 self-field J_c at 77 K increases linearly, similar to the situation with T_c, and reaches its maximum at 0.5 mbar.

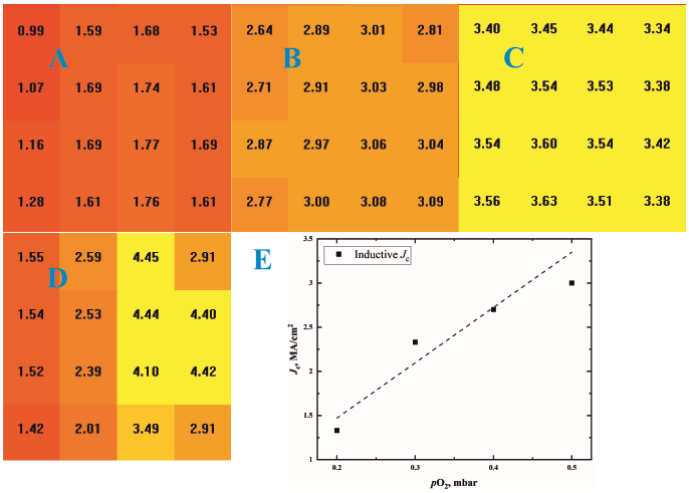

Figure 4.3: J_c maps measured on CryoScan Theva GmbH. A) 0.2 mbar, B) 0.3 mbar, C) 0.4 mbar, D) 0.5 mbar, E) Self-field J_c and pO_2 correlation. J_c values are recalculated with the actual thickness of 250nm.

The values on the Fig. 4.3 A-D differ from the values on E due to 200 nm assumption of the film thickness for the measurement. However, the overall trend of J_c enhancement with increase of pO_2 may be seen in Fig 4.3, which may appear due to changes in the density of ED and size of domain walls formed by ED. As shown in previous studies [83], the density of ED can be modified by changing the deposition rate, which in this case is affected by the change of pO_2. Fig. 4.3 A-D shows that regardless having the highest self-field J_c at 0.5 mbar, the increase in J_c is not significant, however, the uni-

formity of J_c drops with increase of pO_2. For applications of *RE*BCO-based superconductors a more uniform distribution of J_c over the length is preferable. Therefore, for consequent studies on influence of v_{dep} and T_{sub}, pO_2=0.4 mbar was chosen as optimum.

4.1.2 Influence of deposition rate on superconducting and transport properties

Compared to the background gas and its pressure pO_2, which regulates the coverage area, the kinetic energy of the species in the plasma plume and the composition of the film, the deposition rate (here controlled by the laser frequency *f*) is the only kinetic parameter and combined with T_{sub} regulates the crystalline quality of thin films. v_{dep} controls the diffusion time of the species on the substrate surface. Since we have chosen pO_2 =0.4 mbar as the optimum, to study the influence of the deposition rate on the structural and superconducting properties 820 °C, 0.4 mbar and 80 mJ were used. The laser frequencies used are 10 and 5 Hz. After the deposition, each sample is cooled to 800 °C with 10 °Cmin^{-1} where samples are oxygenated for 10 min at 400 mbar oxygen atmosphere with consequent cooling to RT. Similar to subsection 4.1.1, the same oxygenation process is adapted to exclude influence of other parameters.

The summary of basic superconducting and structural properties (see Table 4.2 and Fig.4.4-A) shows that with decrease of the deposition rate in our experimental setup, T_c drops from 92 K at 10 Hz to 90.5 K at 5 Hz. Transition width is increasing with the decrease of the v_{dep}. Inductive J_c measurements shows that *f*=10 Hz exhibits higher self-field J_c. Due to such reduction, the lower deposition rates have not been considered. Similar to the situation of various pO_2, the variation in frequency affects v_{dep}, thus, resulting in a higher density of ED at 10 Hz.

Table 4.2: Basic superconducting and structural properties of GdBCO thin films deposited at 10 and 5 Hz.

v_{dep}, Hz	5	10
T_c, K	90.5	92.0
c-axis, Å	11.70	11.72
J_c (0 T, 77 K), MAcm^{-2}	2.2	2.5

XRD pattern for GdBCO films deposited at 10 and 5 Hz (see Fig. 4.4-B) shows that the decrease in the deposition rate does not bring drastic changes as it is seen for various pO_2. All samples have GdBCO (00*l*) peaks which indicates of highly *c*-axis oriented thin films. The calculated *c*-axis show that at 10 Hz samples has optimum oxygen doping, while for 5 Hz it corresponds to overdoped region. J. P. Suh *et al*. [135] in the studies on

the influence of deposition rate on crystalline structure of YBCO thin films showed that combination of v_{dep} with T_{sub} can drastically change the structure of the films:

A) **low T_{sub} and high v_{dep}**: formation of tetragonal YBCO structure with short-range orthorhombic domains. Such structure is related to kinetics of adatoms because the diffusion rate is reduced at low T_{sub}, and high v_{dep} lowers the migration time. Therefore, species does not have enough time to move to energetically favorable places.

B) **high T_{sub} and v_{dep}:** formation of cation disordered *c*-axis oriented orthorhombic structure.

C) **high T_{sub} and low v_{dep}:** formation of *c*-axis oriented orthorhombic structure.

Combination of T_{sub}=820 °C and f=10 Hz in our case possibly corresponds to the case B, while T_{sub}=820 °C and f=5 Hz to case C. However, both films show *c*-axis oriented orthorhombic structure. The higher T_c value at 10 Hz is related to the oxygen content in the film (see Table 4.2). As shown in the work of A. H. El-Astal *et al*. [136] on the role of gas-phase oxidation during growth of YBCO thin films, the Cu oxidation in the plume mostly appears close to the substrate surface, which in turn combined with higher migration time of the species at 5 Hz and diffusion rates at 820 °C possibly leads to the changes in the film microstructure, therefore, higher oxygen content in the film but reduced T_c and lower J_c as seen in Table 4.2.

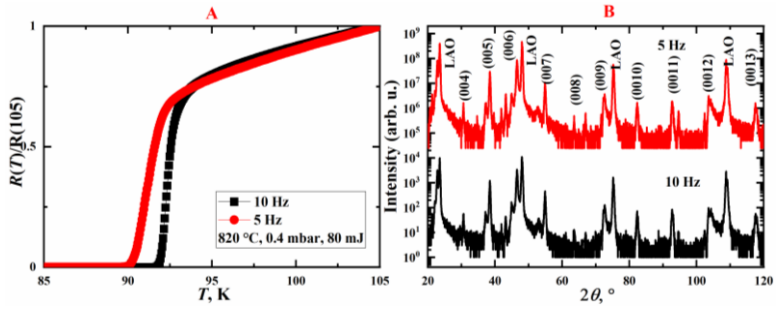

Figure 4.4: A) *R*(T) dependence, B) XRD paptterns for GdBCO thin films deposited at 10 and 5 Hz.

SEM images for PLD-grown GdBCO films with 10 and 5 Hz (see Fig. 4.5) shows that with the decrease of the laser frequency, the density of particulates is increasing.

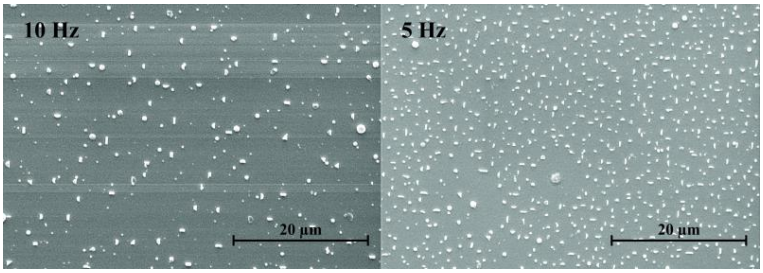

Figure 4.5: SEM images of GdBCO films deposited at 10 and 5 Hz.

4.1.3 Influence of substrate temperature on structural and superconducting properties

4.1.3.1 Superconducting and structural properties

The substrate temperature (T_{sub}) regulates the diffusion rate of the species from the plasma plume on the substrate surface and therefore affects the nucleation and growth process of the film. In the previous subsections it was shown that the sample grown at pO_2=0.4 mbar and v_{dep}=10 Hz exhibits only slight reduction in T_c compared to pO_2=0.5 but more uniform distribution of J_c on inductive J_c map. Therefore, to study the influence of T_{sub} on structural and transport properties, GdBCO thin films were deposited at 10 Hz, 0.4 mbar, and T_{sub} was varied between 780 °C and 840 °C. After the deposition, all samples were cooled down for 20 °C with 10 °Cmin^{-1} where they were oxygenated for 10 min at 400 mbar oxygen atmosphere. After oxygen annealing, all GdBCO thin films were cooled to RT with 10 °Cmin^{-1}.

Table 4.3: Basic superconducting and structural properties of GdBCO thin films deposited at 780 °C-840 °C.

T_{sub}, °C	780	800	820	840
T_c, K	91.6	92.0	92.0	91.7
c-axis, Å	11.71	11.72	11.72	11.73

GdBCO thin films deposited at T_{sub}=780 °C-840 °C (see Table 4.3) show that the transition temperatures do not vary more than 1 K. The highest values of 92 K are achieved at 800 °C and 820 °C. XRD patterns of these samples (see Fig. 4.6-B) show that all samples have strong GdBCO (00*l*) peaks, which indicates highly *c*-axis oriented films. Additional peaks from Gd_2O_3 (200), (422) and (345) orientations are present as well. B. L. Low *et al*. [137] showed in their studies on the dependence of the texture quality from T_{sub} that at low T_{sub} the energy is insufficient for surface mobility and, therefore, the majority of unit cells are unable to align their *c*-axis with the normal of the substrate. With increase of T_{sub}

surface mobility is improving and unit cells are able to align their *c*-axis with the normal of the substrate. Compared to the range of temperatures used in their studies, in our case a smaller range of T_{sub} was used, thus, no drastic changes in crystalline structure and superconducting properties were noticed. The estimated *c*-axis lattice parameters show that independent of the T_{sub}, all samples have optimum or close to optimum oxygen content.

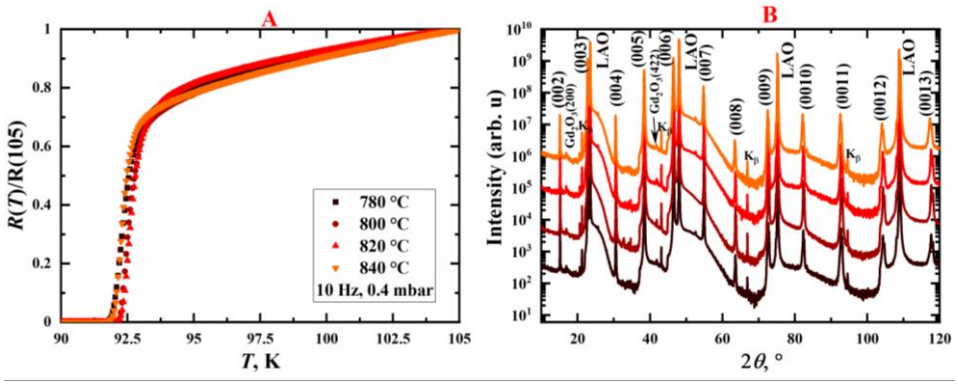

Figure 4.6: A) *R*(T) dependence,
B) XRD patterns for GdBCO thin films deposited at T_{sub} = 780 °C-840 °C.

SEM images of GdBCO thin films (see Fig. 4.7) show that at 840 °C sample has droplets with size varying between 1 and 3 µm. At 820 °C, the density is somewhat lower compared to 840 °C but the size is larger.

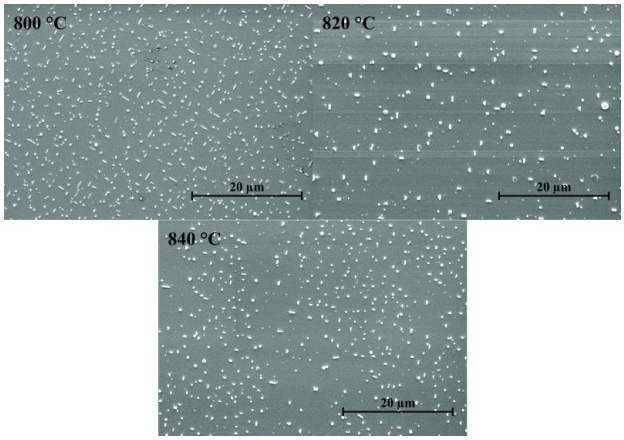

Figure 4.7: SEM images of GdBCO films deposited at T_{sub}=780 °C-840 °C.

At 800 °C sample has the largest density of precipitates many of which have stripe-like shape which is not seen for T_{sub}=840 °C. Such variation in the size and density of particulates between 800 °C and 840 °C is attributed to higher diffusion rate and better alignment of the grains at high T_{sub} since according to [127], the reduction of T_{sub} causes particulates arriving on the surface of the growing film have lesser surface mobility and the diffusion length, thus, leading to worsening of alignment of *c*- and *ab*-orientations.

Inductive J_c measurements (see Fig. 4.8) show that the highest self-field J_c of 3.6 MAcm^{-2} is achieved for the sample deposited at 800 °C. A slightly lower value has sample with T_{sub}=780 °C, and the lowest are at 820 °C and 840 °C. Increase or decrease of T_{sub} modifies the diffusion processes during the film growth. Therefore, changes in J_c can possibly be attributed to the change in the size of domains formed by the ensemble of ED in the GdBCO film.

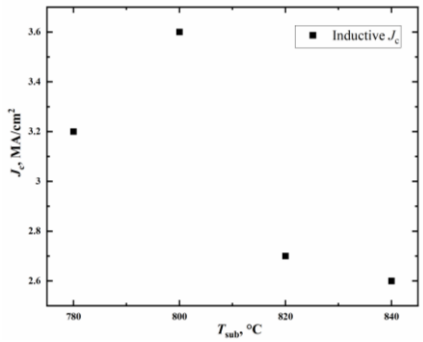

Figure 4.8: Inductive J_c measurements for GdBCO thin films deposited at T_{sub}=780 °C-840 °C.

4.1.4 Microstructure and transport properties of the film prepared at optimum conditions

Since the sample deposited at T_{sub}=800 °C, f=10 Hz and pO_2=0.4 mbar shows the highest T_c and self-field J_c values with good crystallinity and *c*-axis orientation of the film, it is chosen for further investigation of microstructure and transport properties. GdBCO thin film deposited at optimum conditions shows an irreversibility field (B_{irr}) at 77 K of ≈8 T, which lies within the range of irreversibility fields previously reported for pristine GdBCO thin films [92, 95, 128] and exceeds those reported for YBCO [98, 101, 102, 104, 109] mainly due to higher T_c.

J_c (see Fig. 4.9-B) reaches 3.2 MAcm^{-2} at 77 K and 0 T which is quite common for *RE*BCO-based superconducting thin films and lies within the range 2-6 MAcm^{-2} as

reported [90-110, 128-132] for GdBCO and YBCO thin films. Pinning force densities (F_p, see Fig. 4.9-C) at 77 K has the highest values of 4.6 GNm^{-3} which is reached at 1.2 T magnetic field.

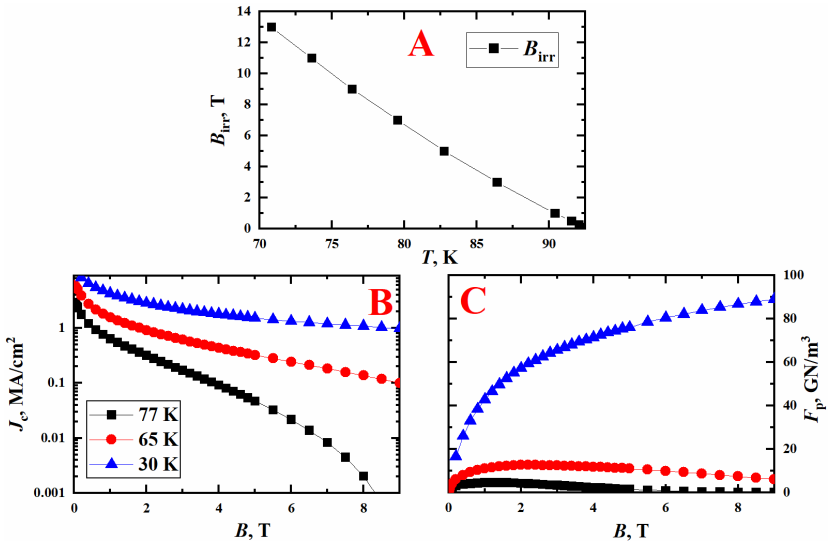

Figure 4.9: Transport properties of GdBCO thin films deposited at 800 °C, 10 Hz, 0.4 mbar. A) Irreversibility line; B) Field dependence of J_c at 77, 65 and 30 K; C) Field dependence of F_p at 77, 65, 30 K.

Angular dependence of J_c (see Fig. 4.10-B, C) shows that at 1 T, 77 and 65 K sample has a large peak in the *c*-direction with additional shoulder in the area 95°-135°. At 3 T, 77 and 65 K peak is present as well with somewhat larger shoulder. As mentioned in subsection 2.3.2, in pristine *RE*BCO thin films 1D linear defects such as edge dislocations play an utmost important role for flux pinning. Due to the island-type growth of the thin film and misalignment between the islands, LAB are formed during coalescence. LAB contain cores of ED, which during further deposition forms ED in the *RE*BCO matrix. Ensemble of ED form domain walls and are able to pin vortices along their whole length [74, 75, 81]. Therefore, as shown by BF-STEM images (see Fig. 4.10-A), optimally grown GdBCO thin film has domain walls with dislocation threading through the whole films. Thus, a large peak in *c*-direction appears due to flux pinning at linear defects. The peak is most prominent at 1 T, possibly because 1 T provides the density of flux lines matching the density of ED in GdBCO film. The appearance of a similar peak at 1 T, 77 K was previously reported for PLD-grown GdBCO thin films on MgO single crystals [128]. Additionally, the appearance of the shoulders may be due to combined flux pinning at SF

and Gd_2O_3 NPs, which are also seen in Fig. 4.10-A, and such an effect was previously reported for YBCO films containing Y_2BaCuO_5 NPs [109].

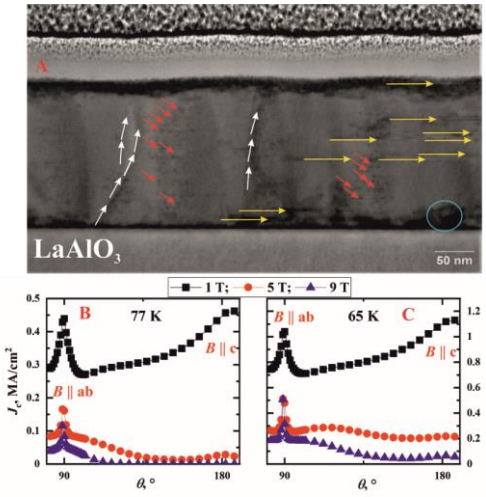

Figure 4.10: J_c (θ) dependence at A) 77 K and B) 65 K and 1, 5, 9 T magnetic fields. C) BF-STEM images of GdBCO film deposited at 800 °C, 10 Hz, 0.4 mbar. White arrows indicate threading dislocation, yellow-SFs, red-Gd_2O_3 nanoparticles.

4.2 Structural and transport properties of $BaHfO_3$ nanocomposite $GdBa_2Cu_3O_{7-\delta}$ superconducting thin films

In a variety of studies related to the introduction of different types of secondary phases such as RE_2O_3 nanoparticles, Y_2BaCuO_5, $BaHfO_3$, $BaZrO_3$, $BaSnO_3$, Ba_2YTaO_5 and Ba_2YNbO_5 [89-110], it was shown that the secondary phases can drastically increase the in-field performance of *RE*BCO-based superconducting thin films with amount of secondary phase up to 10 wt. %. In most of the works related to PLD-growth of *RE*BCO-based thin films, different types of excimer lasers are used. Due to the usage of Nd:YAG laser and pioneer works in our lab on growth of BHO-nanocomposite GdBCO thin films our studies were limited to GdBCO with 2.5 wt% BHO.

Compared to pristine *RE*BCO thin films, one of the most prominent aspects of PLD-grown *RE*BCO thin films containing BMO precipitates is the effect of self-organization. J. J. Shi and J. Wu [138] have shown that these BMO secondary phases can grow in the

shape of nanocolumns due to strain effects, which appear as a result of lattice mismatch between *RE*BCO and Ba*MO*$_3$ (BMO, *M*=Hf, Zr, Sn, Ce). This effect was confirmed experimentally on the example of YBCO thin films containing BZO secondary phases [13-15]. Another interesting feature, which was studied both theoretically [139] and experimentally [15], is the influence of T_{sub} and v_{dep} on the shape and size of these nanocolumns. According to these studies, the behavior of BMO secondary phases regarding T_{sub} and v_{dep} can be divided into 3 groups:

1. Low T_{sub}+high v_{dep}: secondary phases mostly grow as NPs or segmented nanorods
2. Low T_{sub}+low v_{dep} high T_{sub}+high v_{dep}: these combinations of deposition parameters give a mixture of nanocolumns, segmented nanocolumns and NPs
3. High T_{sub}+low v_{dep}: these conditions result in the formation of well aligned along *c*-axis of the film nanocolumns. However, quite often the diameter of nanocolumns becomes too large and starts to disrupt the *RE*BCO matrix.

Therefore, setting as reference point optimum deposition conditions for pristine GdBCO thin films, here, we studied the influence of T_{sub} and v_{dep} on structural and transport properties in 2.5wt.% BHO nanocomposite GdBCO thin films in order to find the optimum deposition parameters for the studies of Chapter 7.

4.2.1 Influence of T_{sub} on structural and transport properties

4.2.1.1 Superconducting and structural properties of BHO nanocomposite GdBCO thin films

To understand the influence of the growth temperature on the BHO formation and resulting in-field performance, GdBCO thin films were deposited on $LaAlO_3$ (100) single crystals at 10 Hz, 0.4 mbar. Similar to pristine samples, T_{sub} was varied in the range 780 °C-840 °C. After the deposition, all samples were cooled down by 20 °C with 10 °Cmin^{-1}. At this point, all samples were annealed in 400 mbar oxygen atmosphere for 10 min with consequent cooling to RT with the rate 10 °Cmin^{-1}.

Table 4.4: Basic superconducting and structural properties of BHO-nanocomposite GdBCO thin films deposited at 780 °C-840 °C.

T_{sub}, °C	780	800	820	840
T_c, K	90.1	91.5	91.9	91.4
c-axis, Å	11.74	11.75	11.75	11.75

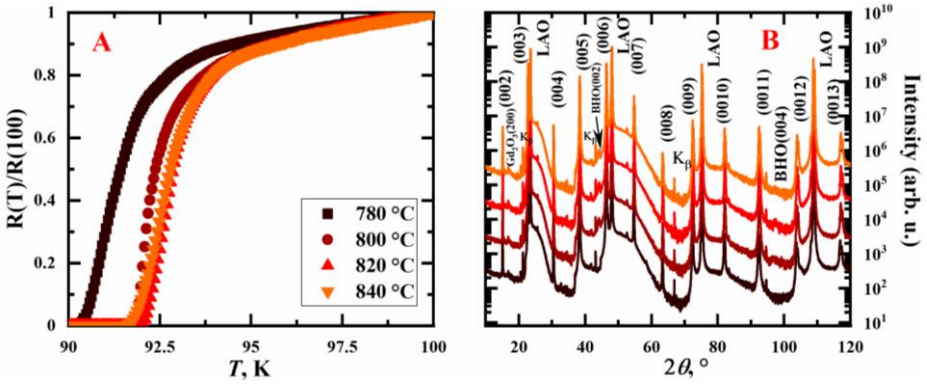

Figure 4.11: A) R(T) dependence and B) XRD patterns for BHO-nanocomposite GdBCO thin films deposited at 780 °C-840 °C.

Systematical R(*T*) measurements (see Table 4.4 and Fig. 4.11-A) show that compared to pristine GdBCO thin film deposited at optimum conditions, T_c of BHO-nanocomposite samples is reduced. This is a common effect of introduction of secondary phases into *RE*BCO-matrix by PLD. Due to strain effects during the film growth [93, 140], BHO nanocolumns create surrounding oxygen deficient regions which in turn reduces the transition temperature of the films. XRD patterns (see Fig. 4.11-B) show GdBCO (00*l*) peaks, which indicates highly *c*-axis-oriented films. Additionally, starting from 800 °C, BHO (004) peak with $2\theta \approx 44$ ° appears on the XRD patterns. Another peak with orientation (008) is visible only for $T_{sub} \geq 820$ °C. The *c*-axis lattice parameters (see Table 4.4) of BHO nanocomposite GdBCO thin films have larger length of the *c*-axis than the pristine films, which appears as a result of strained in the *c*-axis direction films ($3a_{BHO} > c_{GdBCO}$).

BF-STEM images of GdBCO films deposited at 800 °C and 820 °C (see Fig. 4.12) show that at 800 °C the GdBCO thin film has segmented BHO nanocolumns distributed in its matrix. The diameter of these nanocolumns varies between 4 and 5 nm. Between the nanocolumns, some agglomeration of short BHO particles as well as strain regions at the interface of substrate and film are present. Such strained regions possibly appear due to the lattice mismatch between GdBCO and the LAO single crystal. Compared to 800 °C, at 820 °C BHO shows a more elongated shape of the nanocolumns with less BHO agglomerations. According to previous studies on BHO formation in *RE*BCO-based superconducting thin films [15, 139], the nanocolumns' diameter should be increasing with the increase of T_{sub}, however, at 820 °C the size of nanocolumns varies in the range 4-5 nm similar to situation at 800 °C. This apparent contradictory with previous reports can be explained by the difference in the deposition temperature steps which were used in those work. In our case, 20 °C difference does not affect drastically the size distribution.

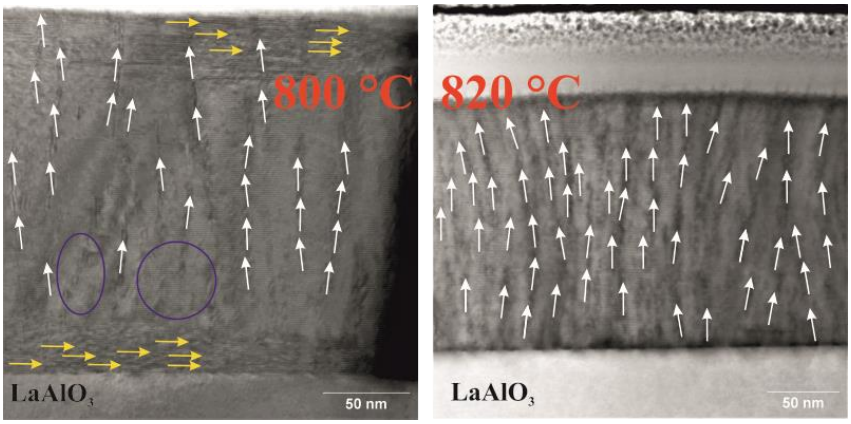

Figure 4.12: BF-STEM images for BHO-nanocomposite GdBCO thin films deposited at 800 °C and 820 °C. White arrows indicate at BHO nanocolumns, yellow arrows – strain regions and SFs, blue circles – agglomeration of BHO nanocomposites in GdBCO.

4.2.1.2 Transport properties

IL for samples deposited at 780 °C-840 °C (see Fig. 4.13) shows that the films deposited at T_{sub}=800 °C and 820 °C have an S-shape. Such S-shape is a common sign of the nanocolumn formation in GdBCO matrix. A similar behavior was previously reported for *RE*BCO-based superconducting thin films containing $BaMO_3$ (BMO, M=Hf, Zr, Sn) nanorods [89, 101]. Since the BHO-nanocomposite GdBCO films were grown on LAO single crystals, this situation corresponds to the growth of GdBCO films on lattice matched substrate [138]. In accordance with the micromechanical model for self-organized secondary phases, the biggest influence on the growth of BHO in GdBCO matrix has the lattice mismatch between BHO and GdBCO. In this case, the alignment of nanorods along *c*-axis of the substrate appears as result of a smaller GdBCO lattice deformation and, thus, being the energetically favorable state. Matching field (B_Φ) estimated from average distance between the nanorods has a value of 6.9 T for T_{sub}=800 °C and 6.7 T for T_{sub}=820 °C.

Compared to T_{sub}=800 °C and 820 °C, at the highest T_{sub}=840 °C, the S-shape of IL is beginning to vanish. Increase of T_{sub} enlarges the size of the nanocolumns. The bigger size means a smaller density of the nanocolumns and larger oxygen deficient zones. Thus, resulting in slightly worse superconducting properties and reduced matching fields.

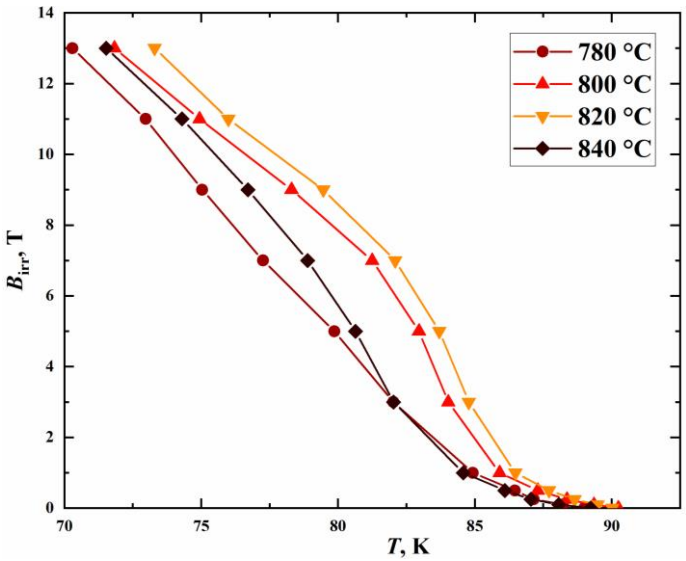

Figure 4.13: ILs for 2.5wt% BHO nanocomposite GdBCO thin films deposited at T_{sub}=780 °C-840 °C

In case of T_{sub}=780 °C, the behaviour of IL is similar to pristine GdBCO films (see Fig. 4.9). At low T_{sub} and high v_{dep} the diffusion rate and diffusion time are low, therefore species arriving in the substrate surface can not move to the energetically favorable position before the next wave of species arrives. Therefore, in this case the GdBCO matrix has mostly random disorder and correlated pinning centers in the shape of segmented BHO nanorods.

The field dependence of J_c (see Fig. 4.14), which is one of the important characteristics for engineering applications and to gain insight on the T_{sub} influence on transport properties and for a possibility of tailoring the desired pinning landscape in the future. At 77 K (Fig. 4.14) GdBCO films deposited at 800 °C and 820 °C have the highest in-field values in the whole range of magnetic fields. Compared to high T_{sub}, 780 °C shows the strongest decay with increase of magnetic field, however, it has the highest self-field J_c=1.7 MAcm^{-2}.

J_c behavior can be described with empirical function:

$$J_c = J_c(0)\left(1+\frac{B}{B_0}\right)^{-\alpha}(1-\frac{B}{B_{irr}})^q \tag{4.1}$$

where B_0 is the length of the low field plateau related to the self-field, B_{irr} – irreversibility field, α and q are fitting parameters. Here, q = 1 is set, since it gives better fitting for $J_c(B)$ behavior. α for pristine sample has a value of 0.73 (see the inset on Fig. 4.14),

which is close to previously reported for pristine GdBCO thin films [91, 128]. BHO nanocomposite samples, compared to pristine, have lower values with smallest fitting parameter achieved at T_{sub}=800 °C and 820 °C. However, these values are still higher than those reported for *RE*BCO-based superconducting thin films with BMO secondary phases [141, 142]. The difference with previous studies possibly appears due to the combination of correlated pinning centers and random disorder, which results from relatively low T_{sub} and high v_{dep}.

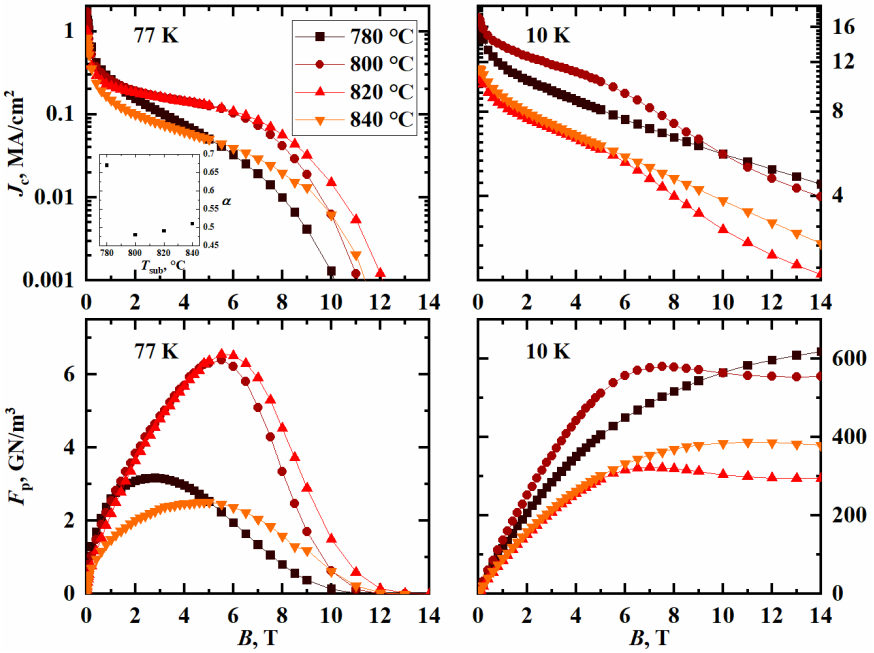

Figure 4.14: $J_c(B)$ dependence for 2.5 wt.% GdBCO superconducting thin films deposited at 780 °C-840 °C. The inset show dependence of the fitting parameter α on T_{sub}.

The $J_c(B)$ behavior changes at 10 K. The highest in-field values has the film deposited at T_{sub}=800 °C in the range 0-9 T. In the high field region between 9-14 T, T_{sub}=780 °C show better performance compared to T_{sub}=800 °C. Contrary to the situation at 77 K, GdBCO thin films deposited at 820 °C and 840 °C show the strongest dependence on magnetic field. Such a behavior is due to change of coherence length ξ with the decrease of the measurement temperature. With a temperature decrease the coherence length is reducing, thus, the vortex core size is also reducing [70]. Therefore, as it was shown in studies of vortex pinning in HTS [70] and the role of weak pinning at low temperatures [143], in low temperature region due to smaller vortex core, weak pinning centers give

higher contribution to the flux pinning compared to strong correlated pinning center, while at LN_2 temperatures strong correlated pinning centers such as BHO nanocolumns able to pin vortices along their whole length, which also gives a characteristic plateau on $J_c(B)$ dependence. The samples deposited at 780 °C and 800 °C have a combination of strong correlated pinning centers (segmented BHO nanorods) and weak pinning centers (random disorder created by BHO nanoparticles, SFs) due to relatively low T_{sub} and high v_{dep}. Therefore, in-field J_cs are higher for T_{sub}=780 °C and 800 °C at 10 K, compared to 820 °C and 840 °C, where the defects in the GdBCO matrix are mostly BHO nanocolumns.

The pinning force density at 77 K (see Fig. 4.14) has a maximum value of 6.6 GNm^{-3} at T_{sub}=820 °C. The characteristic peak in the F_p(B) dependence appears due to the matching effect, when each BHO nanocolumn pins 1 vortex. Similar to the changes in trends of J_c(B) behavior, at 10 K the sample deposited at 800 °C has the highest F_p up to 10 T, but in the 10-14 T region 780 °C shows higher values compared to 800 °C.

The dependence of J_c on the angle (θ) between the *c*-axis of the film and magnetic field is another important characteristic since *RE*BCO-based superconducting thin films are known for $J_c(\theta)$ anisotropy, and for engineering applications it is preferable to possess as much isotropic behavior of J_c as possible.

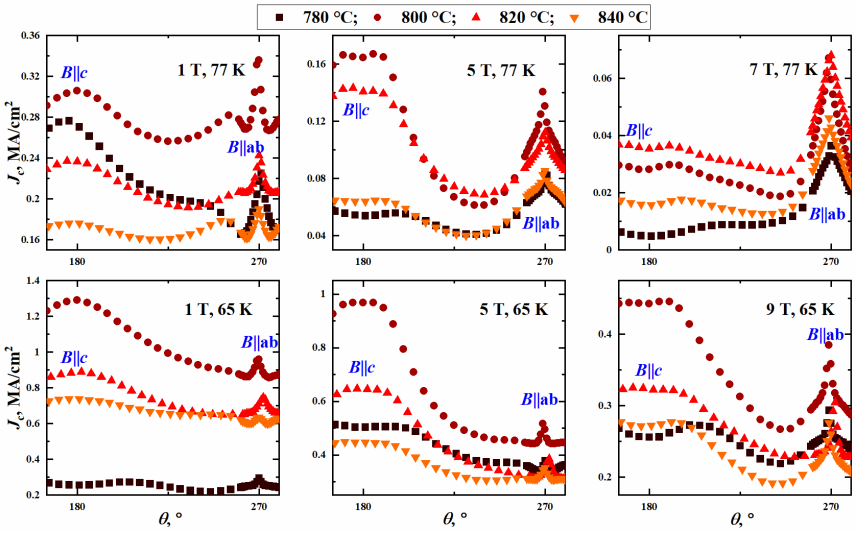

Figure 4.15: $J_c(\theta)$ dependencies for 2.5 wt.% BHO-nanocomposite GdBCO superconducting thin films deposited at 780 °C - 840 °C

The $J_c(\theta)$ dependence (see Fig. 4.15) for samples deposited at T_{sub}=780 °C-840 °C shows a large peak along the *c*-axis direction at 1 T, 77 and 65 K for T_{sub}=800 °C-840 °C with the highest J_c values at 800 °C. At 1 T, 65 K, the *c*-axis peak has the smallest values at T_{sub}=780 °C compared to higher T_{sub}, since at LN_2 temperatures strong correlated pinning centers have a higher contribution towards flux pinning compared to weak pinning centers which are present in GdBCO matrix of 780 °C sample. Additionally, at 1 T, 77 K T_{sub}=800 °C has a shoulder in 235°-270° region. Such shoulder appears as a consequence of the flux pinning on SF and nanoparticles [109]. A peak in *c*-axis direction is present up to 9 T, 77 and 65 K. Changes in the width of *c*-axis peak are caused by variation in nanorod size for different T_{sub}, which results in vortices being pinned by few nanocolumns and stretched among them at intermediate angles between *c* and *ab*-directions [142]. The double-kink ("volcano-like feature") at 180° appears due to the enhanced pinning parallel to the *ab*-plane or by the shortened and tilted nanocolumns in GdBCO matrix [144]

The 2.5 wt% BHO nanocomposite GdBCO thin films deposited at T_{sub}=780 °C-840 °C show that T_{sub} has a direct influence on the defect morphology since it regulates the diffusion rate and, therefore, formation of BHO in GdBCO matrix. At low T_{sub}, the diffusion rate is low and in combination with high v_{dep} leads to a formation of mostly random disorder which is present in the form of strain regions, nanoparticles, short SFs and segmented, short BHO nanorods. Increase of T_{sub} leads to a better alignment of BHO nanocolumns in *c*-axis direction with d≈4-5 nm. The field dependence of J_c and its anisotropy, in accordance with previous studies, reveals that for better in-field performance both at LN_2 and LHe temperatures combination of short nanocolumns and nanoparticles is more favorable since correlated pinning centers can effectively pin vortices at LN_2 temperatures and distortion of GdBCO matrix created by BHO nanocolumns, thus, weak pinning centers contribute to a flux pinning at low temperatures.

4.2.2 Influence of deposition rate

4.2.2.1 Superconducting and structural properties

The variation of v_{dep} has a similar effect on BHO formation as T_{sub}. Decrease of v_{dep} increases the size of the secondary phase nanocolumns similar to the increase of T_{sub}. Here, for studies of influence of v_{dep} on the structural and transport properties in BHO nanocomposite GdBCO thin films, it is varied by the laser frequency. As shown in subsection 4.2.1, the highest in-field J_c is achieved at T_{sub}=800 °C; therefore, all films were deposited at T_{sub}=800 °C, pO_2=0.4 mbar and f=10-2 Hz. After the deposition, all films were cooled to 780 °C where they were oxygenated for 10 min at 400 mbar O_2. After oxygenation all samples were cooled in 400 mbar O_2 atmosphere to RT with 10 °Cmin^{-1}.

Table 4.5: Basic superconducting and structural properties of BHO-nanocomposite GdBCO thin films deposited at f=10, 5 and 2 Hz.

f, Hz	10	5	2
T_c, K	90.2	90.6	87.3
c-axis, Å	11.75	11.75	11.75

BHO nanocomposite GdBCO thin films deposited at f=10, 5 and 2 Hz show GdBCO (00l) peaks in XRD θ - 2θ scans (see Fig. 4.16). The (002) reflection of BHO is present for all three samples. Moreover, the intensity of the BHO (002) and (004) peaks become larger with the reduction of deposition rate which is a possible sign of enlargement of BHO nanoparticles/nanocolumns size in GdBCO matrix. The highest T_c=90.6 K is achieved at f=5 Hz and the lowest 87.2 K at f=2 Hz. The c-axis lattice parameter does not experience any changes with the variation of v_{dep}, which means, due to usage of the exact same oxygen annealing, the changes in T_c are caused by the change of defect morphology in GdBCO matrix.

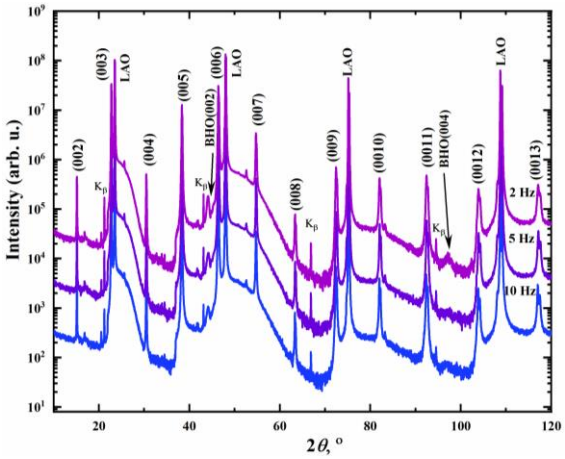

Figure 4.16: XRD patterns of 2.5wt.% BHO nanocomposite GdBCO thin films deposited at f=10, 5 and 2 Hz.

The ILs for the 2.5wt.% BHO containing GdBCO thin films deposited at f=10, 5 and 2 Hz have a characteristic S-shape at 10 and 5 Hz (see Fig. 4.17), which indicates that in these two films BHO has formed nanocolumns aligned in the c-direction. Reduction of v_{dep} does not reduce the matching field for f=5 Hz. The IL of the f=2Hz sample has a less clear S-shape. Such changes in IL behavior appear as a consequence of BHO nanocolumn

diameter change, since the reduction of v_{dep} and increase of the T_{sub} have similar effect on the size of BHO nanocolumns.

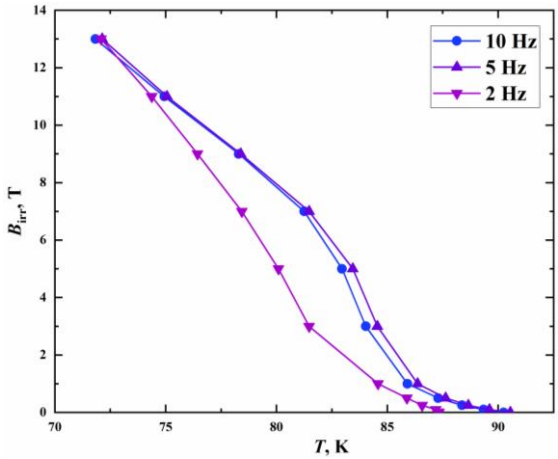

Figure 4.17: ILs of 2.5wt.% BHO nanocomposite GdBCO thin films deposited at f=10, 5 and 2 Hz.

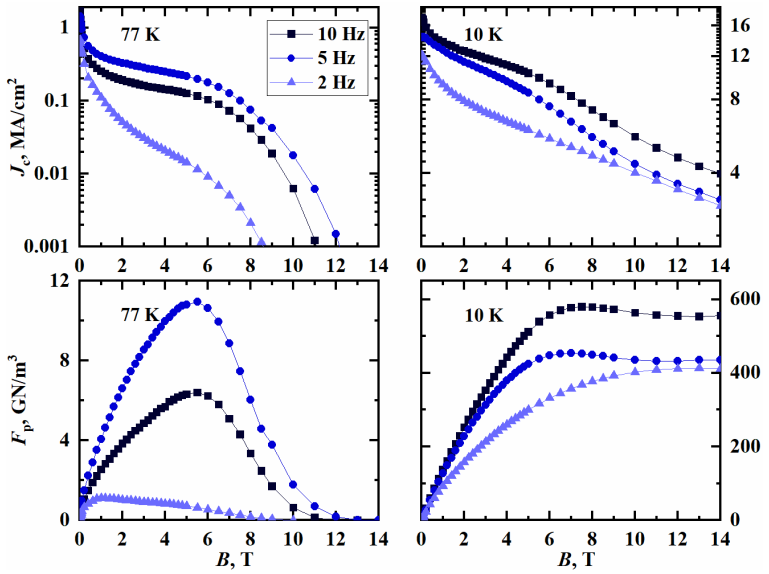

Figure 4.18: J_c(B) and F_p(B) dependencies of 2.5wt.% BHO nanocomposite GdBCO thin films deposited at f=10, 5 and 2 Hz at 77 and 10 K.

Field dependence of J_c (see Fig. 4.18) shows almost 2-fold increase in in-field values at 77 K for the sample deposited at f=5 Hz, while f=2 Hz has the lowest in-field values in the whole range of magnetic fields available at PPMS 14 T measurements system. Similar to the situation with T_{sub}=800 °C and 820 °C, sample deposited at f=10 Hz has the better in-field performance at 10 K since the combination of relatively low T_{sub} and high v_{dep} leads to the formation of both correlated (BHO nanocolumns) pinning centers and random disorder (such as nanoparticles, short SFs, strain region etc.), which contribute to flux pinning at low temperatures and high magnetic fields. $F_{p,max}$=11 GNm^{-3} is achieved by 5 Hz at 77 K, and this value is comparable or lower by a factor of 2 to previous results on *RE*BCO-based superconducting thin films containing BMO secondary phases [88, 91-97].

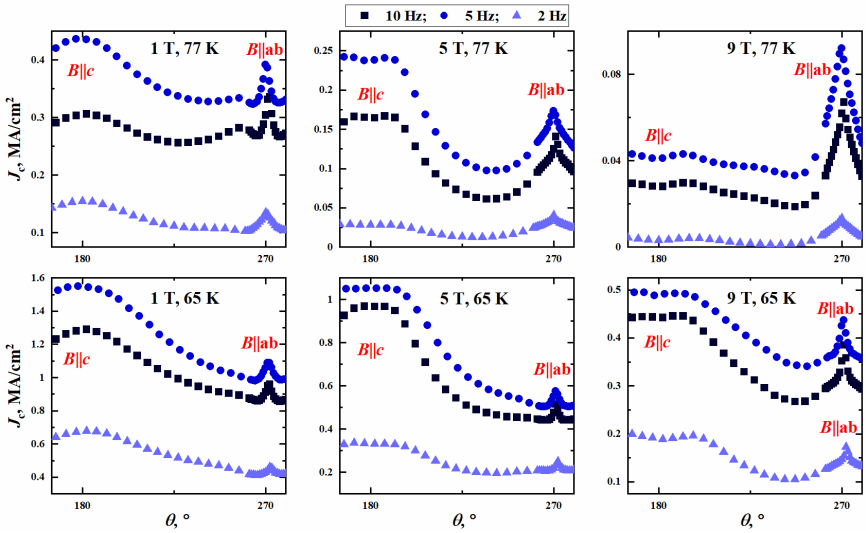

Figure 4.19: J_c-θ characteristics of 2.5wt.% BHO nanocomposite GdBCO thin films deposited at f=10, 5 and 2 Hz at 77 and 65 K.

$J_c(\theta)$ characteristics (see Fig. 4.19) for samples deposited at f=10, 5 and 2 Hz show a large peak in c-axis direction at 1 T, 77 and 65 K, with the highest values for f=5 Hz. Additionally, small shoulders are present at 1 T, 77 K for f=5 Hz and 10 Hz. At 5 T, 77 K $J_c(\theta)$ behavior has a double kink at the c-direction which appears due to splay of nanocolumns. The broadening of the peak around c-axis direction from 5 T to 9 T is caused by vortex pinning by several nanocolumns and correlated with the change in the size of BHO nanocolumns, which indicates that with the reduction of v_{dep} the diameter of BHO nanorods is increasing.

In this chapter, we have shown that considering all transport and structural properties, T_{sub}=800 °C and ν_{dep}=10 Hz is the optimum deposition parameters for 2.5wt.% BHO nanocomposite GdBCO thin films, therefore, these conditions were used to deposit all BHO-nanocomposite GdBCO thin films of Chapter 7. Additionally, in accordance with previous studies on *RE*BCO-based superconducting thin films with BMO nanocomposites, we have shown that the highest in-field J_c both at LN_2 and LHe temperatures are achieved for sample containing combination of correlated pinning centers and random disorder.

5 *In-situ* oxygen annealing of pristine $GdBa_2Cu_3O_{7-\delta}$ superconducting thin films

Various deposition parameters play a crucial role in the formation of defects in *RE*BCO thin film matrix, which has been discussed in Chapter 4. However, another important step in GdBCO thin film preparation is the oxygen annealing. As shown in Chapter 2, the *RE*BCO film has stable tetragonal (T) phase after the deposition, which is an insulator, and oxygen annealing is required to introduce additional oxygen in the structure and form the orthorhombic phase, which is superconducting.

This chapter shows the results of our studies on the influence of the *in-situ* oxygen annealing on the structural and transport properties of pristine GdBCO thin films. This chapter is organized as follows: subsection 5.1 is dedicated to studies of the influence of the annealing temperature (T_{ann}). Based on the results of subsection 5.1, the subsections 5.2 and 5.3 discuss the role that the annealing time (t_{ann}) and oxygen pressure (PO_2) play for the resulting J_c and its anisotropy.

5.1 Influence of annealing temperature

5.1.1 Structural and superconducting properties

All GdBCO thin films were deposited on MgO (100) single crystals in accordance with the optimum conditions explained in Chapter 4. After the deposition, all samples were cooled to the respective T_{ann} in 0.4 mbar oxygen flow with a cooling rate 10 °Cmin^{-1}. After reaching T_{ann}, 400 mbar of oxygen was introduced into the vacuum chamber. T_{ann} was varied between 450 °C-780 °C. According to subsection 2.1.4, t_{ann} was increased from 10 min at 780 °C to 30 min at 450 °C due to the reduction of the diffusion coefficient at lower T_{ann}.

Basic superconducting and structural properties (see Table 5.1) show that compared to GdBCO thin films of Chapter 4, which are grown on $LaAlO_3$ (100) single crystals and annealed at 780 °C, the films on MgO annealed at 780 °C have a much lower T_c (85.2 K vs 92.5 K), this may be an effect of the difference in lattice mismatch between GdBCO/MgO and GdBCO/$LaAlO_3$, hence, of different growth, structure and strain effects

(see subsection 2.3.2). The reduction of T_{ann} leads to an increase in T_c which reaches the maximum value at T_{ann}=450 °C (the lowest investigated T_{ann}). The *c*-axis lattice parameter does not follow the same trend as T_c, since the values stay more or less constant in the investigated temperature range. Such behavior of the *c*-axis lattice parameter is possibly related to the fact that after the deposition and annealing at every T_{ann}, all samples were cooled to RT in the same way i.e., under 400 mbar oxygen atmosphere and, therefore, the possible differences associated to the different T_{ann} vanish. Assuming this, the observed change in T_c is not related to changes in the oxygen content of the samples (this would cause variations in the *c*-axis) but with the strain effects and secondary phases which are forming in the GdBCO matrix.

Table 5.1: Basic superconducting and structural properties of GdBCO thin films annealed at T_{ann}=450 °C-780 °C.

T_{ann}, °C	450	550	650	700	780
T_c, K	92.7	90.9	88.2	84.9	85.2
c-axis, Å	11.737	11.739	11.738	11.738	11.742

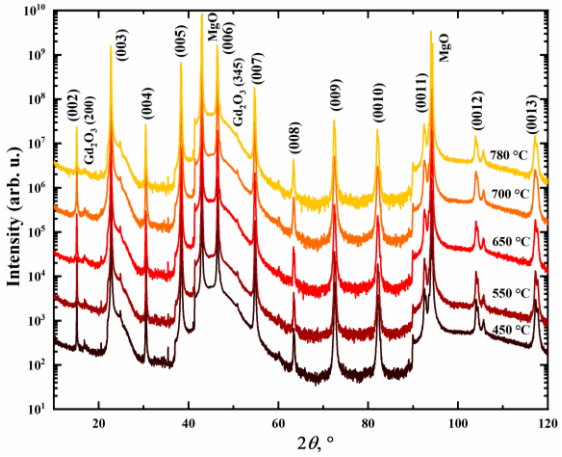

Figure 5.1: XRD pattern of GdBCO thin films annealed at T_{ann}=450 °C-780 °C.

XRD patterns of GdBCO thin films (see Fig. 5.1) shows that all samples have GdBCO (00*l*) reflections which indicates that films are highly *c*-axis oriented. Additionally, reflections from Gd_2O_3 with (200) and (345) orientation are present as well. Rough Scherrer size estimate gives size ≈10-15 nm for (200) reflection and ≈30 nm for (345) reflection.

The AFM images (see Fig. 5.2) display similar features for all films regardless T_{ann}. Similar features were observed in YBCO and GdBCO thin films. Hill-like structures, results of the island-type growth of the films, appear at the surface of all samples. Additional small NPs become visible for T_{ann}≥550 °C.

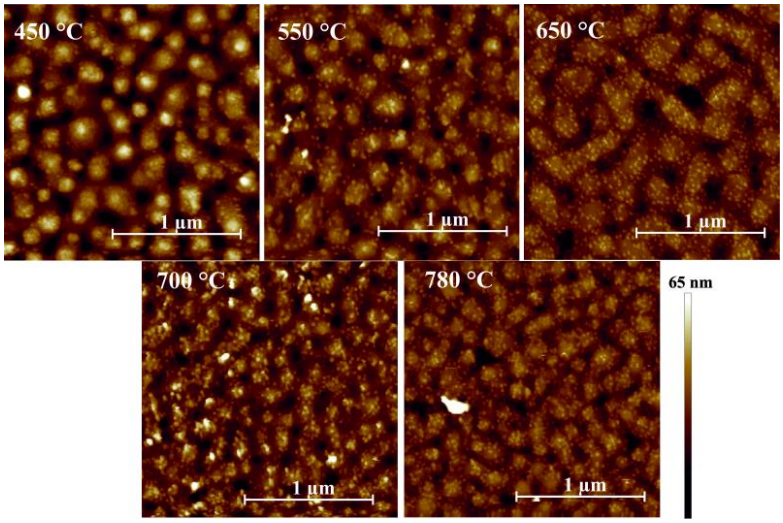

Figure 5.2: Surface images of GdBCO thin films annealed at T_{ann}=450 °C-780 °C.

5.1.2 Transport properties

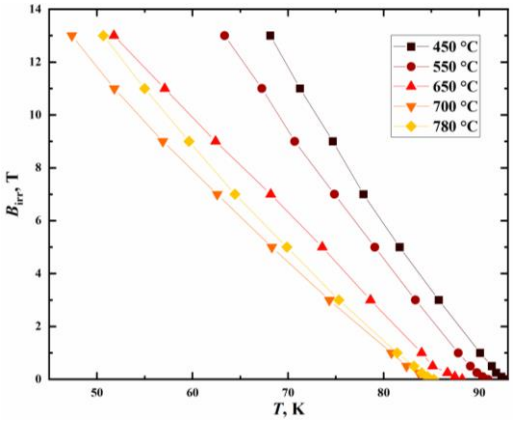

Figure 5.3: ILs of GdBCO thin films annealed at T_{ann}=450 °C-780 °C.

The ILs of the GdBCO thin films annealed at T_{ann}=450 °C-780 °C (see Fig. 5.3) show the typical shape of the IL of pristine *RE*BCO-based superconducting thin films [128, 130]. However, T_{ann} causes changes in the position of the IL. The reduction of T_{ann} from 780 °C to 700 °C moves the IL towards lower fields, but a further decrease to 450 °C causes the contrary effect, reaching the biggest shift at 450 °C. B_{irr} at 77 K has the lowest value of 2.1 T at T_{ann}=700 °C and reaches the highest value of 7.5 T at T_{ann}=450 °C. In the previous studies of transport properties of YBCO and GdBCO superconducting thin films B_{irr} at 77 K is reported to lie within the range 7-9 T for YBCO and GdBCO superconducting thin films. Therefore, values achieved for T_{ann}=450 °C are in a good agreement with previous works.

The field dependence of J_c at 77 and 10 K of GdBCO thin films annealed at 450 °C-780 °C is shown in Fig. 5.4. The samples annealed at 700 °C and 780 °C exhibit the fastest decay of J_c. By decreasing T_{ann} from 700 °C to 450 °C, the in-field J_c increases. The smoothest in-field J_c dependence and the largest self-field J_c are achieved at T_{ann}=450 °C. At 77 K, $F_{p,max}$ is increasing from 0.2 GNm^{-3} to 6.0 GNm^{-3} with the reduction of T_{ann} from 780 °C to 450 °C. $F_{p,max}$ at 77 K, reached for T_{ann}=450 °C, is slightly higher than those previously reported for pristine YBCO thin films [90, 92, 95, 97, 106, 108] and comparable or higher than those previously reported for GdBCO thin films [89, 102, 104, 107, 109]. At 10 K the trend between T_{ann} and resulting in-field J_c stays similar to the trend at 77 K. The highest in-field J_c and F_p at 14 T are achieved for T_{ann}=450 °C.

$J_c(\theta)$ curves (see Fig. 5.5) for GdBCO thin films annealed at 450 °C-780 °C show at 1 and 3 T, 77 K and 65 K for T_{ann}=700 °C and 780 °C only the peak in *ab*-direction while the region around *c*-axis direction is nearly flat. For samples annealed at $T_{ann}\leq$650 °C at 1 and 3 T, 77 and 65 K, another peak in *c*-axis direction starts to appear and reaches its maximum J_c at 450 °C. Such a peak in *c*-axis direction was previously reported for PLD-grown GdBCO thin films on MgO single crystals by T. Matsumoto [128] and was related to flux pinning at a-axis domains and anti-phase boundaries. Moreover, at 1 T, 77 and 65 K the peak in *ab*-direction is increasing from 780 °C to 550 °C and then decreases at 450 °C. Also, in the sample annealed at 450 °C, at 3T, 77 and 65 K, the anisotropy behavior exhibits not only peaks in *c*- and *ab*-direction, but also a shoulder between 235° and 270°. This shape of J_c anisotropy at T_{ann}=450 °C is similar to what was observed for the GdBCO thin film grown at optimum conditions on $LaAlO_3$ single crystals. Therefore, regardless of absence of TEM images in this case, it is possible to conclude by comparing with the previous data from subsection 4.1.4 that at T_{ann}=450 °C ED are the main reason for the appearance of a large peak in *c*-direction, whereas SF and Gd_2O_3 NPs contribute to appearance of shoulder between 235° and 270°.

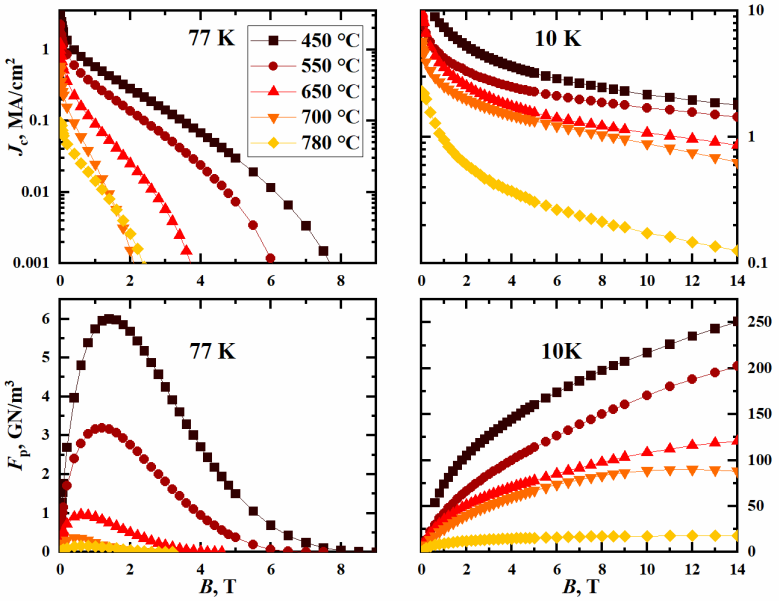

Figure 5.4: Field dependence of J_c and F_p for GdBCO thin films annealed at T_{ann}=450 °C-780 °C.

Considering all features that are observed from structural and transport properties, the behavior of GdBCO thin films may appear due to variations in the density of dislocation loops and ED threading through the whole film. The Gd124 phase i.e., SFs that are usually formed during the film deposition, possibly decompose into a mixture of Gd247+CuO according to [145] at high temperatures and low oxygen pressures, which is further confirmed in studies on influence of post-annealing on J_c in GdBCO thin films [146], exposure to oxygen atmosphere at high temperatures and low pressures reduces the density of SFs. Additionally, the presence of SF in the GdBCO matrix implies dislocation loops [74, 82]. Therefore, films annealed at high T_{ann}=650 – 780 °C may have a small density of large SF, which may also interrupt the domains formed by the ensemble of ED threading through the film, not only causing strain effects, which degrade the superconducting properties. ED, having the core size in the range of the coherence length are effectively pinning vortices around their whole length and contribute towards flux pinning in *c*-direction. Dislocation loops, which primarily lie within the *ab*-plane, can also contribute to flux pinning in *c*-direction [74, 82]. Therefore, decomposition of SF during reduction of T_{ann} from 780 °C to 450 °C possibly results in the larger density of short SF, hence, larger density of defects. Increase in the density of dislocation loops, combined with the presence of domains, which are formed by ED, may be the main reason for the gradual increase of in-field J_c from T_{ann}=780 °C to 450 °C as well as the appearance of the large peak in *c*-direction at T_{ann}=450 °C.

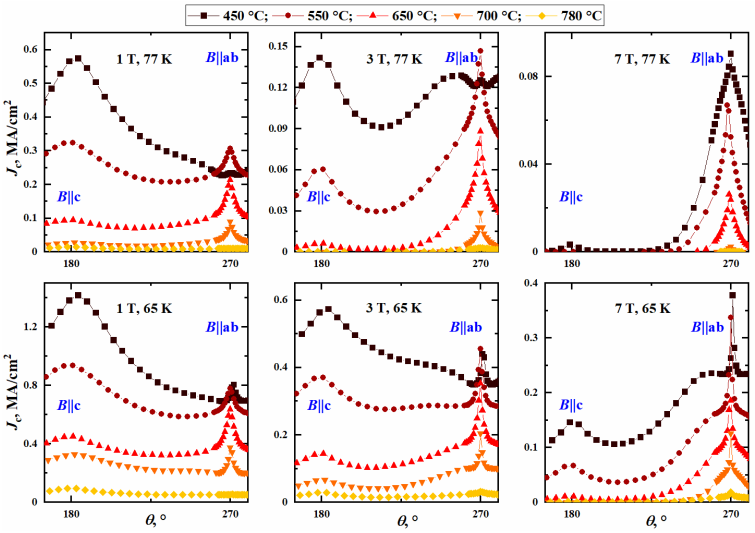

Figure 5.5: $J_c(\theta)$ characteristics for GdBCO thin films annealed at T_{ann}=450 °C-780 °C.

5.2 Influence of annealing time

In subsection 5.1 we have shown that T_{ann} can drastically change the self-field and in-field J_c of pristine GdBCO thin films. However, another important parameter is the annealing time (t_{ann}). In subsection 5.1, t_{ann} was increased from 10 min at 780 °C to 30 min at 450 °C. Now, since it was shown, that the highest in-field J_c are achieved at T_{ann}=450 °C, in this subsection we study how annealing time can further affect the structural and transport properties of pristine GdBCO thin films keeping 450 °C as annealing temperature.

All GdBCO thin films were deposited on MgO (100) single crystals at 800 °C, 10 Hz and 0.4 mbar O_2 flow, in accordance with the optimum conditions of Chapter 4. After the deposition, all samples were cooled to 450 °C in 0.4 mbar O_2 flow with 10 °Cmin^{-1} cooling rate. After reaching 450 °C, 400 mbar of O_2 were introduced into the vacuum chamber. The annealing time was varied between 5 and 60 min. After oxygen annealing at 450 °C, all samples were cooled to RT with 10 °Cmin^{-1} in 400 mbar O_2 pressure.

5.2.1 Structural and superconducting properties

Basic superconducting and structural properties (see Table 5.2) show that by extending t_{ann} from 5 min to 30 min, T_c increases and reaches the maximum value of 92.7 K at t_{ann}=30 min. Larger times cause a small decrease of T_c to 91.9 K. A similar behavior was

previously reported for YBCO thin films [24]. However, in those studies the highest T_c was reached after 7 h.

In accordance with the studies on nonstoichiometry in YBCO thin films [27] and optimum oxygen content reported for GdBCO thin films [32], the GdBCO samples are optimally doped for t_{ann}=15-60 min, reaching the maximum T_c at t_{ann}=30 min, while *c*-axis lattice parameter for t_{ann}=5 min corresponds to the underdoped range, which explains the low T_c observed for this sample. Between 15 and 30 min, the *c*-axis lattice parameters have insignificant differences and still correspond to the optimum oxygen content, while T_c has a drastic change during extension of t_{ann} from 15 to 30 min. Since T_c and *c*-axis lattice parameter are linked to each other, this drastic change could be caused by a change in the microstructure for t_{ann}=15 min (larger defects, strain, higher density of SFs).

Table 5.2: Basic superconducting and structural properties of GdBCO thin films annealed at t_{ann}=5-60 min

t_{ann}, min	5	15	30	60
T_c, K	71.8	84.4	92.7	91.9
c-axis, Å	11.753	11.744	11.737	11.741

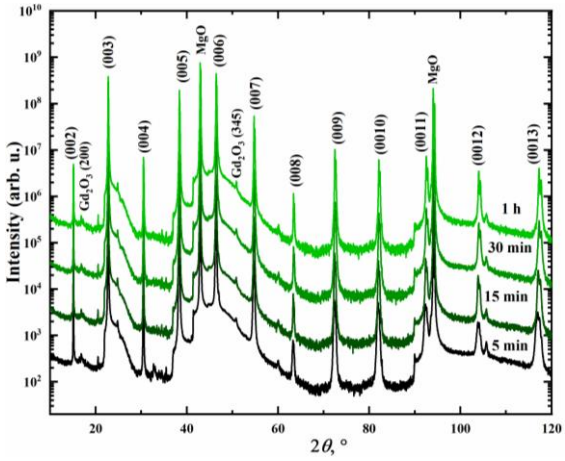

Figure 5.6: XRD θ-2θ scans of GdBCO thin films annealed at t_{ann}=5-60 min.

XRD θ-2θ scans of samples annealed for t_{ann}=5-60 min (see Fig. 5.6) show (00*l*) reflections of GdBCO, and (200) and (345) reflections of Gd_2O_3. The size estimation shows 17-20 nm distribution of Gd_2O_3 (200) for t_{ann}=5-15 min and 7 nm for t_{ann}=30-60 min, while for Gd_2O_3 (345) reflection size is nearly constant ≈30 nm. Due to the absence of TEM images of GdBCO thin films annealed at 450 °C and t_{ann}=5-60 min, from the

crystalline size estimation we assumed that the reason for the T_c reduction at 15 min is the larger size of Gd_2O_3 nanoparticles which disturb the GdBCO matrix.

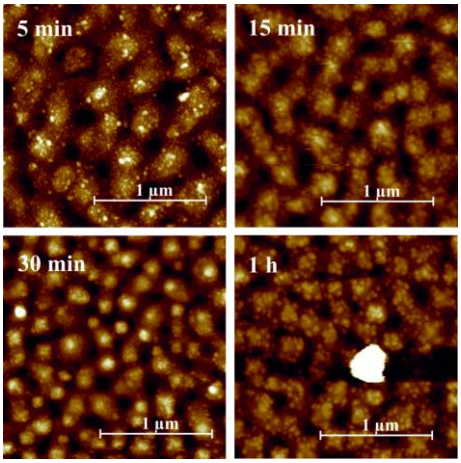

Figure 5.7: Surface images of GdBCO thin films annealed at t_{ann}=5-60 min

AFM images (see Fig. 5.7) show no drastic changes of the surface morphology when t_{ann} increases from 5 to 60 min. All films have a hill-like surface, similar to samples of subsection 5.1.

5.2.2 Transport properties

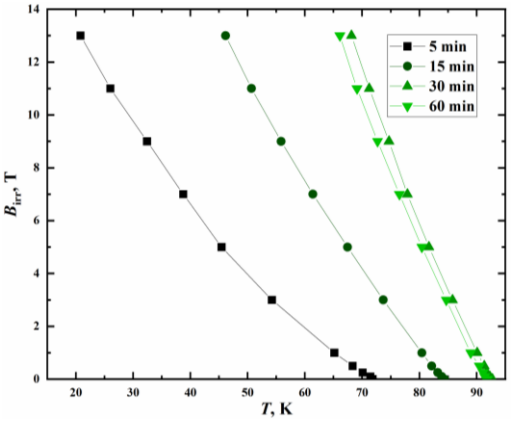

Figure 5.8: ILs of GdBCO thin films annealed at t_{ann}=5-60 min

The ILs of GdBCO thin films annealed for t_{ann}=5-60 min (see Fig. 5.8) show the characteristic behavior with linear dependence of B_{irr} on the temperature which is starting at 0.5 T. The lowest shift as well as the lowest value of B_{irr} has the sample annealed for t_{ann}=5 min. Increase of t_{ann} shifts the IL towards high temperatures and reaches the largest values at t_{ann}=30 min. The highest B_{irr} (77 K) = 7.5 T is achieved at t_{ann}=30 min. The low IL at t_{ann}=5 min is linked to the lower oxygen content of the film which caused worsening of the superconducting properties, at t_{ann}=15 min it is, supposedly, due to large defects that created additional strain on the GdBCO matrix.

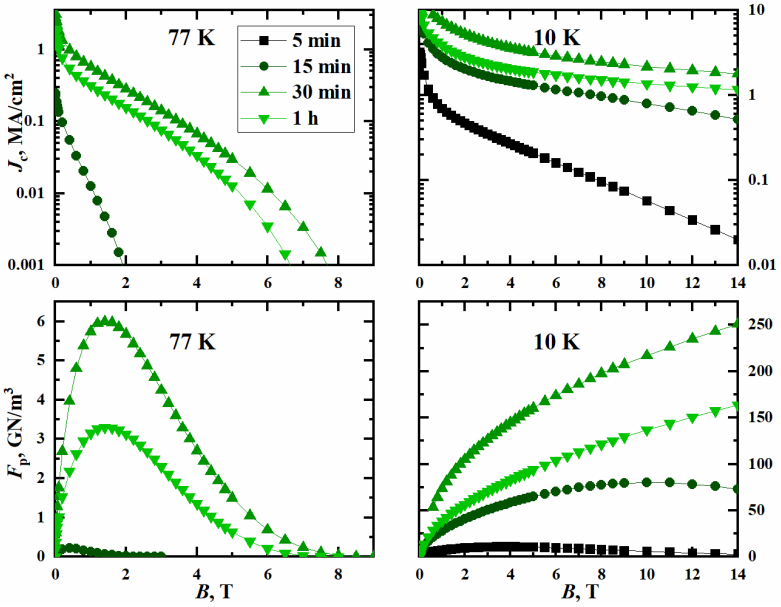

Figure 5.9: Field dependence of J_c for GdBCO thin films annealed at t_{ann}=5-60 min

Similar to the trend observed for T_c, $J_c(B)$ dependence of GdBCO thin films annealed for t_{ann}=5-60 min shows that t_{ann}=15 min has the strongest decay of in-field J_c. Since T_c for t_{ann}=5 min is lower than 77 K, at this temperature the superconducting state has not been reached. The increase of t_{ann} leads to an improvement of in-field J_c with the maximum values achieved at t_{ann}=30 min. A longer exposure to 0.4 bar of oxygen atmosphere slightly reduces in-field J_c. Such behavior of t_{ann}=60 min could result from the slow diffusion processes that are still taking place at 450 °C, thus, possibly causing the reduction of such defects as oxygen vacancies and SFs. In addition, regarding the increase of the Gd_2O_3 NPs size, one could assume that due to slow diffusion and oxygen redistribution SFs i.e., the Gd248 phase is decomposing and participates in the formation of the

Gd123 phase and possibly other oxides. The highest self-field J_c=3.2 MAcm^{-2} is achieved at t_{ann}=30 min. At 10 K, the situation is similar to 77 K regarding the trends with the variation of t_{ann}. The highest in-field J_c are achieved for t_{ann}=30 min, while t_{ann}=5 min has the strongest dependence on magnetic field. Field dependence of F_p (see Fig. 5.9) shows that the highest $F_{p,max}$(77 K)=5.9 GNm^{-3} has t_{ann}=30 min.

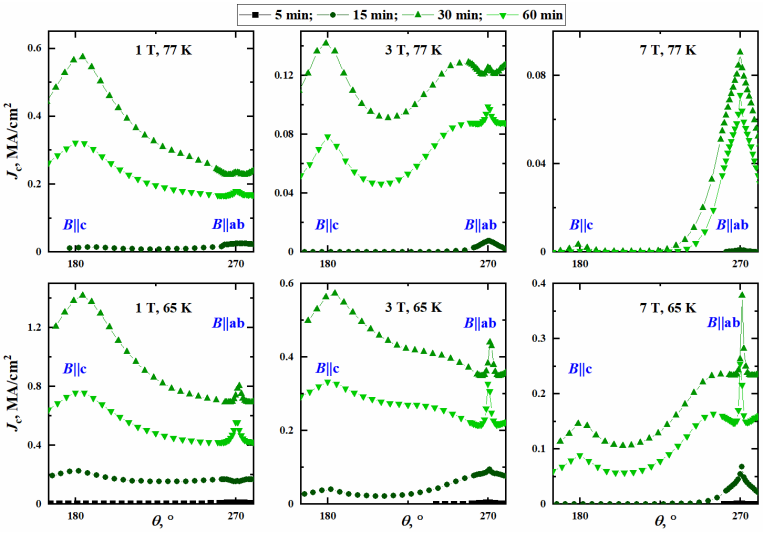

Figure 5.10: J_c (θ) characteristics of GdBCO thin films annealed at t_{ann}=5-60 min.

The $J_c(\theta)$ curves (see Fig. 5.10) for t_{ann}=30 min and 60 min are similar to J_c anisotropies in Chapter 4. These samples have a peak in *c*-axis direction at 1 and 3 T, 77 and 65 K, with the J_c values increasing from t_{ann}=5 min and the highest value for t_{ann}=30 min. The peak in *ab*-direction is increasing from t_{ann}=5 min to t_{ann}=30 min followed by a small reduction at t_{ann}=60 min. Additionally, t_{ann}=30 and 60 min have a shoulder between 235° and 270°. At 7 T, 77 K, GdBCO thin films annealed at t_{ann}=30 and 60 min are close to the transition into a normal state, therefore, the flat region around *c*-axis direction is observed. The shoulders for t_{ann}=30 min and 60 min could be another indication of the changes in the microstructure regarding SF density and oxide NPs.

5.3 Influence of oxygen pressure

In subsections 5.1 and 5.2, we have shown that the highest self-field and in-field J_c are achieved at T_{ann}=450 °C and t_{ann}=30 min. According to [27], the oxygen content which

can be introduced into YBCO is limited by the annealing temperatures and oxygen pressure (PO_2). Therefore, as one of the important parameters of oxygen annealing, the influence of PO_2 on the structural and transport properties of pristine GdBCO thin films was investigated.

5.3.1 Structural and superconducting properties

All GdBCO thin films were deposited in accordance with the optimum conditions of Chapter 4: T_{sub}=800 °C, f=10 Hz, pO_2=0.4 mbar. After the deposition, the films were cooled in 0.4 mbar oxygen flow to 450 °C where they are annealed for 30 min. The oxygen pressure was varied between 0.1 and 1 bar during this annealing. After annealing for 30 min at 450 °C, the samples were cooled to RT in the respective PO_2.

The T_c values and c-axis lattice parameters of the films annealed at PO_2=0.1-1 bar are shown in Table 5.3. The sample annealed at 0.1 bar has the lowest T_c≈86.6 K. By increasing PO_2, T_c enhances and reaches the maximum at PO_2=0.4 bar. Larger values of PO_2 slightly reduce T_c. From the c-axis lattice parameters, it is obvious that independent of PO_2 all GdBCO thin films have optimum oxygen doping, which contradicts the observed T_c values. Therefore, the changes in T_c are caused by modifications of the microstructure by different PO_2 values.

The θ-2θ scans of the films annealed at PO_2=0.1-1 bar show GdBCO (00l) reflections, as well as (200) and (345) reflections of Gd_2O_3 for all samples. Size estimation shows a decrease of the crystalline size from 20 nm to 6 nm for (200) orientation and decrease from 41 nm to 10 nm for (345) orientation for increasing PO_2 from 0.1 to 1 bar. The estimated size of oxide NPs can serve as a confirmation for the behavior of T_c and c-axis lattice parameter. According to [145], the decomposition temperature of the Gd124 phase is dependent on PO_2. Additionally, in [146] it was shown that low PO_2 and high temperature annealing of GdBCO thin films leads to the reduction of the SF density. Therefore, a higher decomposition rate of the Gd124 phase at low PO_2 possibly leads to the formation of the Gd123 phase and larger Gd_2O_3 NPs, while these processes are much slower at high PO_2.

Table 5.3: Basic superconducting and structural properties of GdBCO thin films annealed at PO_2=0.1-1 bar

pO_2, bar	0.1	0.2	0.4	0.6	1
T_c, K	86.6	91.7	92.7	92.5	91
c-axis, Å	11.747	11.740	11.737	11.736	11.746

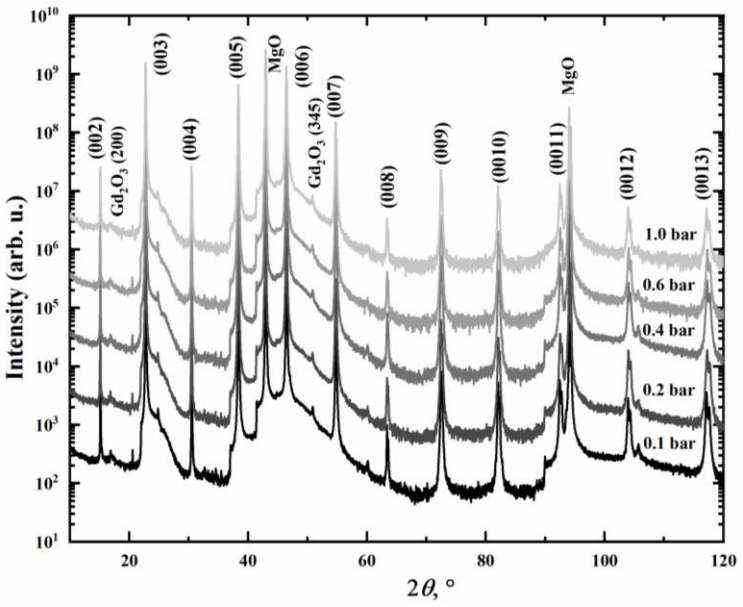

Figure 5.11: XRD θ-2θ of GdBCO thin films annealed at PO_2=0.1-1 bar

The surface morphology of the GdBCO thin films annealed at PO_2=0.1-1 bar is similar to the other annealing parameters. Independent of PO_2, all samples have hill-like surface structure.

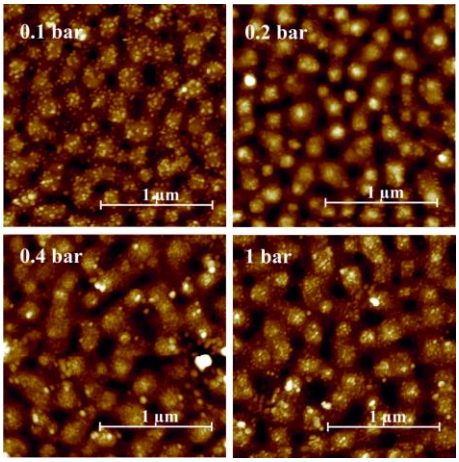

Figure 5.12: Surface images of GdBCO thin films annealed at PO_2=0.1-1 bar

5.3.2 Transport properties

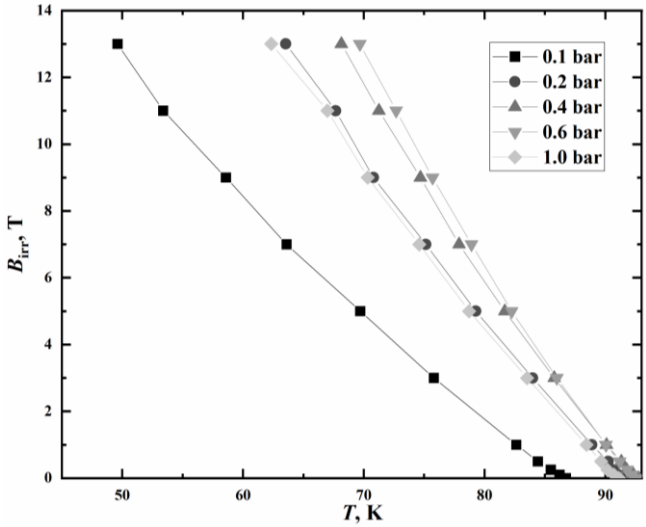

Figure 5.13: ILs of GdBCO thin films annealed at PO_2=0.1-1 bar

B_{irr} at 77 K, which was estimated from the ILs (see Fig. 5.13), has the lowest value of 2.7 T for PO_2=0.1 bar. Increasing PO_2 enhances B_{irr} to the maximum value of 8.1 T at 0.6 bar followed by a slight reduction to 5.8 T at 1 bar.

The field dependence of J_c shows at 77 K the fastest decrease in in-field J_c at PO_2=0.1 bar. Increase of PO_2 leads to increase of in-field J_c. In the region 0-7 T, the sample annealed at 0.4 mbar has the highest in-field J_c while between 7 and 14 T the film annealed at PO_2=0.6 bar has an insignificantly small advantage. At 10 K and in 0-14 T, the sample of PO_2=0.4 bar has the highest in-field J_c, and PO_2=0.1 bar again the strongest dependence on magnetic fields. Similar to the behavior at 77 K, where 0.2 and 1 bar as well as 0.4 and 0.6 bar samples have quite similar J_c in the whole range of magnetic fields, at 10 K, 0.2 and 1 bar have similar in-field J_c. However, the 0.6 bar GdBCO film exhibits a strong reduction compared to 0.4 bar. The angular dependence of J_c (see Fig. 5.15) at PO_2=0.1-1 bar (see Fig. 5.15) is similar to that of GdBCO thin films deposited at optimum conditions on $LaAlO_3$ single crystals (see Chapter 4). At 1 T, 77 and 65 K, PO_2=0.2-1 bar have a large peak in *c*-axis direction, which is increasing from 0.2 to 0.4 bar where it shows the highest J_c, and a peak in *ab*-direction, which is increasing from 0.1 to 0.2 bar, where it reaches the highest J_c and slightly decreases between 0.4 and 1 bar. At 3 T, 77 and 65 K, all samples have a small shoulder between 235° and 270°, which is

most prominent at PO_2=0.4 bar. At 7 T, 77 K, the PO_2=0.1 bar sample is close to the transition into normal state, therefore, flat region around *c*-axis direction is observed.

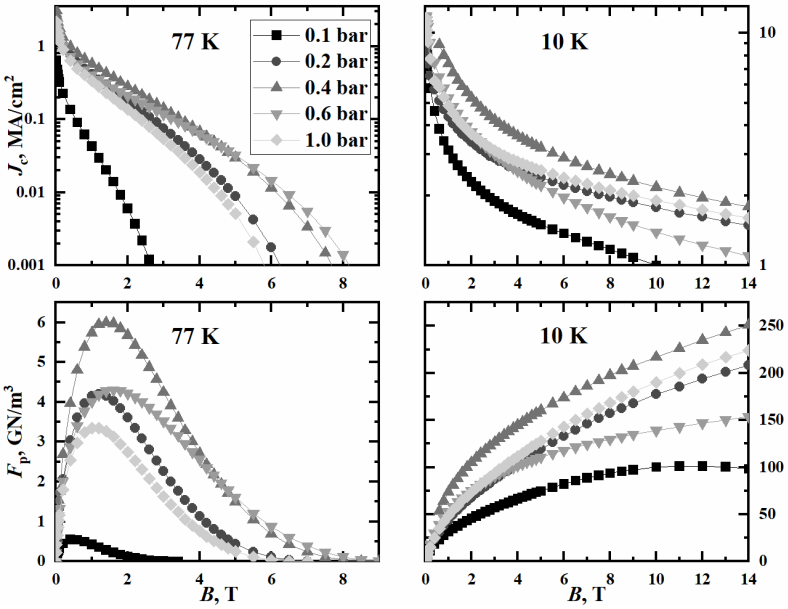

Figure 5.14: Field dependence of J_c for GdBCO thin films annealed at PO_2=0.1-1 bar

Such changes in $J_c(\theta)$ behavior might appear due to SF decomposition at low PO_2, similar to subsection 5.1, and growth/decomposition of Gd_2O_3 NPs as it was observed on data from XRD patterns. Therefore, considering the importance of ED and dislocation loops for flux pinning in pristine *RE*BCO thin films, we assume that the microstructure and, hence, J_c anisotropy behavior can be divided into 3 regions:

1. ***PO*₂≤0.1 bar:** At low PO_2, similar to section 5.1, SF are decomposing, which is possibly the reason for large Gd_2O_3 NPs and the degradation of superconducting properties caused by strain effects. Additionally, a lower SF density implies less dislocation loops present in GdBCO matrix. Thus, these samples exhibit the lower in-field J_c and corresponding $J_c(\theta)$ behavior with the smallest peak in *c*-direction.
2. **0.2 bar≤*PO*₂≤0.6 bar:** Smaller-scale or completely absent SF decomposition, compared to PO_2≤0.1 bar. Considering that the highest in-field J_c is achieved at 0.4 bar, it would seem that PO_2=0.2 bar is the border condition, where SF start to decompose, and PO_2=0.6 bar is for Gd_2O_3 NPs decomposition. The small variations in J_c for field in *c*-direction on Fig. 5.15 appear due to changes in the

density of dislocation loops, while the density of ED threading through the GdBCO film may stay the same. PO_2=0.4 bar is the optimum annealing pressure, since it has optimum density of ED, dislocation loops and Gd_2O_3 NPs, hence, exhibiting the highest J_c.

3. ***PO*$_2$>0.6 bar:** At these conditions, Gd_2O_3 NPs decomposition takes place, therefore, XRD patterns give the smallest size estimation. Therefore, since the SF decomposition is absent, the reduction of Gd_2O_3 NPs size and density may be the reason for further degradation of J_c compared to PO_2=0.6 bar, while the density of ED and dislocation loops may be similar.

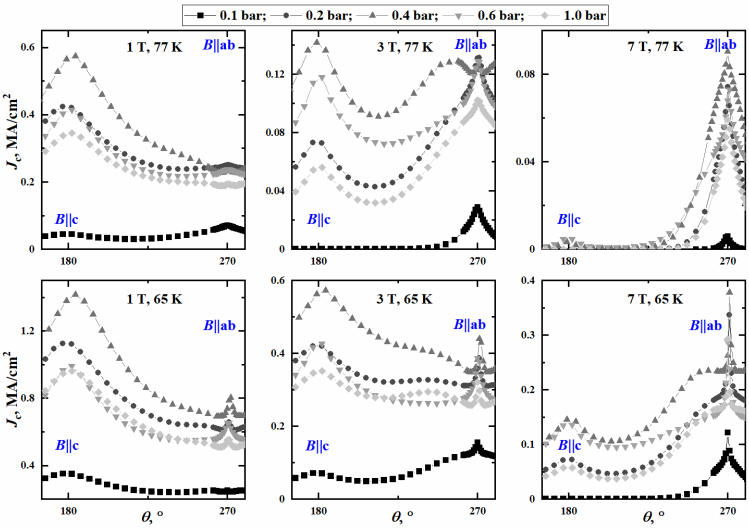

Figure 5.15: $J_c(\theta)$ characteristics of GdBCO thin films annealed at PO_2=0.1-1 bar.

6 *Ex-situ* oxygen annealing of $GdBa_2Cu_3O_{7-\delta}$ superconducting thin films

In Chapter 5 it was shown that oxygen annealing parameters such T_{ann}, t_{ann}, PO_2 of the vacuum chamber have a strong influence on the microstructure and, therefore, on transport properties of pristine GdBCO superconducting thin films. However, due to the existence of a large variety of deposition methods, the oxygen annealing procedures also vary from one approach to another (e.g., oxygen annealing in tubular furnaces for CSD grown samples in our group). Additionally, during production of coated conductors (CC), after the deposition of all buffer and superconducting layers, CC are *ex-situ* annealed in furnaces or tubes. In this Chapter we present results on *ex-situ* (tubular furnace) annealing of pristine GdBCO thin films, correlations between oxygen annealing parameters and defect morphology, and consequently resulting transport properties. Subsection 6.1 is dedicated to comparison of different annealing routes, subsections 6.2, 6.3 and 6.4 show the influence of T_{ann}, t_{ann}, and cooling or quench rate (Q_{PLD}) on structural and transport properties in *ex-situ* annealed pristine GdBCO thin films, respectively.

6.1 Role of annealing route in transport properties improvement of pristine GdBCO thin films

The highest self-field and in-field J_c are achieved at T_{ann}=450 °C, t_{ann}=30 min, PO_2=0.4 bar. Therefore, to figure out which oxygen annealing route is more suitable for *ex-situ* annealing, a preliminary parameter set of T_{ann}=450 °C and t_{ann}=30 min was chosen. On the Fig. 6.1, in addition to three *ex-situ* annealing routes, the temperature profiles for the *in-situ* annealed sample with the highest self-field and in-field J_c and for the sample cooled down to RT in the PLD chamber but without further oxygen annealing are shown. The inclusion of those is necessary to compare *in-situ* and *ex-situ* annealing and keep track of defect morphology changes at various steps.

1. *In-situ* annealing route for the sample with the highest self-field and in-field J_c.
2. No annealing route: GdBCO film cooled at pO_2=0.4 mbar to RT in PLD chamber.
3. Heating to 450 °C with 1200 °Cmin^{-1} in Ar flow. Oxygen annealing for 30 min in 2000 ml/min pure O_2 flow.

4. Heating to 800 °C with a rate of 1200 °Cmin^{-1} in Ar, cooling to T_{ann}=450 °C in Ar flow with 15 °Cmin^{-1}. Oxygen annealing for 30 min in 2000 ml/min pure O_2 flow.
5. Heating to 800 °C in Ar flow with a rate of 1200 °Cmin^{-1}, cooling to T_{ann}=450 °C with 15 °Cmin^{-1} in a mixture of Ar+400 mbar O_2. Oxygen annealing at 450 °C for 30 min with 2000ml/min pure O_2 flow (simulation of *in-situ* annealing in the tubular furnace)

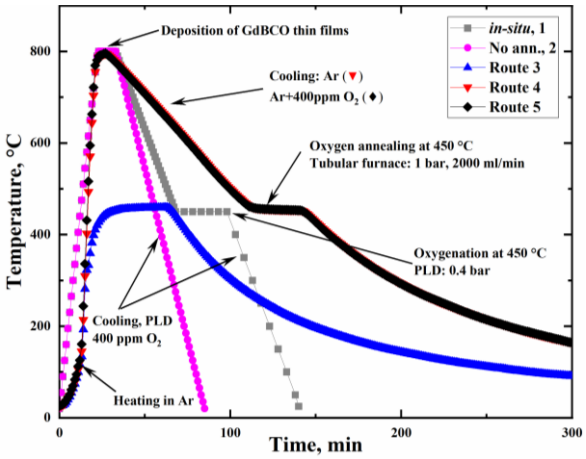

Figure 6.1: Oxygen annealing routes

6.1.1 Structural and superconducting properties

Table 6.1: Superconducting and structural properties of GdBCO thin films annealed at routes 1-5

Ann. route	In-situ, 1	No ann., 2	3	4	5
T_c, K	92.7	32.7	93.1	92.5	93.0
c-axis, Å	11.737	11.811	11.725	11.725	11.728
Gd_2O_3(200), nm	15	40	15	15	15
Gd_2O_3(211), nm	-	-	-	29	30
Gd_2O_3(345), nm	30	30	28	56	9

The investigation of superconducting properties and *c*-axis lattice parameter (see Table 6.1.) have shown that *in-situ* annealed, and route 3-5 samples have a T_c around 93 K and *c*-axis lattice parameters of ≈11.73 Å, which belongs to the optimum oxygen doping

range. The oxygen content, which is linked to the *c*-axis lattice parameter, and which can be introduced into YBCO, is limited by temperature and pressure, therefore, since all samples have a cooling to RT at PO_2=1 bar after annealing at 450 °C for 30 min, the differences are vanished. The sample cooled to RT in the vacuum chamber is underdoped and has a *c*-axis lattice parameters of 11.81 Å and therefore belongs to orthorhombic (O) phase with T_c=32.7 K.

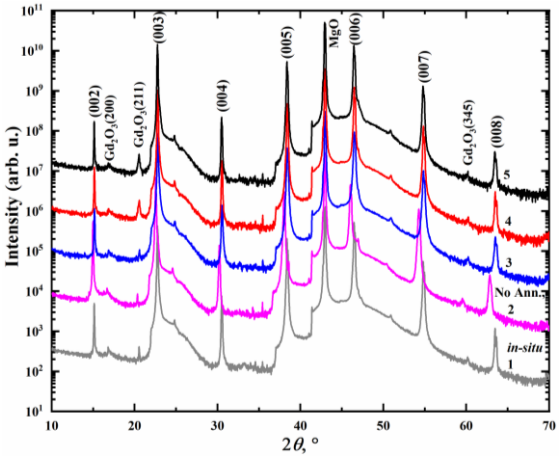

Figure 6.2: XRD patterns for GdBCO thin films annealed at routes 1-5.

XRD θ-2θ show (00*l*) reflections of GdBCO for all the samples. The films of routes 4 and 5 have additional peaks of Gd_2O_3 (200), (211) and (345) orientations. However, orientation (211) is not present for the *in-situ* annealed sample and for routes 2 and 3, which indicates that a possible reason for the formation of Gd_2O_3 (211) is the additional heating step to 800 °C in Ar flow. Rough Scherrer size estimation from (211) reflection of Gd_2O_3 yields ≈30 nm NP size. (200) reflection yields to ≈40 nm for route 2 and ≈15 nm for routes 3-5. The largest variation is seen for (345) reflection: route 2 ≈30 nm, route 3 ≈28 nm, route 4 ≈56 nm, and route 5 ≈9 nm. Additionally, compared to routes 3-5 and *in-situ* annealed GdBCO thin film, the sample cooled to RT in 0.4 mbar has a shift of GdBCO (00*l*) peaks which is appearing as a result of lower oxygen content.

The GdBCO thin films annealed at various T_{ann}, t_{ann} and PO_2 did not show drastic differences in their surface morphology, Chapter 5. Surface images (see Fig. 6.3) for GdBCO thin films annealed at route 2-5 show that cooling to RT leads to a similar surface morphology as many other samples of Chapter 5. The surface morphology of route 3 is similar to that of route 2 with somewhat larger hills. Compared to routes 2 and 3, routes 4

and 5 have triangular shaped precipitates on the surface with approximate size 10-30 nm, which corresponds to estimation from Gd_2O_3 (211) peak.

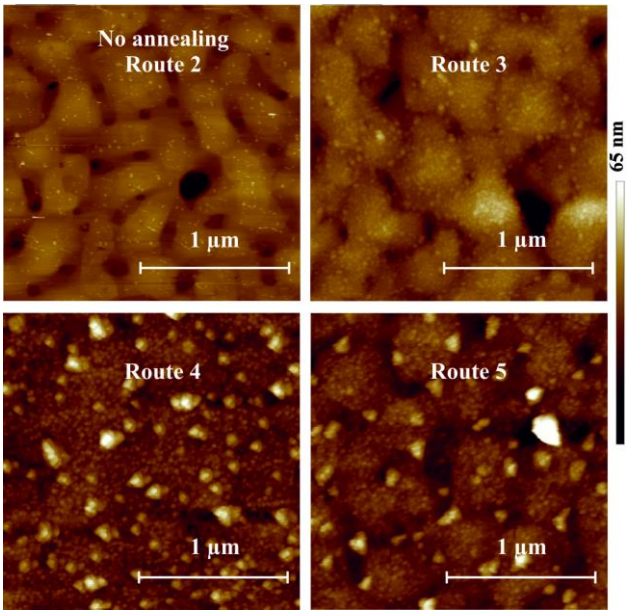

Figure 6.3: Surface images of GdBCO thin films annealed at routes 2-5.

The appearance of the Gd_2O_3 (211) peak in θ-2θ scans and additional triangular-shaped precipitates for *ex-situ* annealed GdBCO thin films of routes 4 and 5 indicates that introduction of additional heating and cooling steps possibly induces the formation of additional Gd_2O_3 NPs both on the surface and in the GdBCO matrix.

6.1.2 Correlation of microstructural features with thermodynamic phases and the irreversibility lines

BF-STEM and LAADF images (see Fig. 6.4) show clearly a presence of domain walls for Route 3 and 4, which are formed by ED, whereas for route 2 and 4 they are less visible but still present. Due to presence of domain walls and threading dislocation, one may expect that this type of defects will be responsible for a large contribution to flux pinning in *c*-direction. Moreover, in addition to ED, Gd-rich NPs, threading dislocations and SFs are present in all samples. The sample annealed at route 3 has predominantly Gd-rich NPs of higher density compared to route 2 and several SFs. Route 4 shows mostly Gd-

rich NPs and threading dislocations. Compared to routes 2-4, route 5 has a larger density of Gd-rich NPs with different orientations, as seen in Fig. 6.4. Additionally, a large density of SFs is present for sample 5, some of the SFs form stair-like structures along 45° direction. The reason of density variations for Gd-rich NPs and SFs and, overall, defect morphology for route 2-5 can appear due to several factors:

Route 2: After the deposition, the GdBCO thin film has predominantly SFs and Gd-rich NPs. Cooling to RT in 0.4 mbar O_2 possibly leads to a partial decomposition of SFs according to [145, 146].

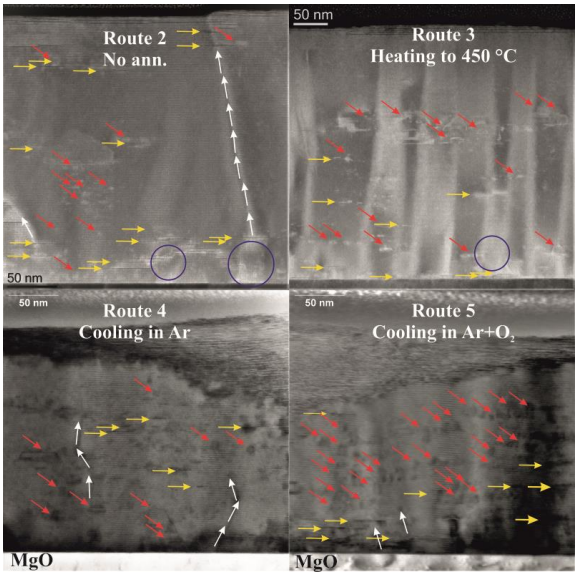

Figure 6.4: BF-STEM and LAADF images of samples deposited at routes 2-5. Red arrows – Gd_2O_3 NPs, yellow – SFs, white arrows – threading dislocations. Blue circles – (l00) outgrowths.

Route 3: SFs, which were formed during deposition, partially decompose during cool-down to RT [145]. Heating to 450 °C in Ar flow relaunches the decomposition process and, additionally, changes the phase from O to T. Switching from Ar flow to the pure O_2 flow stops the SF decomposition and leads to a phase transition from T to O-I, in accordance with the phase diagram proposed by R. Hammond [39]. Due to the stability of the T phase and partial decomposition of SFs, the sample has Gd-rich NPs, which are formed during deposition, and a somewhat reduced SF density, compared to route 2. From the size estimation, it would seem that oxygen annealing at 450 °C and 1 bar O_2 mostly reduces the size of Gd_2O_3 (200).

Route 4: Heating to 800 °C in Ar launches the SF decomposition and changes the O phase to the T phase due to oxygen out-diffusion. Then the original Gd123 phase may decompose into a mixture of Gd163+Gd_2O_3+liquid phases [29], possibly inducing a formation of Gd_2O_3 (211) NPs observed in θ-2θ scans. Further cooling to 450 °C in Ar flow causes severe O_2 out-diffusion and prolongation of the SF decomposition, before annealing at 450 °C. Therefore, this sample has the lowest SF density among routes 2-5. Similar to route 3, annealing at 450 °C and 1 bar O_2 aborts the SF decomposition, starts the Gd_2O_3 decomposition, and changes the T phase to the O-I phase. SFs, which decompose during heating and cooling steps, most likely participate in the Gd123 phase formation and enlargement of the Gd_2O_3 (345) NPs.

Route 5: Similar processes as in route 4 take place. However, due to consecutive cooling to 450 °C in a mixture of Ar+400 ppm O_2 (0.4 mbar of O_2) the decomposition of SFs is less severe. This correlates with the reduced size for Gd_2O_3 (345). Thus, this sample has the largest density of short SFs ≈10-20 nm and a large density of Gd_2O_3 NPs.

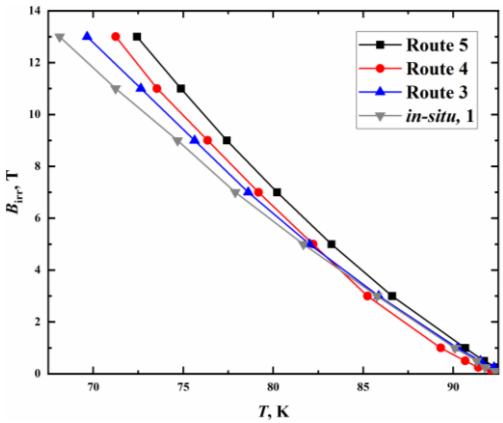

Figure 6.5: ILs for GdBCO thin films annealed at routes 3-5. *In-situ* annealed sample is shown for comparison.

The ILs of GdBCO thin films annealed at routes 3-5 and, additionally, of the *in-situ* annealed film (route 1) (see Fig. 6.5) shows that the highest B_{irr} (77 K) ≈9.3 T is achieved for route 5 while the *in-situ* annealed sample exhibits the lowest B_{irr} (77 K) ≈7.5 T. This indicates that *ex-situ* annealing of GdBCO thin films can improve the transport properties.

6.1.3 Transport properties

After clarifying what is the influence of each annealing route on the defect morphology, it is necessary to determine the resulting field-dependence of J_c, correlation between defects present in each sample and J_c anisotropy. The field dependence of J_c (see Fig. 6.6) of *ex-situ* annealed GdBCO thin films shows a situation similar to the shift of the ILs. The highest in-field J_c values are achieved at route 5 as well as the highest self-field J_c(0 T, 77 K) =3.7 MAcm^{-2}. At 77 K, route 3 has the strongest dependence on magnetic fields. However, J_c for route 3 and for the *in-situ* annealed sample can be considered equal. This may be considered as confirmation of the fact that ED and domains formed by them appear during the deposition process, while the oxygen annealing modifies such defects as SF and Gd_2O_3 NPs. The field dependence of F_p, Fig. 6.6, shows that route 3 has $F_{p,max}$(77 K)=4.4 GNm^{-3}, route 4 has $F_{p,max}$(77 K)=5.5 GNm^{-3}, and route 5 has the highest $F_{p,max}$=6.7 GNm^{-3}. Interestingly, the $F_{p,max}$ for route 5 is similar to those achieved for 2.5wt.% BHO nanocomposite GdBCO thin films of Chapter 4, section 4.2.

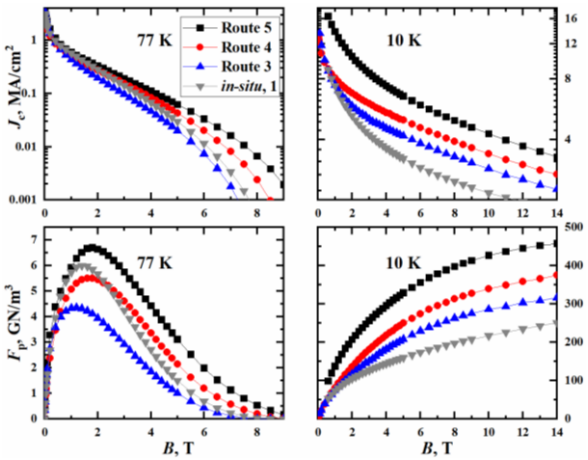

Figure 6.6: Field dependence of J_c and F_p for GdBCO thin films annealed at routes 3-5. Gray dotes represent *in-situ* oxygenated GdBCO films.

The situation changes at 10 K, where the strongest dependence on magnetic fields is shown by the *in-situ* annealed sample and all *ex-situ* annealed samples have higher in-field J_c. The differences between in-field J_c of route 1 and 3, which are more prominent in higher fields, indicate the contribution to flux pinning from a larger density of Gd-rich NPs and SF. Among route 3-5, sample 5 shows the highest in-field J_c in the magnetic field range 0-14 T. Such difference in the field dependence of J_c similar to the situation at 77 K, appears as a result of difference in the density of such defects as Gd-rich NPs and

SF. However, in the low temperature region, weak pinning centers contribute more to flux pinning, and since the route 5 sample is the richest in defects compared to routes 3 and 4, many weak pinning centers might be present in GdBCO matrix.

$J_c(\theta)$ characteristics for the *in-situ* annealed sample and the samples of routes 3-5 (see Fig. 6.7) show a large peak in *c*-axis direction at 1 and 3 T, 77 and 65 K, with the largest J_c values in *c*-axis direction for route 5. Additionally, all samples have a shoulder in 235°-270° region. In accordance with [74, 75, 77], the main contribution towards appearance of a large peak in *c*-direction comes from dislocations and domains formed by them as revealed by BF-STEM images. Considering small differences in J_c, this is caused by the variations of SF density. The reduction of SF density for route 5 affects dislocation loops, which contribute to flux pinning in *c*- and *ab*-directions [83]. Additionally, the differences in the *c*-axis peak as well as the amplitude of the shoulder appear due to differences in SF and Gd_2O_3 NP density. Behavior similar to route 5 was observed in YBCO thin films with excess of Y [147]. Moreover, sample 5 has SFs piled along 45° direction regarding *c*-axis orientation of the film, which can act as columnar defects to pin vortices. Since the sample of route 5 has the largest density of SF and Gd-rich NPs, it has more elevated J_c in the proximity of *c*-axis with a "dome" like shape. Comparing J_c values in the *ab*-direction, it becomes clear that annealing at low pressures and high temperatures reduces the SF density.

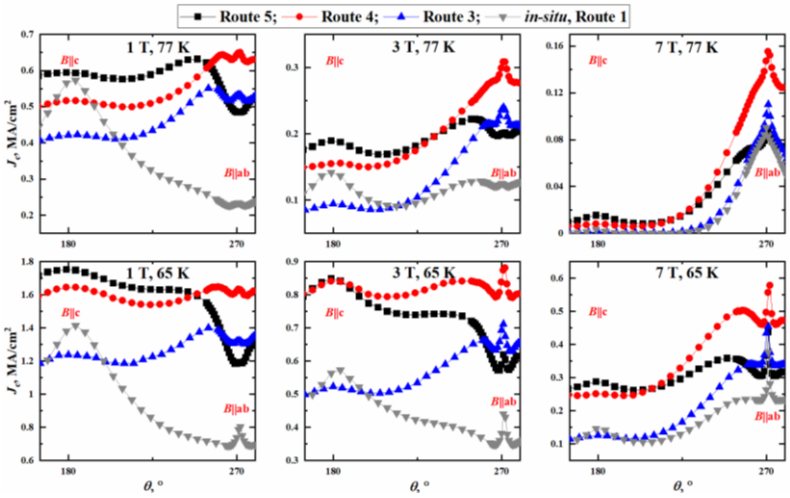

Figure 6.7: $J_c(\theta)$ characteristics of GdBCO thin films annealed at routes 3-5. Gray dotes represent *in-situ* annealed GdBCO thin film.

6.2 Role of annealing temperature for pristine GdBCO thin films

Studies of various oxygen annealing routes have shown that incorporation of heating in Ar atmosphere to 800 °C possibly decomposes the Gd123 phase and forms a mixture of Gd163+Gd_2O_3+liquid phases, thus, inducing the formation of additional Gd-rich NPs in GdBCO, which considerably enhances the transport properties of pristine GdBCO thin films. Therefore, to study the influence of T_{ann}, route 5 was adapted.

All GdBCO thin films were deposited on MgO (100) single crystals according to optimum conditions from Chapter 4. After deposition, all samples were cooled to RT in 0.4 mbar oxygen flow. Consequently, samples were placed in the tubular furnace where, at first, they were heated to 800 °C in Ar flow, afterwards, they were cooled to corresponding T_{ann} in the mixture of Ar and 400 ppm (0.4 mbar) O_2. Similar to *in-situ* annealing (see Chapter 5), T_{ann} was varied between 450 °C and 780 °C and t_{ann} between 30 min at 450 °C and 10 min at 780 °C due to increase of the diffusion coefficient at higher T_{ann}. Oxygen annealing diagrams used for GdBCO thin films are present on Fig. 6.8.

6.2.1 Structural and superconducting properties

Table 6.2: Superconducting and structural properties of GdBCO thin films annealed at 450 °C – 780 °C

T_{ann}, °C	450	550	650	700	780
T_c, K	93.0	92.2	92.6	92.7	92.8
c-axis, Å	11.728	11.728	11.728	11.730	11.731
Gd_2O_3 (200), nm	15	15	15	15	15
Gd_2O_3 (211), nm	30	25	25	26	27
Gd_2O_3 (345), nm	10	10	29	30	31

Regardless of T_{ann} all samples have $T_c \approx 93$ K, Table 6.2. Additionally, all *c*-axis lattice parameters estimated from XRD patterns (see Fig. 6.8) are close to 11.73 Å and belong to the optimum oxygen doping range. As mentioned in subsection 6.1 and chapter 5, regardless of T_{ann} all GdBCO thin films were cooled to RT in 1 bar and 2000 ml/min O_2 flow, therefore, all differences in oxygen content vanished.

XRD patterns (see Fig. 6.8) for GdBCO thin films annealed at T_{ann}=450 °C-780 °C show that all samples have GdBCO (00*l*) peaks with, similar to subsection 6.1, additional peaks from (200), (211) and (345) orientations of Gd_2O_3. The estimated size of Gd_2O_3 NPs was 25-30 nm for (211) reflection, ≈15 nm for (200), and for (345) reflection the size is

increasing from 10 nm at 450 °C to 30 nm at T_{ann}≥650 °C, Table 6.2. Additionally, the intensity of Gd_2O_3 (200) and (345) peaks is reduced at T_{ann}=650 °C-780 °C.

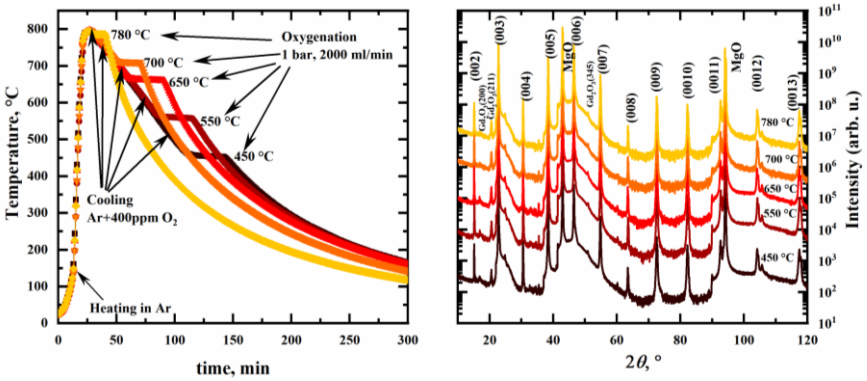

Figure 6.8: Oxygen annealing diagrams and θ-2θ scans for GdBCO thin films annealed at 450 °C-780 °C.

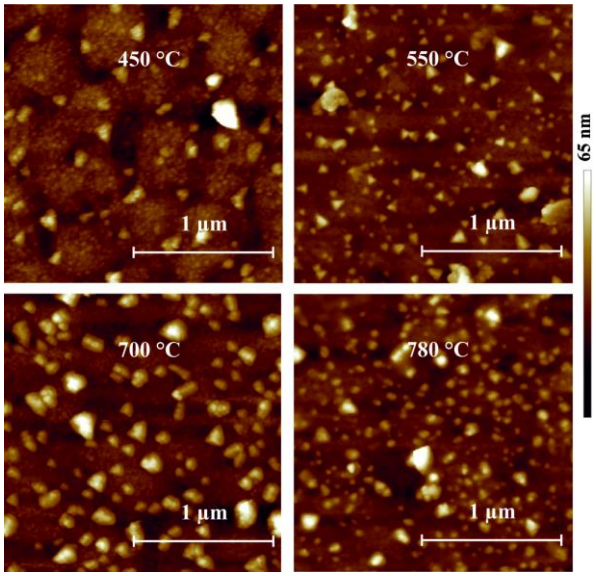

Figure 6.9: Surface images of GdBCO thin films annealed at 450 °C, 550 °C, 700 °C and 780 °C.

Compared to *in-situ* annealing, *ex-situ* annealing at T_{ann}=450 °C-780 °C leads to drastic differences in the surface morphology. At T_{ann}=780 °C, the sample has mostly round precipitates with size 100-300 nm and small precipitates with size ≤50 nm. The reduction of T_{ann} to 700 °C leads to the appearance of particles with size ≈50 nm. At 550 °C, the

sample has many triangular shaped nanoparticles with size corresponding to the estimates of XRD for Gd_2O_3 NPs. At 450 °C, the sample exhibits a clear hill-like surface, which is a clear sign of island-type growth of the thin film, and which is not observed for higher T_{ann}. Similar to 550 °C, T_{ann}=450 °C has triangular shaped precipitates which might be Gd_2O_3 NPs with (211) orientation.

BF-STEM images (see Fig. 6.10) of *ex-situ* annealed samples at T_{ann}=450 °C, 550 °C and 780 °C GdBCO films reveal that even though all samples show presence of domain walls and ED, main changes appear in such defects as SF and Gd-rich NPs, and can be separated into three types in accordance with T_{ann}:

1. **T_{ann}=450 °C:** The sample has a large density of Gd_2O_3 NPs and a large density of short, ≈10-20 nm long SF, due to SF decomposition during cool-down from 800 °C to 450 °C in 400 mbar O_2 and consecutive partial decomposition of Gd_2O_3 NPs during annealing at 1 bar O_2. Oxygen annealing corresponds to O-I phase.
2. **T_{ann}=550 °C:** this GdBCO thin film has mostly Gd_2O_3 NPs and a small density of SF. Such drastic changes compared to other T_{ann} is possibly due to the following:
    a. Similar to 450 °C, SFs decompose during cool-down to 550 °C in 400 mbar O_2.
    b. According to the phase diagrams, during cool-down to 550 °C in 400 ppm O_2 flow, the phase changes from T to O-II. Afterwards at 550 °C and 1 bar O_2 pressure, annealing takes place at the transition line between O-II and O-I phases, which possibly leads to a frustrated growth due to the coexistence of twin domains with different size.
    c. As observed in subsections 5.3 and 6.1, it is possible that increase of PO_2 up to 1 bar stops the SF decomposition and possibly launches the Gd_2O_3 NP decomposition. However, due to close proximity to the O-I and O-II phases and a stressed growth of the Gd123 phase, these processes may be much slower at 550 °C and 1 bar O_2. Moreover, such changes have not been observed for the *in-situ* annealed GdBCO films at 550 °C possibly due to annealing at lower O_2 pressures.

3. **T_{ann}≥650 °C:** These GdBCO thin films have the largest density of 40-50 nm long SFs and just a small amount of Gd_2O_3 NPs. The samples experience a short exposure to high T_{ann} and low PO_2, therefore, only a small fraction of SFs is decomposing. Additionally, reduction of intensity for (200) and (345) orientation of Gd_2O_3 means that at high T_{ann} those Gd_2O_3 NPs dissolve and possibly participate in Gd123 or Gd124 (i.e. SF) phase formations. High T_{ann} and 1 bar O_2 corresponds to oxygen annealing in the O-II phase.

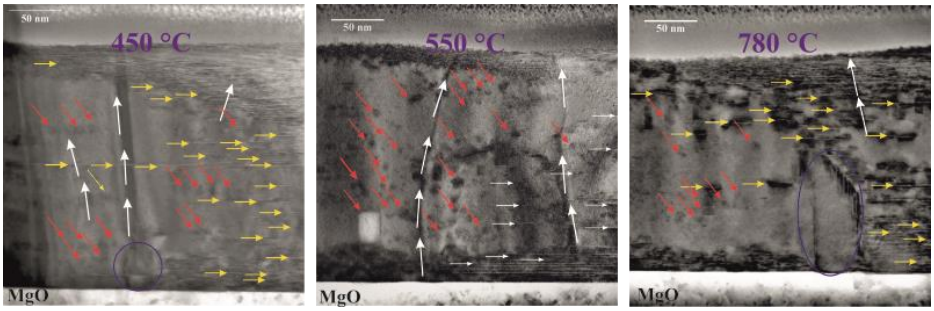

Figure 6.10: BF-STEM images of GdBCO thin films annealed at 450 °C, 550 °C and 780 °C. Yellow arrows indicate SFs, white-threading dislocations, Red-Gd-rich NPs, Blue circles-(*l*00) out-growths.

6.2.2 Transport properties

The highest IL is reached by T_{ann}=450 °C with B_{irr}(77 K)=9.8 T, Fig. 6.11, which is higher than those acquired for *in-situ* oxygen annealing. However, irreversibility fields at 77 K for other samples are very similar. Compared to *in-situ* annealed pristine GdBCO thin films, *ex-situ* annealed samples do not show such large differences in B_{irr}; even at high T_{ann}≥650 °C, the values do not differ that much. For the *in-situ* annealing the lowest value was shown by the sample annealed at T_{ann}=780 °C. In both annealing methods the highest IL is achieved at T_{ann}=450 °C, which indicates that low temperature annealing is preferable for better in-field performance of the GdBCO thin films.

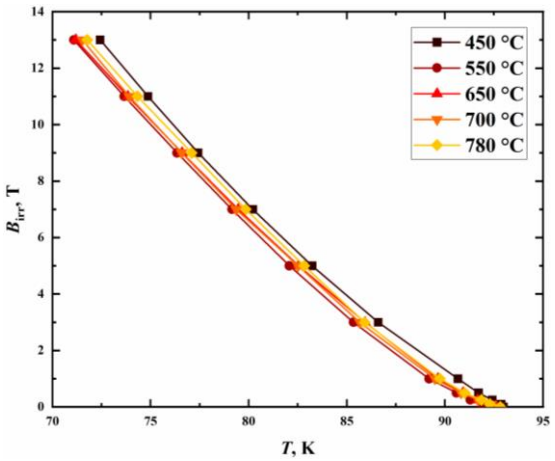

Figure 6.11: ILs for GdBCO thin films annealed at 450 °C-780 °C.

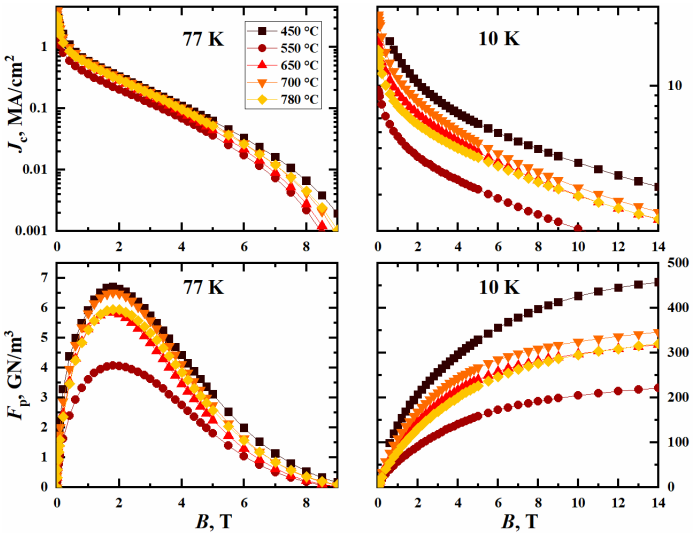

Figure 6.12: J_c (B) dependence for *ex-situ* annealed GdBCO thin films at T_{ann}=450 °C-780 °C.

The $J_c(B)$ behavior (see Fig. 6.12) of GdBCO thin films annealed at 450 °C-780 °C shows strong deviation from the *in-situ* case. At 77 K, all samples have close in-field J_c values, however, T_{ann}=450 °C can be considered as the best sample. $F_{p,max}$(77 K)=6.9 GNm^{-3} is achieved at T_{ann}=450 °C, while T_{ann}=550 °C has the lowest $F_{p,max}$=4.3 GNm^{-3}. The situation drastically changes at 10 K: While for *in-situ* annealed GdBCO thin films at low temperatures the trend in J_c with T_{ann} was similar to 77 K, for *ex-situ* annealed samples this trend is absent. The highest self-field and in-field J_c is shown by T_{ann}=450 °C, and T_{ann}=550 °C has the strongest dependence on magnetic fields. High $T_{ann}\geq$650 °C yield in-field J_c between those for 450 °C and 550 °C. Such variation in J_c behavior can be attributed to differences in defects present in GdBCO matrix of each sample as well as their density. Another important feature (see Fig. 6.12) is $F_{p,max}$, which for all *ex-situ* annealed samples appear at B=1.8 T, in contrast to the *in-situ* annealed films. This might indicate that at 1.8 T the density of flux lines matches the density of linear defects, such as ED. Therefore, we may conclude that the ED and domain walls formed by them appear in the film during the deposition process, and oxygen annealing primarily affect the Gd_2O_3 NPs and SF. In case of the *in-situ* annealed film at $T_{ann}\geq$700 °C, exposure to high temperatures possibly affects LAB and domains, thus, reducing the density of linear defects and, therefore, shifting $F_{p,max}$ towards lower B. Additionally, in the low temperature region, weak pinning centers play a more important role due to their contribution to flux pinning. The highest value of F_p (10 K, 14 T) =457 GNm^{-3} is achieved at 450 °C. Compared to the *in-situ* annealed sample at 450 °C, this value is higher by a factor of 2, which indicates that *ex-situ* oxygen annealing can be used as an additional tool for J_c

improvement of *RE*BCO-based superconducting thin films. Moreover, compared to previous studies on transport properties in heavily Zr-doped YBCO thin films [99], this value is lower by only a factor of 2.

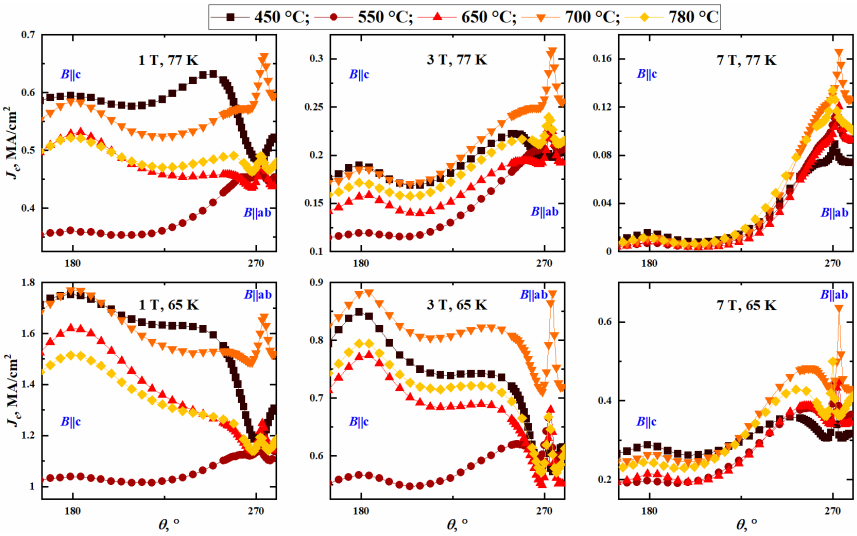

Figure 6.13: J_c (θ) characteristics for *ex-situ* annealed GdBCO thin films at T_{ann}=450 °C-780 °C.

$J_c(\theta)$ characteristics (see Fig. 6.13) shows that the behavior of J_c anisotropy can be separated into 3 types in accordance with the changes in the density of Gd_2O_3 NPs and SF (see Fig. 6.9):

1. **T_{ann}≤450 °C:** The GdBCO film exhibits a large peak in *c*-axis direction, appears due to flux pinning on ED threading through the GdBCO film, with the largest shoulder between 235° and 270° than it is seen at 550 °C-780 °C. Compared to other T_{ann}, the sample has a dip in the *ab*-direction at 1 T, 77 and 65 K. This dip at T_{ann}=450 °C appears due to reduction of the pinning potential on the spherical defects (in this case Gd_2O_3 NPs) [109], thus, resulting in the J_c depression in *ab*-direction. Additionally, the film has short SFs, some of which create a step-like structure along 45°, which can contribute to the vortex pinning between 235° and 270°.
2. **T_{ann}=550 °C:** This sample shows presence of a small peak in *c*-axis direction and a shoulder between 235° and 270°. Such behavior is the result of presence of dislocations and mostly Gd_2O_3 NPs with much lower density of SF.
3. **High temperature region T_{ann}≥650 °C**: $J_c(\theta)$ has a large peak in *c*-axis direction at 1 and 3 T, 77 K and 65 K as well as a peak in the *ab*-direction with the largest

J_c values achieved at 700 °C for both directions. Additionally, all high T_{ann} samples have a shoulder in the region 235°-270°. Such anisotropy behavior for T_{ann}≥650 °C samples appear due to flux pinning on ED and domains formed by them, which gives the appearance of a large peak in *c*-direction. However, the presence of predominantly planar defects in GdBCO matrix implies that there are dislocation loops, which give rise to the peak in *ab*-direction [83], and possibly also contribute to flux pinning in *c*-direction. Additionally, due to the presence of a small amount of Gd_2O_3 NPs, combined pinning on spherical and planar defects gives a somewhat smaller shoulder between 235° and 270°.

Comparison of *in-situ* and *ex-situ* oxygen annealing at various T_{ann} for pristine GdBCO thin films reveals that both methods have similarities regarding the correlation between highest achieved in-field J_c and T_{ann}. Both methods require low temperature (T_{ann}≤450 °C) oxygen annealing to achieve better in-field performance. $J_c(\theta)$ characteristics for both oxygen annealing methods exhibit a large peak in *c*-axis direction at 1 T, 77 K. which implies strong influence of ED threading through the GdBCO films on flux pinning. However, from the features observed on field dependence of J_c and F_p, it becomes clear that this type of defects is formed during the deposition process, and the oxygen annealing is primarily affecting Gd_2O_3 NPs (see section 5.3) and SF (see section 6.1). Thus, the main advantage of *ex-situ* oxygen annealing is an introduction of additional cooling and heating steps since it induces the formation of additional defects in the GdBCO matrix and increases J_c. Additionally, in case of *in-situ* annealing a clear trend of J_c increase with the reduction of T_{ann} was observed, while for *ex-situ* annealing at 77 K samples have close J_c values and the main difference appears at low measurement temperatures, where *ex-situ* annealed samples show lack of trend. Another feature which is common for both annealing methods is the behaviour at 550 °C. In case of *in-situ* annealed GdBCO films, the SFs decompose during cooling at high T_{ann} and low pO_2, which possibly stops around 550 °C, thus, creating the GdBCO thin films with a large density of short SFs and Gd-rich NPs. A similar process takes place in case of *ex-situ* annealed samples. However, *ex-situ* annealed GdBCO film also experiences a stressed growth as mentioned above due to competition between twin domains of O-I and O-II phases. Therefore, it is possible to assume that due to these SF decomposition processes during *in-situ* and *ex-situ* oxygen annealing, for both approaches at T_{ann}=450 °C we acquire GdBCO films with rich pinning morphology consisting of ED, domains, short SFs and Gd-rich NPs.

6.3 Role of annealing time for pristine GdBCO thin films

In subsection 6.2 we have studied the influence of T_{ann} on structural and transport properties in *ex-situ* annealed GdBCO thin films. To further improve the in-field performance of GdBCO thin films, annealing at low temperature with additional cooling and heating steps is preferable, since such an annealing procedure induces formation of NPs in GdBCO matrix. Similar to *in-situ* annealing, the 2nd annealing parameter which was taken into consideration is the annealing time t_{ann}. In this subsection we present the influence of t_{ann} on structural and transport properties.

GdBCO thin films were deposited in accordance with optimum conditions (see Chapter 4). After the deposition, all samples were cooled to RT in 0.4 mbar O_2 flow with cooling rate 15 °Cmin^{-1}. Afterwards, all samples were placed in the tubular furnace, where at first, they were heated to 800 °C in Ar flow and then cooled to 450 °C in the mixture of Ar and 400 ppm O_2. At this point, pure O_2 flow at 1 bar and 2000ml/min was introduced into the tubular furnace. Annealing time was varied in the exact way as for *in-situ* annealed GdBCO thin films between 5 and 60 min, but with addition of t_{ann}=120 min.

6.3.1 Structural and superconducting properties

Table 6.3: Basic superconducting and structural properties of GdBCO thin films annealed at t_{ann}=5, 15, 30, 60 and 120 min.

t_{ann}, min	5	15	30	60	120
T_c, K	93.4	93.3	93.1	93.2	92.9
c-axis, Å	11.724	11.723	11.722	11.722	11.724

In contrast to *in-situ* annealing, all *ex-situ* annealed samples have *c*-axis lattice parameter around 11.72 Å independent of t_{ann}, which corresponds to the optimum oxygen content for GdBCO thin films. T_c values of GdBCO thin films annealed at 5-120 min do not exhibit drastic differences, and all values are distributed around 93 K. *In-situ* annealing leads to a much more severe reduction in T_c when t_{ann} is reduced from 30 to 15 min and further to 5 min. This shows that these two annealing methods possibly have different oxygen in-diffusion rates. Such changes may appear due to the dependence of the diffusion coefficient on the concentration, which in the tubular furnace has a permanent supply, while in PLD chamber is constant. Moreover, compared to *in-situ* oxygen annealing, *ex-situ* oxygenated samples undergo two additional cooling (in-diffusion) and heating (out-diffusion) steps, which in accordance with previous works on oxygen in- and

out-diffusion in YBCO [19] leads to a faster oxygen in-diffusion. Therefore, the combination of fast oxygen in-diffusion and cooling to RT at 1 bar pure O_2 flow results in an optimum oxygen content in all *ex-situ* annealed GdBCO thin films.

All GdBCO thin films annealed at t_{ann}=5-120 min (see Fig. 6.14) have (00*l*) reflections of GdBCO indicates highly *c*-axis oriented films. Similar to samples from subsection 6.2, Gd_2O_3 peaks with orientation (200), (211) and (345) are present as well. Rough Scherrer estimation points to a decrease in size from 20 to 10 nm for (200) orientation with increase of t_{ann}, (211) leads to the ≈30 nm size for Gd_2O_3 NPs, and (345) orientation have ≈40 nm size.

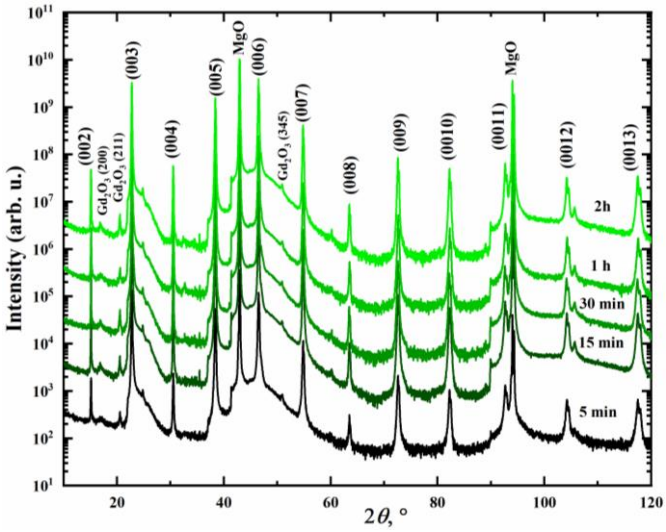

Figure 6.14: XRD θ-2θ scans of GdBCO thin film annealed at t_{ann}=5-120 min.

Surface morphology of GdBCO thin films annealed at t_{ann}=5-120 min (see Fig. 6.15) is similar to those of subsection 6.2 for T_{ann}=450 °C, all samples exhibit a clear hill-like surface, which appears due to island growth of the film. Moreover, all films have triangular shaped precipitates on the film surface, which are possibly Gd_2O_3 NPs with (211) orientation formed during heating to 800 °C procedure. At t_{ann}=5 min, a large density of small precipitates is present, which become less visible at t_{ann}=15 min.

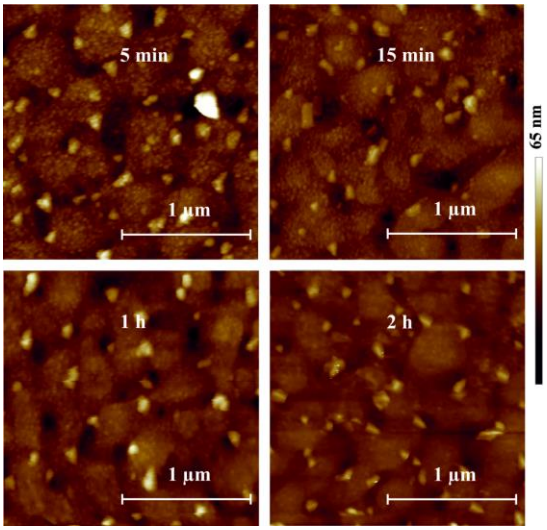

Figure 6.15: Surface images of GdBCO thin film annealed at t_{ann}=5-120 min.

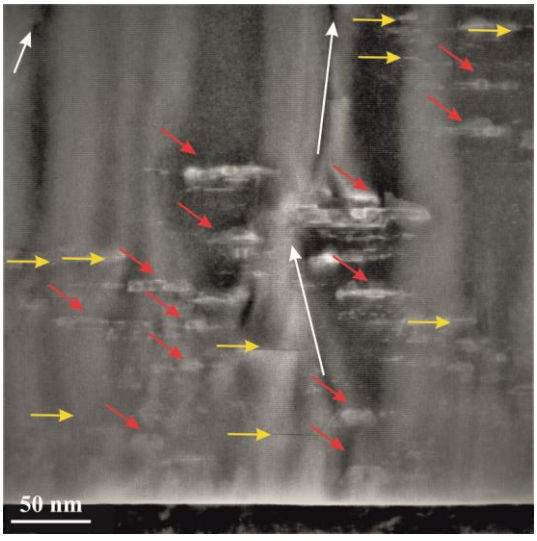

Figure 6.16: LADDF image of GdBCO thin films annealed at t_{ann}=15 min. Red arrows - Gd-rich NPs, yellow arrows – SFs, white arrows – threading dislocations.

An LAADF image of the GdBCO thin film annealed at t_{ann}=15 min (see Fig. 6.16) shows clear presence of domain walls formed by ED and threading dislocation. Additionally, plate-like NPs with the size 30-50 nm which corresponds to estimations of Gd_2O_3 secondary phases from XRD patterns as well as SF.

6.3.2 Transport properties

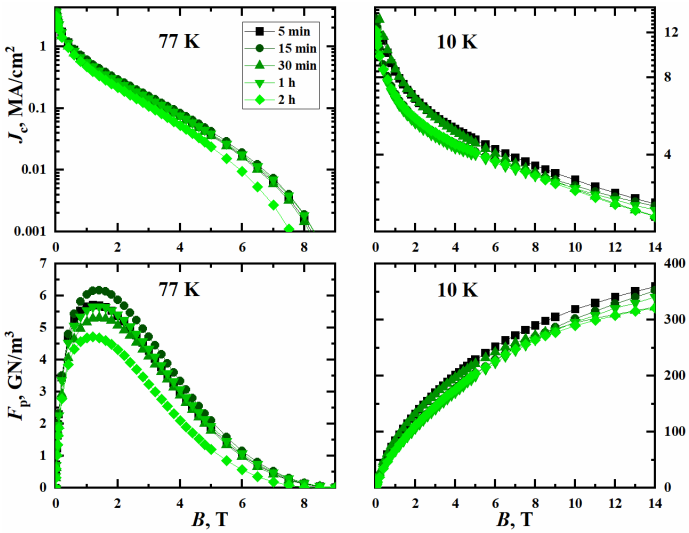

Figure 6.17: Field dependence of J_c and F_p for GdBCO thin films annealed at t_{ann}=5-120 min

Self-field and in-field J_c is very similar for t_{ann}=5-60 min, whereas t_{ann}=120 min has a slightly lower J_c at high magnetic fields, which however can be disregarded, see Fig. 6.17. The change in J_c values at t_{ann}=120 min may appear due to a "healing effect" during the long exposure to oxygen. Long annealing possibly removes point-like defects such as oxygen vacancies in the GdBCO thin film and, additionally, at these temperatures diffusion processes can still take place regardless of relatively low T_{ann}. Therefore, one could expect that within 120 min of oxygen annealing some variations in size and density of SF and Gd_2O_3 NPs might appear. Corresponding decrease in size of Gd_2O_3 secondary phases have been observed from XRD patterns for (200) orientation. Compared to *ex-situ* annealing, *in-situ* annealed GdBCO thin films (see Chapter 5) show a large variation of in-field J_c and stronger dependence on magnetic fields. In case of *in-situ* annealing, GdBCO thin films require at least 15 min of exposure to the oxygen atmosphere. The difference in both annealing methods can be explained by Fick's law and the dependence of the diffusion coefficient on temperature. In the large volume of the PLD chamber, during the oxygen annealing, 400 mbar of O_2 are sealed without any additional supply. Additionally, a temperature gradient is existing inside the PLD chamber, since 450 °C are kept only on the heater itself. Therefore, the diffusion coefficients and the velocity of gas molecules might exhibit gradients. Compared to *in-situ* annealing, in the tubular furnace a thermocouple is placed right above the film, which provides more uniform temperature distribu-

tion. In the tubular furnace oxygen is supplied continuously with the rate 2000 ml/min. Moreover, as mentioned in the previous subsection, oxygen out-diffusion before the annealing at 450 °C increases the rate of oxygen in-diffusion. Considering all these facts, *ex-situ* oxygen annealing gives similar in-field J_c since optimum oxygen content is reached within a short period of time after which prolongation of the exposure to the oxygen atmosphere can slightly modify the microstructure of the film. At 10 K, GdBCO thin films annealed at t_{ann}=5-120 min show similar in-field J_c values. Small differences can be noticed in the low-field region (0-4 T) for samples annealed for 60 and 120 min. The $F_{p,max}$(77 K) increases from 5.7 GNm^{-3} at t_{ann}=5 min to 6.1 GNm^{-3} at t_{ann}=15 min, afterwards it slightly drops at 30 and 60 min and reaches the lowest value 4.8 GNm^{-3} at t_{ann}=120 min. The small variation in $F_{p,max}$ might be caused by slight changes in the defect morphology during long annealing times as well as small variations in the microstructure from one thin film deposition to another.

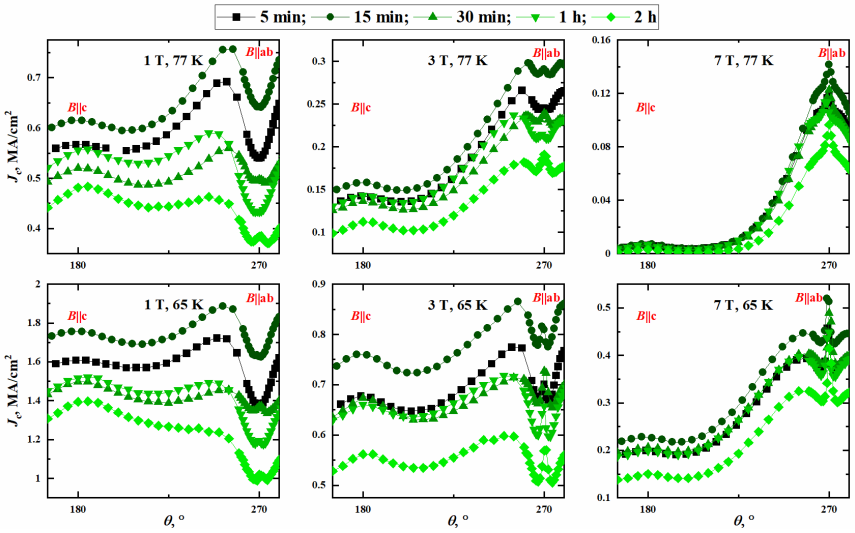

Figure 6.18: $J_c(\theta)$ characteristics for GdBCO thin films annealed at t_{ann}=5-120 min

$J_c(\theta)$ characteristics (see Fig. 6.18) of all these samples are very similar. At 1 T, 77 and 65 K GdBCO films have a large peak in *c*-axis direction, large shoulders in 235°-270° region and a dip in the *ab*-direction. As mentioned above, such behavior appears due to flux pinning on ED and presence of both spherical NPs and SF. However, similar to the field dependence of J_c, small variations in the behavior of J_c anisotropy can be related to longer t_{ann} as well as variations which appear during the thin film deposition.

One of the assumptions for the worsening of transport properties for various t_{ann} during *in-situ* oxygenation was the presence of strain due to large defects. Therefore, it would seem that additional heating and cooling steps for *ex-situ* oxygen annealing participate in the release of stress on GdBCO matrix, which was created in GdBCO during the deposition. Thus, as mentioned in Chapter 2, this might cause the formation of "short circuits" for oxygen in-diffusion which in combination with the reasons mentioned in subsection 6.3.1 may explain the short t_{ann} required for *ex-situ* oxygen annealing.

6.4 Role of PLD chamber cooling rate in *ex-situ* annealing procedure

Another parameter which attracted our interest and can have an influence on the in-field J_c of GdBCO thin films is the cooling rate at 0.4 mbar pO_2 in the PLD chamber (Q_{PLD} - quench rate of the PLD chamber) before oxygen annealing in the tubular furnace. In subsection 6.2 we have shown that the highest self-field and in-field J_c are achieved at T_{ann}=450 °C. In subsection 6.3, t_{ann}=15 min showed slightly better in-field performance than the other annealing times. However, since the difference compared to other t_{ann} can be neglected for t_{ann}=5-60 min, for studies of influence of Q_{PLD} on structural and transport properties the parameters T_{ann}=450 °C and t_{ann}=30 min were used (route 5, subsection 6.1).

6.4.1 Structural and superconducting properties

All GdBCO thin films were deposited at optimum conditions in accordance with the results in Chapter 4. After deposition, all samples were cooled to RT in 0.4 mbar oxygen flow. At the cooling stage, Q_{PLD} was varied between 5 °Cmin^{-1} and 30 °Cmin^{-1}. Afterwards, all GdBCO thin films were placed in the tubular furnace where they were annealed according to route 5 (see Subsection 6.1).

All samples have T_c≈92.8 K and *c*-axis lattice parameter ≈11.72 Å, which indicates that all samples have optimum oxygen content regardless of Q_{PLD}, Table 6.4.

Table 6.4: Basic superconducting and structural properties of GdBCO thin films cooled to RT with Q_{PLD}=5, 10, 15, and 30 °C/min.

Q_{PLD}, °Cmin^{-1}	5	10	15	30
T_c, K	92.7	92.8	92.8	92.8
c-axis, Å	11.720	11.724	11.722	11.720

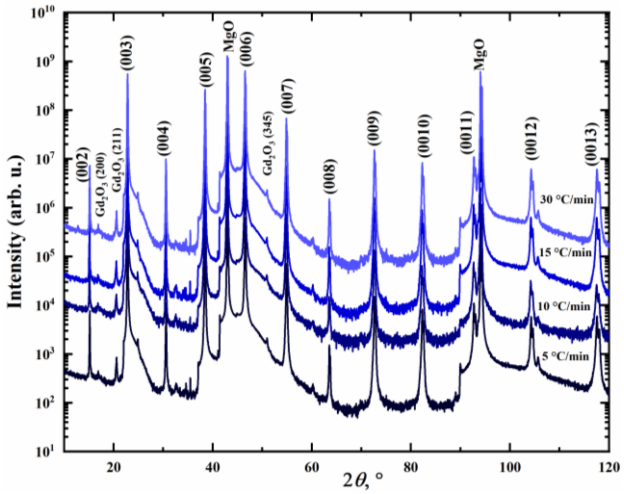

Figure 6.19: XRD θ-2θ scans of GdBCO thin films cooled to RT with Q_{PLD}=5, 10, 15 and 30 °C/min

All GdBCO thin films cooled down to RT at Q_{PLD}=5-30 °Cmin^{-1} (see Fig. 6.19) have GdBCO (00*l*) peaks which indicates of highly *c*-axis oriented thin films. Additionally, all patterns exhibit presence of Gd_2O_3 secondary phases with (200), (211) and (345) orientations. The size estimation gives increase from 15 to 23 nm with increase of Q_{PLD} for (200) orientation, ≈30 nm for (211) and decrease from 90 to 30 nm for (345) orientation.

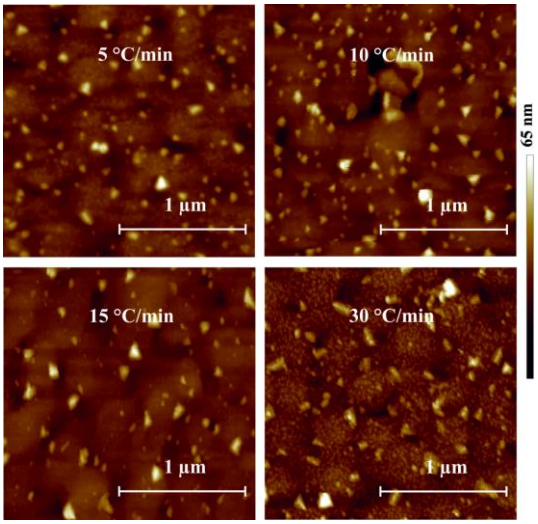

Figure 6.20: Surface images of GdBCO thin films cooled to RT at Q_{PLD}=5, 10, 15 and 30 °C/min

AFM images (see Fig. 6.20) for these GdBCO films show that, similar to other samples annealed at 450 °C for 30 min, all samples have hill-like surface morphology which appears due to island growth. Additionally, GdBCO thin films cooled at higher rates Q_{PLD}=10-30 °Cmin^{-1} exhibit triangular shaped precipitates, whose density varies from sample to sample. However, Q_{PLD}=5 °Cmin^{-1} has mostly round precipitates. Moreover, all precipitates have size between 30 and 50 nm, which corresponds to size estimation from XRD patterns for Gd_2O_3 NPs.

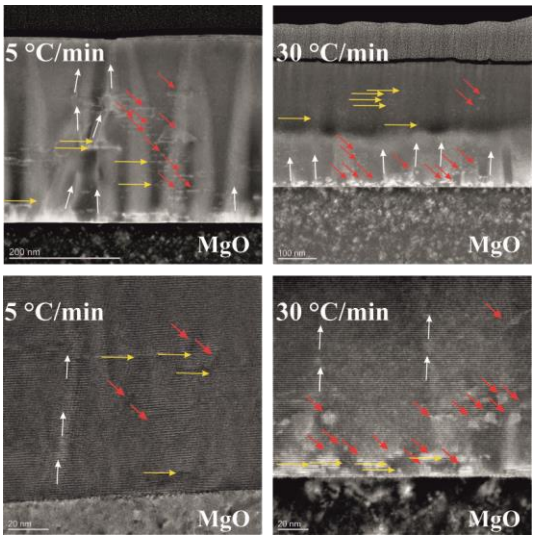

Figure 6.21: LADDF and HRTEM images of GdBCO thin films cooled to RT Q_{PLD}=5 and 30 °Cmin^{-1}. Yellow arrows indicate SFs, white-threading dislocations and anti-phase boundaries, red-Gd-rich NPs.

LAADF images for GdBCO thin films cooled to RT at Q_{PLD}=5 and 30 °Cmin^{-1} (see Fig. 6.21) clearly exhibit the variations in shade from domain formed by ED. Additionally, images show that both samples have Gd-rich NPs, which in accordance with XRD patterns are most probably Gd_2O_3 NPs, anti-phase boundaries and SF. Compared to low Q_{PLD}, Q_{PLD}=30 °Cmin^{-1} sample has a larger density of NPs close to the interface between GdBCO and MgO. Additionally, a higher cooling rate leads to a larger density of linear defects and SF, which is possibly caused by the diffusion processes. At Q_{PLD}=5 °Cmin^{-1}, the sample has a longer exposure to high T_{sub} and pO_2=0.4 mbar, which according to [146] leads to the reduction of the SF density. Moreover, the largest size for the Gd_2O_3 (345) reflection may indicate that the decomposition of SFs participates in the formation of Gd-rich NPs. Another feature, which appears during cool-down to RT, is the T-O phase transition being responsible for the twin boundary formation, which has at Q_{PLD}=5

°Cmin^{-1} the slowest rate. Therefore, it is possible that compared to low Q_{PLD}, at Q_{PLD}=30 °Cmin^{-1} the sample has a richer defect morphology due to the shorter exposure to high T_{sub} and faster T-O transition.

6.4.2 Transport properties

The field dependence of J_c at 77 K (see Fig. 6.22) for GdBCO thin films cooled to RT at Q_{PLD}=5-30 °Cmin^{-1} are very similar. Compared to low Q_{PLD}, Q_{PLD}=30 °Cmin^{-1} leads to a slightly higher in-field J_c. $F_{p,max}$(77 K) is increasing from 3.9 GNm^{-3} at Q_{PLD}=5 °Cmin^{-1} to 6.2 GNm^{-3} at Q_{PLD}=30 °Cmin^{-1}. At 10 K the difference in the in-field performance of GdBCO thin films becomes much clearer. Since GdBCO thin film with Q_{PLD}=30 °Cmin^{-1} has a richer defect morphology, it exhibits higher in-field J_c.

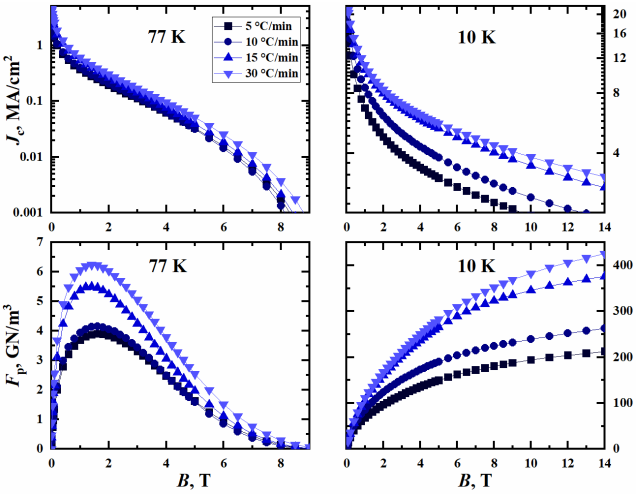

Figure 6.22: Field dependence of J_c for GdBCO thin films cooled to RT at Q_{PLD}=5, 10, 15 and 30 °Cmin^{-1}

$J_c(\theta)$ characteristics (see Fig. 6.23) of these GdBCO thin films are similar to GdBCO thin films from subsections 6.2 and 6.3 annealed at T_{ann} =450 °C and t_{ann}=30 min. J_c anisotropy at 1 T, 77 and 65 K exhibits a large peak in *c*-axis direction, which appears due to flux pinning at dislocations as well as contributions from dislocation loops around SF. Shoulders in the region 235°-270°, and a small peak in the *ab*-direction (becomes more visible at 1 T, 65 K). As seen from Fig. 6.23, the peak in *ab*-direction is increasing from Q_{PLD}=5 °Cmin^{-1} to Q_{PLD}=30 °Cmin^{-1}, which confirms the hypothesis for Fig. 6.20: at low Q_{PLD}, Gd124 phase (i.e., SF) due to longer exposure to high T_{sub} dissolves to contribute to formation of large Gd_2O_3 NPs and Gd123 phase. The latter is additionally responsible for

overall shift in J_c values in *c*-axis direction, since sufficiently short SF and Gd_2O_3 NPs are the main cause of such changes.

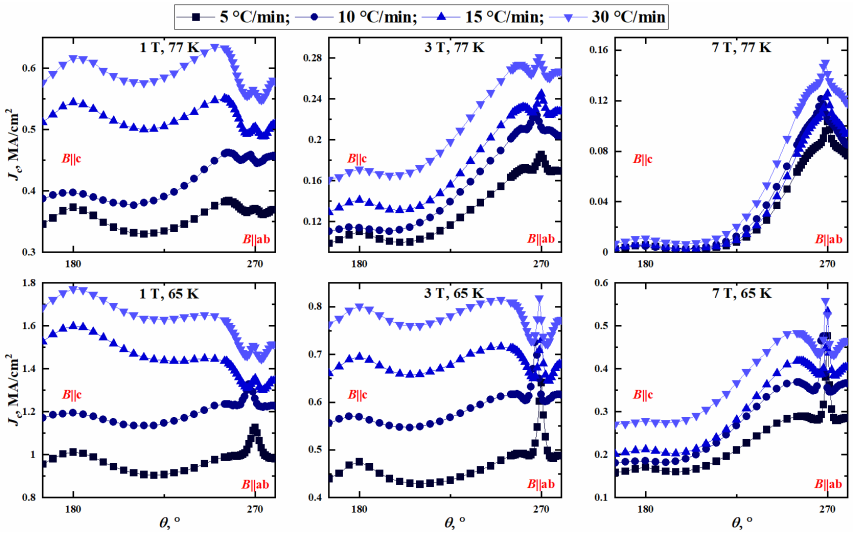

Figure 6.23: $J_c(\theta)$ characteristics for GdBCO thin films cooled to RT at Q_{PLD}=5, 10, 15 and 30 °Cmin^{-1}

Studies of the influence of Q_{PLD} on structural and transport properties in pristine GdBCO thin films show that combined with T_{ann} and t_{ann}, it is one of the various annealing parameters that have a strong influence on the defect morphology and, thus, the transport properties. Such variety of parameters can serve as a valuable tool for tailoring a desired pinning morphology.

General conclusion on *in-situ* and *ex-situ* oxygen annealing of pristine GdBCO thin films:

The study of the influence of oxygen annealing parameters such as T_{ann}, t_{ann}, PO_2 and Q_{PLD} allowed us to get a clearer understanding of changes appearing in the defect morphology and the resulting transport properties. Even though slightly different sets of parameters have been used for each oxygen annealing method, in the end, all pieces of the puzzle combine into a single picture. Based on our observations from XRD, TEM, and transport measurements, especially the J_c anisotropy, it became clear that in accordance with previous studies [74-77], 1D linear defects such as threading/edge dislocations play an utmost important role for flux pinning and enhancement of J_c at high temperatures and low magnetic fields. Dislocations, which originate from LAB, form domain walls and can pin vortices along their entire length. However, $J_c(\theta)$ characteristics and

TEM images lead to the conclusion that dislocations are formed during the deposition and are not or only slightly affected by the oxygen annealing process. As shown in Chapters 5 and 6, the oxygen annealing treatment primarily changes the SF and Gd_2O_3 NPs. Therefore, we propose a phase diagram, which correlates the annealing parameters and changes in density of SF and Gd_2O_3 NPs (see Fig. 6.24).

In pristine GdBCO thin films, T_{ann} and PO_2 are mainly modifying the density and size of SF and Gd-rich NPs. Therefore, regarding these parameters, we propose two scenarios:

1. Cooling from 800 °C to 450 °C at high PO_2
2. Cooling from 800 °C to 450 °C at low PO_2

Following the 1st scenario, SFs that are formed during deposition of GdBCO thin film start to decompose at high temperatures, which leads to the formation of short segmented SF combined with Gd-rich NPs. Then, increase in PO_2 up to 1 bar during oxygen annealing leads to a partial decomposition or dissolution of Gd-rich NPs. Therefore, the GdBCO thin film has a large density of fine Gd-rich NPs combined with a large density of short SFs, thus, resulting in the best in-field performance.

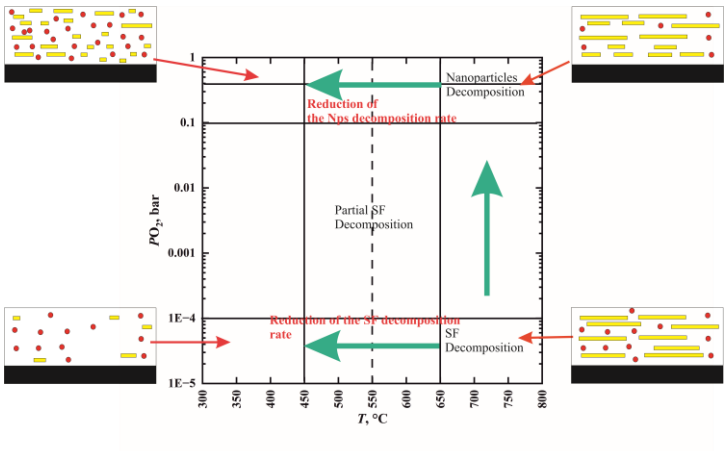

Figure 6.24: Phase Diagram for pristine GdBCO thin films, showing correlation of annealing parameters and changes in the density of SF and Gd_2O_3 NPs.

2nd scenario: during short cooling from 800 °C to T_{ann}=650 °C-780 °C, only a small amount of SFs is decomposing. Afterwards, increase of PO_2 leads to the stabilization of SFs and to the beginning of the dissolution/decomposition of Gd-rich NPs. Therefore, GdBCO thin films that are oxygenated according to scenario 2 have mostly SFs in their matrix with much less Gd-rich NPs. Both *in-situ* and *ex-situ* oxygen annealing have

similar changes during variation of T_{ann} and PO_2. However, one of the most interesting features, which appeared during investigation of t_{ann} and which requires more thorough studies are the strain effects which defects and secondary phases cause during *in-situ* annealing. This leads to the question: What changes appear during heating and cooling steps that lead to such behavior. This should be the focus of future studies.

7 *Ex-situ* oxygen annealing of 2.5 wt.% $BaHfO_3$ nanocomposite $GdBa_2Cu_3O_{7-\delta}$ superconducting thin films

In the field of nanocomposite *RE*BCO-based superconducting thin films, the majority of studies are focused on understanding the correlation between deposition conditions, such T_{sub}, v_{dep}, oxygen pressure during deposition, and resulting defect morphology and, thus, resulting in-field J_c and its anisotropy. Similar to the situation with pristine films, often the oxygen annealing issue stays most of the time disregarded. Therefore, in this chapter we attempt to uncover the influence of T_{ann} on structural and transport properties in $BaHfO_3$ nanocomposite GdBCO thin films.

7.1 Structural and superconducting properties

Based on the results of Chapters 5 and 6, i.e., the better performance of *ex-situ* oxygen annealed pristine GdBCO thin films, only *ex-situ* annealing was studied for BHO nanocomposite GdBCO thin films. All 2.5 wt.% BHO nanocomposite GdBCO thin films were deposited in accordance with the optimum conditions of Chapter 4. After deposition, all BHO nanocomposite samples were cooled to RT at 0.4 mbar oxygen flow with Q_{PLD}=30 °Cmin^{-1}. Afterwards, films were placed in the tubular furnace where they were heated to 800 °C in Ar flow. After reaching 800 °C, the Ar flow was exchanged by a mixture of Ar+400 ppm O_2 in which the samples were cooled to the respective T_{ann}. Similar to pristine GdBCO, t_{ann} was varied between 10 and 30 min. All samples were annealed at a pressure of 1 bar and 2000 ml/min pure O_2 flow, which was also kept during cool-down to RT.

Compared to *ex-situ* annealed pristine GdBCO thin films, BHO nanocomposite samples have lower transition temperatures T_c≈90.5 K, Table 7.1. As mentioned in Chapter 4, such a reduction of transition temperatures is a common effect of introduction of secondary phases, since they create oxygen deficient regions around the nanocolumns [93, 140]. The *c*-axis lattice parameters (≈11.76 Å) are slightly larger compared to pristine GdBCO thin films, which is due to the difference in the lattice parameters between GdBCO and BHO and extension of the *c*-axis lattice parameter by BHO.

Table 7.1: Basic superconducting and structural properties of 2.5wt.% BHO nanocomposite GdBCO thin films annealed at T_{ann}=450 °C-780 °C.

T_{ann}, °C	450	550	650	700	780
T_c, K	90.2	90.1	90.4	90.5	90.7
c-axis, Å	11.764	11.764	11.761	11.757	11.763

Fig. 7.1 shows (00*l*) reflections of GdBCO for all films. The samples with T_{ann}=450 °C and 550 °C show a weak GdBCO (103) reflection. Additionally, similar to *ex-situ* annealed pristine films, (200), (211) and (345) reflections of Gd_2O_3 are present as well. Since the Gd_2O_3 (200) reflection has not been observed for the *in-situ* annealed BHO nanocomposite GdBCO thin films deposited on $LaAlO_3$ single crystals, this possibly indicates that similar to pristine samples, heating to 800 °C in Ar flow decomposes the matrix of BHO nanocomposite GdBCO thin films. However, in case of BHO nanocomposite samples the formation of phases other than Gd_2O_3 is also possible. Further investigation on the thermodynamic phase stability diagram for BHO-nanocomposite GdBCO thin films is required.

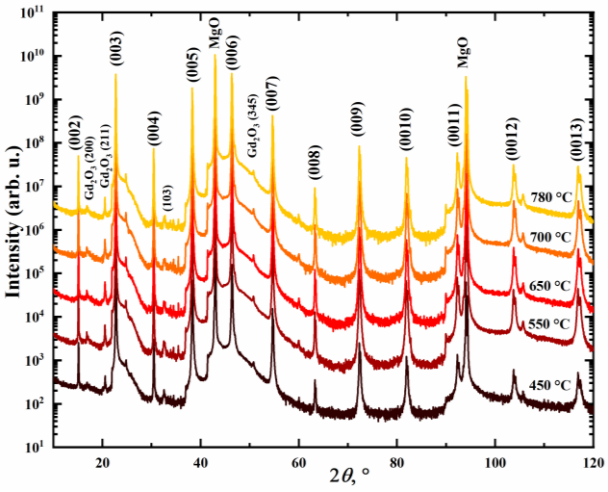

Figure 7.1: XRD pattern of 2.5wt% BHO nanocomposite GdBCO thin films annealed at T_{ann}=450 °C-780 °C.

AFM images (see Fig. 7.2) show similar surface morphologies to *ex-situ* annealed pristine GdBCO thin films with a clear hill-like surface which occurs as a results of island-type film growth. Additionally, triangular shaped precipitates with size 30-50 nm, which are possibly Gd_2O_3, are present. Visible at lower magnification (lower row in Fig. 7.2),

the BHO-nanocomposite GdBCO thin films have “splash-like” precipitates of size 3-4 μm, which have not been observed for the samples of Chapter 4 nor in previous studies. Due to the lack of information on the oxygen annealing of *RE*BCO-based superconducting thin films containing BMO nanocomposites, the identification of the composition requires further Z-contrast measurements at TEM. However, similarly to the behavior of pristine GdBCO placed in the tubular furnace, due to heating to 800 °C, the Gd123 phase is decomposing into Gd163+Gd_2O_3+liquid phases, and therefore, in case of BHO nanocomposite GdBCO, possibly new compounds containing atoms of BHO and GdBCO can be formed during heating to 800 °C. Consecutive cooling in the mixture of Ar+400 ppm O_2 is possibly “freezing” those new compounds both in the GdBCO matrix and on the surface.

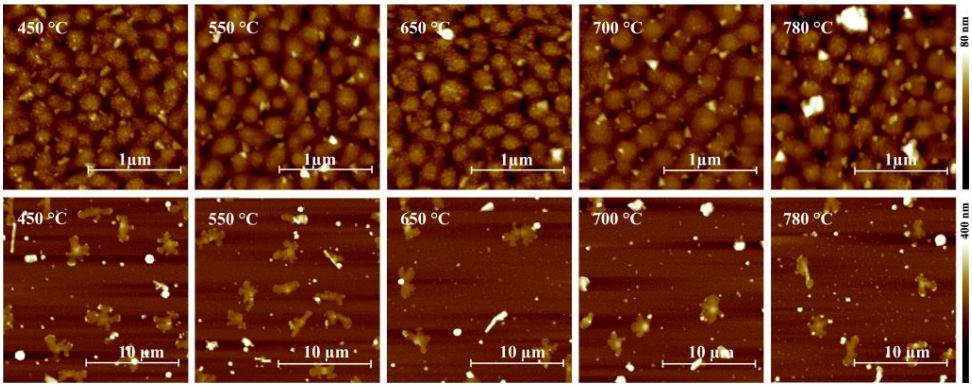

Figure 7.2: Surface images of 2.5wt.% BHO nanocomposite GdBCO thin films annealed at T_{ann}=450 °C-780 °C.

7.1.1 Transport properties

The biggest shift of the ILs for GdBCO films containing 2.5wt.% BHO towards high-field region exhibits T_{ann}=700 °C, while the lowest are at T_{ann}=450 °C and 550 °C. The ILs of the nanocomposites have a sharp increase in the region 0-1 T with a transition towards linear dependence, while samples of Chapter 4 exhibit a clear S-shape of the IL. Thus, as mentioned in the previous section, it is possible that BHO is present in GdBCO matrix in the shape of short segmented nanorods or NPs. Such changes compared to samples of Chapter 4 is most likely a result of additional heating and cooling steps and disruption of BHO-nanocolumns by the formation of Gd_2O_3, SFs and other defects.

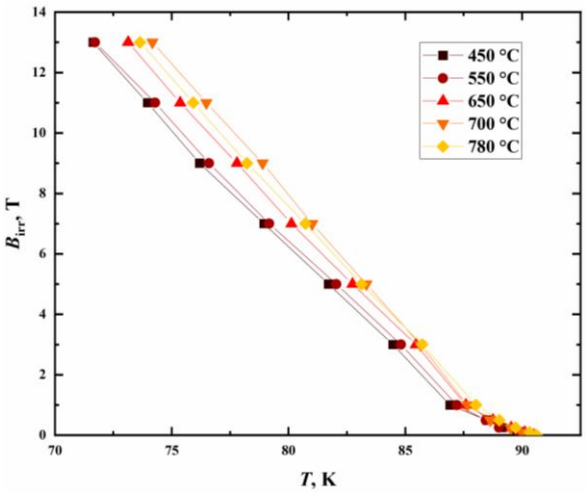

Figure 7.3: ILs of 2.5wt.% BHO nanocomposite GdBCO thin films annealed at T_{ann}=450 °C-780 °C.

The samples annealed at T_{ann}=450 °C and 550 °C have the strongest field dependence at 77 K, Fig. 7.4, while the highest in-field J_c is shown by the sample annealed at T_{ann}=700 °C. In contrast to the extraordinary behavior of *ex-situ* annealed pristine GdBCO thin films, in-field J_c values of BHO nanocomposite samples are increasing from T_{ann}=450 °C, reaching maximum values at T_{ann}=700 °C. Further increase of T_{ann} decreases in-field J_c. Compared to the *in-situ* annealed BHO nanocomposite GdBCO thin films of Chapter 4, the field dependence of J_c for *ex-situ* annealed samples does not exhibit such a clear plateau like dependence, which in Chapter 4 appears at 77 K as a result of the matching effect.

F_p at 77 K is larger compared to pristine GdBCO thin films, with $F_{p,max}$(77 K)=8.6 GNm^{-3} reached at T_{ann}=700 °C. Additionally, the peak in $F_p(B)$ for *ex-situ* annealed samples is shifted towards higher fields ($F_{p,max}$ is achieved at 2.4 T). Compared to *in-situ* annealed BHO containing GdBCO thin films of Chapter 4, the *ex-situ* annealed films show lower values of $F_{p,max}$. Such differences in J_c and F_p possibly appear due to the different shape of BHO in the GdBCO matrix. While *in-situ* annealed samples contain BHO mostly in the shape of nanorods and some as NPs, it is possible that *ex-situ* annealed samples have BHO predominantly in the shape of NPs or segmented nanorods. This additionally corresponds to the near absence of the S-shape of the IL in Fig. 7.3.

At 10 K, the trend in field dependence of J_c is different from 77 K. T_{ann}=700 °C shows here the highest in-field values in the region 6-14 T. In the low field region between 0-6 T, however, T_{ann}=780 °C shows a better performance compared to all other T_{ann}. For further explanation of the field dependence of J_c, detailed BF-STEM images of those

samples are required to identify which defects are present in the GdBCO matrix, which was not possible in this work. However, as mentioned above strong pinning centers give larger contribution towards flux pinning at 77 K, while the contribution of weak pinning centers increases towards low temperatures. Therefore, slight variations in the defect density most likely cause the behavior at 10 K.

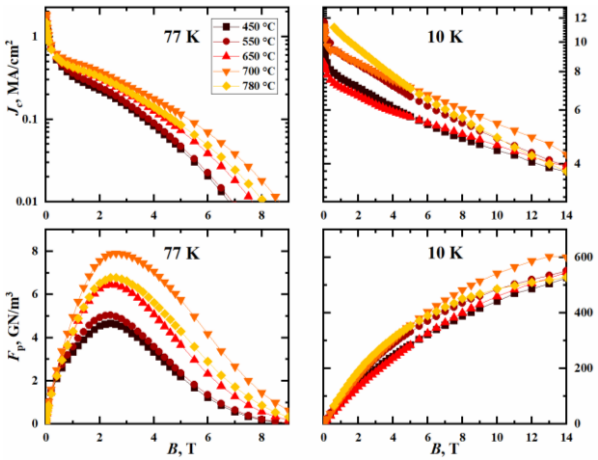

Figure 7.4: ILs of 2.5wt.% BHO nanocomposite GdBCO thin films annealed at T_{ann}=450 °C-780 °C.

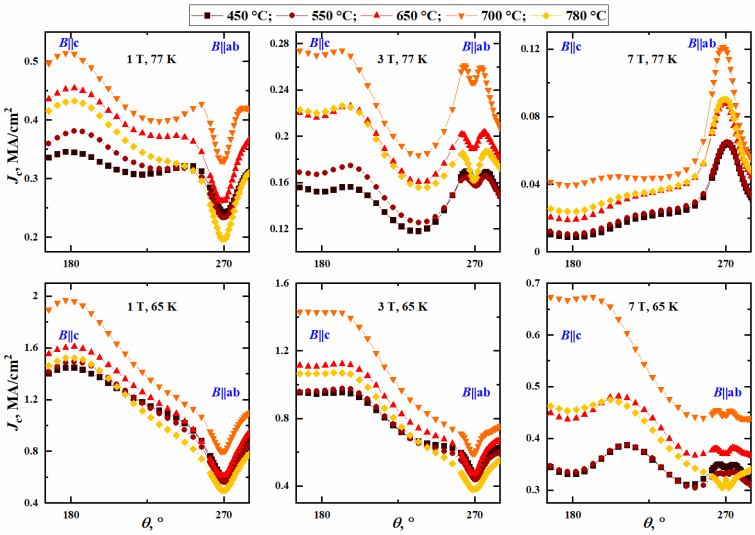

Figure 7.5: $J_c(\theta)$ characteristic of 2.5wt.% BHO nanocomposite GdBCO thin films annealed at T_{ann}=450 °C-780 °C.

$J_c(\theta)$ characteristics (see Fig. 7.5) for 2.5 wt.% BHO nanocomposite GdBCO thin films at 1 T, 77 and 65 K, show a large peak in *c*-axis direction, a dip in the *ab*-direction, and a shoulder between 235°-270°. At 3 T, 77 K and 65 K, the peak in *c*-axis direction is broader, similar to results of Chapter 4, which is the result of segmented nanorods and stretch of the vortices among neighbouring nanorods/NPs. At 7 T, 77 K, a peak in the *ab*-direction appears, however, it is much broader compared to pristine GdBCO thin films.

Ex-situ oxygen annealing of 2.5 wt.% BHO nanocomposite GdBCO thin films shows that the variation of T_{ann} can be an effective tool to further modify the defect morphology and improve in-field performance both at LN_2 and LHe temperatures. Compared to *ex-situ* annealed pristine GdBCO thin films, BHO containing GdBCO samples require higher T_{ann} for best performance, which is possibly caused by a higher complexity of the system and different phase formation.

8 Conclusions and future work

8.1 Conclusions

Regardless of being known for over 30 years, *RE*BCO-based superconductors still have a large variety of features which need to be thoroughly investigated in order to achieve in a reproducible manner the highest possible J_c and to have a possibility of tailoring the J_c anisotropy, thus, utilize its full application potential. Oxygen annealing, which is involved in every HTS film deposition method, is an important if not crucial step in obtaining superconducting thin films with high T_c and J_c. Even though various aspects related to this issue, such as oxygen in- and out-diffusion, oxygen exchange kinetics, dependence of superconducting properties on the oxygen content, have been studied, in the current work we have shown that oxygen annealing can be used as an additional tool for tailoring the pinning landscape morphology and further improvement of transport properties of pristine and 2.5wt% BHO-nanocomposite GdBCO thin films.

As the first step in achieving our goal, the optimum deposition conditions for pristine and 2.5wt% BHO-nanocomposite GdBCO thin films were determined. T_{sub}=800 °C, f=10 Hz, pO_2=0.4 mbar has been shown to be the optimum. Films grown at these conditions have T_c≈92 K, and J_c(0 T, 77 K)=3 MA/cm^2. BF-STEM images revealed domain walls formed by ED, SFs and Gd-rich nanoparticles. The J_c anisotropy was similar to previous reports on GdBCO thin films with a peak in *ab*-direction and a large peak in *c*-axis direction. In case of nanocomposite films, just as for pristine films, T_{sub}=800 °C has shown the highest in-field J_c. Variation of laser frequency from 10 to 5 Hz increases in-field J_c at 77 and 65 K, but showed worse performance at 10 and 30 K. Further reduction of f to 2 Hz leads to a decrease of in-field J_c at all temperatures. Such changes appear due to increased size of the BHO nanocolumns, which cause a disruption of the GdBCO matrix and, therefore, a degradation of transport properties. Therefore, f=10 Hz is also the optimum frequency for growth of BHO-nanocomposite GdBCO thin films. These 2.5 wt% BHO-nanocomposite GdBCO thin films have BHO nanocolumns of diameter 4-5 nm, as well as segmented parts, nanoparticles, and SFs. Such microstructures lead to $F_{p,max}$(77 K)=6.6 GNm^{-3}, which is comparable to or even higher than previous reports on GdBCO thin films containing BMO secondary phases. $J_c(\theta)$ dependencies have a peak in *ab*-direction and a large peak in *c*-axis direction. Additionally, at 1 T, 77 and 65 K, there is a shoulder between 225° and 270°, which appears due to synergetic flux pinning on planar and spherical defects. Another important feature that appears due to the interplay of nanocolumns and segmented nanorods is a dip in J_c around the *c*-axis peak. Comparison of in-

field J_c for pristine and BHO-nanocomposite samples has shown that incorporation of BHO as APC is an effective method in improving transport properties.

As 2nd step in our journey of determining the influence of oxygen annealing on transport properties, we have chosen T_{ann} and t_{ann} as main parameters of our study for *in-situ* and *ex-situ* oxygen annealing. In addition, for *in-situ* annealing we have studied the influence of oxygen pressure during annealing PO_2, and for *ex-situ* annealing the *in-situ* quench rate (Q_{PLD}). One of the main observations in the current work was that in GdBCO thin films mainly the size and the density of SFs and Gd-rich NPs is modified by the oxygen annealing procedure, hence, enhancing the low temperature-high magnetic field transport properties, while at high temperatures ED are the dominant type of defects for flux pinning. The main parameters responsible for those changes are T_{ann} and PO_2. Therefore, based on the results of XRD, TEM, and J_c anisotropy measurements we propose two paths on how the defect morphology of GdBCO thin films can be tailored:

1. **High to low temperature cooling at low pressures, followed by low temperature high pressure annealing and consecutive cooling to RT:** According to this scenario, SFs, which are formed during deposition of GdBCO thin film, start to decompose at high temperatures, which leads to the formation of short segmented SFs combined with Gd-rich NPs. The following increase in PO_2 up to 1 bar during oxygen annealing leads to the partial decomposition or dissolution of Gd-rich NPs. Therefore, the resulting GdBCO thin films have a large density of small Gd-rich NPs combined with a large density of short SFs.
2. **Low to high pressure annealing at high temperatures with consecutive cooling to RT:** Following this path, short cooling from 800 °C to T_{ann}=650 °C-780 °C leads to the decomposition of only a small amount of SF. Afterwards, increase of PO_2 leads to the stabilization of SF and beginning of the dissolution/decomposition of Gd-rich NPs. Therefore, GdBCO thin films oxygenated according to this scenario have mostly SFs in their matrix with much smaller densities of Gd-rich NPs.

Since *ex-situ* oxygen annealing has been shown to be advantageous for pristine GdBCO thin films, we also studied *ex-situ* oxygen annealing of 2.5wt% BHO nanocomposite GdBCO thin films, which we limited to the variation of T_{ann} because that had the largest effect on the defect morphology. Compared to pristine GdBCO thin films, BHO nanocomposite samples required a larger annealing temperature of 700 °C for the best performance. Due to lack of studies on the phase stabilities for such compounds, this has been attributed to the overall complexity of the system and formation of the new phases different from those in pristine GdBCO thin films.

In order to achieve our goals, it was required to overcome a variety of challenges, which go along with the oxygen annealing studies. For example, determination of the oxygen content, especially in thin films, requires specific measurements, which were not possible in our research institute. One of the solutions is determination of the *c*-axis lattice parameter from XRD θ-2θ scans since it is related to the oxygen content of the film. However, as shown in Chapters 4 and 5, many factors such as composition variation, strain, and oxygen inhomogeneities can affect the final result. Other challenges were related to the studies of the film microstructure. To fully understand the changes that each oxygen annealing parameter creates, it is necessary to make BF-STEM measurements on a large number of samples. Therefore, due to limited options in this project, only few samples from each batch were selected. Nevertheless, in the current work, we have shown that among a large variety of parameters in pulsed laser deposition of *RE*BCO-based superconducting thin films, oxygen annealing with all possible parameters also must be taken into account. Two approaches which we considered, *in-situ* and *ex-situ* oxygen annealing, have been shown to be effective not only in modifying the defect morphology, but also in greatly improving the transport properties of pristine and 2.5wt% BHO nanocomposite GdBCO thin films. Comparison of changes that appeared when the system got more complex (GdBCO+2.5wt% BHO) is a good example of the importance of oxygen annealing and necessity of consideration of this issue for each system.

8.2 Future work

Even though large amount of work has been done in this study, certain aspects should still be addressed in order to gain a complete understanding of the influence of oxygen annealing on microstructure and pinning properties:

1. TEM analysis of a large number of deposited pristine and 2.5wt.% $BaHfO_3$ nanocomposite GdBCO thin films, in order to understand the features near 550 °C in pristine GdBCO films and reconstruction of the phase diagrams for GdBCO thin films containing BMO nanocomposites.
2. Influence of oxygen pressure during *ex-situ* annealing: sample annealed at PO_2=0.4 bar has shown the highest in-field J_c for the *in-situ* annealed GdBCO thin films, therefore, similar study is required for the *ex-situ* annealing.
3. Heating step in Ar atmosphere during *ex-situ* oxygen annealing: how far can we destroy the Gd123 phase? How will defect morphology change in that case?
4. Applicability for industry and coated conductors production: additional heating and cooling steps can possibly lead to the formation of various secondary phases on the *RE*BCO-buffer layer interface during coated conductors production. Therefore, such heat treatments need to be thoroughly investigated.

Bibliography

[1] Kammerligh-Onnes, H. The resistance of pure mercury at helium temperatures. *Communications Leiden*. Pages 1479-1481. 1911.

[2] Meissner, W and Ochsenfeld, B. Ein neuer Effect bei Eintritt der Supraleitfähigkeit. *Die Naturwissenschaften*. 44. 1933.

[3] Bardeen, J., Cooper, L. N., and Schrieffer, J. R. Microscopic Theory of Superconductivity. *Physical Review*. 106. Pages 162-164. 1957.

[4] Berdnorz, J. G. and Müller, K. A. Possible High T_c Superconductivity in the Ba-La-Cu-O system. *Zeitschrift für Physik B-Condensed matter*. 64. Pages 189-193. 1986.

[5] Chu, C. W. Superconductivity above 90 K. *Proceedings of the National Academy of Sciences of Unites States of America*. 84. Pages 4681-4682. 1987.

[6] Maeda, H., Tanaka, Y., Fukutomi, M. and Asano., T. A New High-T_c Oxide Superconductor without a Rare Earth Element. *Japanese Journal of Applied Physics*. 27 (2). Pages L209-L210. 1988.

[7] Cheng, Z. Z. and Hermann, A. M. Bulk superconductivity at 120 K in Tl-Ca/Ba-Cu-O system. *Nature*. 332. Pages 138-139. 1988.

[8] Chu, C. W., Gao, L., Chen, F., Huang, Z. J., Meng, R. L., and Xue, Y. Y. Superconductivity above 150 K In $HgBa_2Ca_2Cu_3O_{8+\delta}$ at high pressures. *Nature*. 365. Pages 323-325. 1993.

[9] Gao, L., Xue, Y. Y., Chen, F., Xiong, Q., Meng, R. L., Ramirez, D. and Chu, C. W. Superconductivity up to 164 K in $HgBa_2Ca_{m-1}Cu_mO_{2m+2+\delta}$ (m=1, 2 and 3) under quasihydrostatic pressures. *Physical Review B*. 50 (6). Pages 4260-4263. 1994.

[10] Nagamatsu, J., Nakagawa, N., Muranaka, T., Zenitani, Y., and Akimitsu, Z. Superconductuvity at 39 K in magnesium diboride. *Nature*. 410. Pages 63-64. 2011.

[11] Snider, E., Dasenbrock-Gammon, N., McBride, R., Debessai, M., Vindana, H., Vencatasamy, K., Lawler, K. V., Salamat, A., and Dias, R. P. Room-temperature superconductivity in a carbonaceous sulfur hydride. *Nature*. 586. Pages 373-377. 2020.

[12] MacManus-Driscoll, J. L., Foltyn, S. R., Jia, Q. X., Wang, H., Serquis, A., Civale L., Maiorov, B., Hawley, M. E., Mawley M. P., and Peterson, D. E. Strongly enhanced current densities in superconducting coated conductors of $YBa_2Cu_3O_{7-x}$+$BaZrO_3$. *Nature materials*. 3. Pages 439-443. 2004.

[13] Yamada, Y., Takahashi, K., Kobayashi, H., Konishi, M., Watanabe, T., Ibi, A., Muroga, T., Miyata, S., Kato, T., Hirayama, T., and Shiohara, Y. Epitaxial nanostructure and defects effective for pinning in $Y(RE)Ba_2Cu_3O_{7-x}$ coated conductors. *Applied Physics Letters*. 87. Pages 132502. 2005.

[14] Goyal, A., Kang, S., Leonard, K. J., Martin, P. M., Gapud, A. A., Varela, M., Paranthaman, M., Ijaduola, A. O., Specht, E. D., Thompson, J. R., Christen, D. K., Pennycook, S. J., and List, F. A. Irradioation-free, columnar defects comprising of self-assembled nanodots and nanorods resulting in strongly enhanced flux-pinning in $YBa_2Cu_3O_{7-x}$ films. *Superconductor Science and Technology*. 18. Pages 1533-1538. 2005.

[15] Maiorov, B., Baily, S. A., Zhou, H., Ugurlu, O., Kennison, J. A., Dowden, P. C., Holesinger, T. J., Foltyn, S. R., and Civale, L. Synergetic combination of different types of defects to optimize pinning landscape using $BaZrO_3$-doped $YBa_2Cu_3O_7$. *Nature materials*. 8. Pages 398-404. 2009.

[16] Tullel, H. L., and Opilla, E. Defects and oxygen diffusion in high-T_c superconductors. *Solid State Ionics*. 40/41. Pages 790-794. 1990.

[17] LaGraff, J. R. and Payne, D. A. Concentration-dependent oxygen diffusivity in $YBa_2Cu_3O_{6+x}$. II. Oxygen partial pressure studies. *Physica C*. 212. Pages 478-486. 1993.

[18] Tsuda, K., Suzuki, T., Matsui, T., Kimura, H., Nagano, M. and Mukae, K. Observation of oxygen in YBCO thin films during the cooling down process using ^{18}O tracer. *Phase Transitions*. 41. Pages 159-163.1993.

[19] Michaelis, A., Irene, E., Auciello, O. and Krauss, A. A study of oxygen diffusion in and out of $YBa_2Cu_3O_{7-\delta}$ thin films. *Journal of Applied Physics*. 83 (12). Pages 7736-7743. 1998.

[20] Bredikhin, S. I., Emel`chenko, G. A., Shechtman, V. Sh., and Zhokov, A. A., Carter, S., Chater, R. J., and Kilner, J. A. Anisotropy of oxygen self-diffusion in $YBa_2Cu_3O_{7-\delta}$ single crystals. *Physica C*. 179. Pages 286-290. 1991.

[21] Span, E. A. F., Wormeester, H., Blank, D. H. A., Rogalla, H. Oxygen diffusion in laser-ablated $YBa_2Cu_3O_x$ thin films studied by spectroscopic ellipsometry. *Materials Science and Engineering*. B56. Pages 123-129. 1998.

[22] Vazquez-Navarro, M. D., Kursumovic, A., Evetts, A. Study and modelling of oxygen diffusion in $YBa_2Cu_3O_{7-\delta}$ under isothermal conditions. *Superconductor Science and Technology*. 12. Pages 1177-1122. 1999.

[23] Tsukui, S., Adachi, M., Oshima, R., Nakajima, H., Toujou, F., Tsukamoto, K., Tabata, T. Oxygen tracer diffusion in $YBa_2Cu_3O_y$ superconductor. *Physica C*. 351. Pages 357-362. 2001.

[24] Mori, Z., Doi, T., and Hakuraku, Y. Oxygen diffusion in c-axis oriented $Y_1Ba_2Cu_3O_{7-\delta}$ thin films *Journal of Applied Physics*. 110. 033915. 2011.

[25] Cava, R. J., Batlogg, B., Chen, C. H., Rietman, E. A., Zahurak, S. M., and Werder, D. Oxygen stoichiometry, superconductivity and normal-state properties of $YBa_2Cu_3O_{7-\delta}$. *Nature*. 329. Pages 423-425. 1987.

[26] Routbort, J. L., and Rothman, S. J. Oxygen diffusion in cuprate superconductors. *Journal of Applied Physics*. 76. Pages 5615-5628. 1994.

[27] Lindemer, T. B., Hunley, J. F., Gates, J. E., Sutton, A. L., Brynestad, J., and Hubbard, C. R., Patrick, K. Experimental and Thermodynamic study of non-sthoichiometry in $YBa_2Cu_3O_{7-x}$. *Journal of American Ceramics Society*. 72 (10). Pages 1775-1788. 1989

[28] Shiohara, Y., Endo, A. Crystal growth of bulk high-T_c superconducting oxide materials. *Materials Science and Engineering*. R19. Pages 1-86. 1997

[29] Lee, J.-W., Choi, S.-M., Song, J.-H., Lee, J.-H., Moon, S.-H., Yoo, S.-I. Stability phase diagram of $GdBa_2Cu_3O_{7-\delta}$ in low oxygen pressures. *Journal of Alloys and Compounds*. 602. Pages 78-86. 2014

[30] Lee, J. -W., Choi, S.-M., Oh, W.-J., Lee, J.-H., Moon, S.-H., and Yoo, S.-I. Enhanced Pinning Properties of $GdBa_2Cu_3O_{7-\delta}$ Coated Conductors via a Post-Annealing Process. *IEEE Transaction on Applied Superconductivity*. 26 (3). Pages 8001906. 2016

[31] Wu, M. K., Ashburn, J. R., Torng, C. J., Hoi., P. H., Meng., R. L., Gao, L., Huang, Z. J., Wang, Y. Q., and Chu, C. W. Superconductivity at 93 K in a New Mixed-Phase Y-Ba-Cu-O Compound at Ambient Pressure. *Physical Review Letters*. 58 (9), Pages 908-910. 1987.

[32] Asano, H., Takita, K., Katoh, H., Akinagi, H. Crystal structure of high T_c $LnBa_2Cu_3O_{7-\delta}$(Ln=Sm, Eu and Gd). *Japanese Journal of Applied Physics*. 26 (8). Pages L1410-L1412. 1987.

[33] Xu, Y., Guan, W., Ata-Allah, S. S., and Heiden, Ch. Rare Earth Size Effect on T_c and ρ_n in the Ga and Zr doped $RBa_2Cu_{3-x}Ga_xO_{7-y}$ and $RBa_2Cu_{3-x}Zn_xO_{7-y}$ Systems (R=Yb, Er, Y, Dy, Gd, Eu, Sm and Nd). *Physica C*. 235-240. Pages 823-824. 1994.

[34] Takahashi, K., Kobayashi, H., Yamada, Y., Ibi, A., Fukushima, H., Konishi, M., Miyata, S., Shiohara, Y., Kata, T., and Hirayama, T. Investigation of thick PLD-GdBCO and ZrO_2 doped GdBCO coated conductors with high critical current on PLD-CeO_2 caped IBAD-GZO substrate tapes. *Superconductor Science and Technology*. 19. Pages 924-929. 2006.

[35] Siergist, T., Sunshine, S., Murphy, D. W., Cava, R. J. and Zahurak, S. M. Crystal structure of the high-T_c superconductor $Ba_2YCu_3O_{9-\delta}$. *Physical Review B*. 35 (13). Pages 7137-7139. 1987.

[36] Calestani, G. and Rizzoli, C. Crystal structure of $YBa_2Cu_3O_7$ superconductor by single crystal X-ray diffraction. *Letters to Nature*. 348. Pages 606-607. 1987.

[37] Jorgensen, J. D., Beno, M. A., Hinks, D. G., Sonderholm, L., Volin, K. J., Hitterman, R. L., Grace, J. D. and Schuller, I. K. Oxygen orderding and the orthorombic-to-tetragonal phase transition in $YBa_2Cu_3O_{7-x}$. *Physical Review B*. 36 (7). Pages 3608-3616. 1987.

[38] Habermeier, H.-U. Science and technology of cuprate-based high temperature superconductor thin films, heterostructures and superlattices – the first 30 years. *Low Temperature Physics*. 42 (10). Pages 840-862. 2016.

[39] Hammond, R. H. and Bormann, R. Correlation between the in situ growth conditions of YBCO thin films and the thermodynamic stability criteria. *Physica C*. 162-164. Pages 703-704. 1989.

[40] Skakle, J. M. S. Crystal chemical substitutions and doping of $YBa_2Cu_3O_x$ and related superconductors. *Materials Science and Engineering*. R23. Pages 1-40. 1998.

[41] Jorgensen, J. D., Veal, B. W., Kwok, W. K., Crabtree, G. W., Umezawa, A., Nowicki, L. J. and Paulikas, A. P., Structural and superconducting properties of orthorombic and tetragonal $YBa_2Cu_3O_{7-x}$: The effect of oxygen stoichiometry and ordering on superconductivity. *Physical Review B*. 36 (10). Pages 5731-5734. 1987.

[42] Jorgensen, J. D. Structural Properties of High-T_c Oxide Superconductors. *Japanese Journal of Applied Physics*. 26. Pages 2017-2022. 1987.

[43] Jorgensen, J. D., Veal, B. W., Paulikas, A. P., Nowicki, L. J., Crabtree, G. W., Claus, M. and Kwok, W. K. Structural properties of oxygen-deficient $YBa_2Cu_3O_{7-\delta}$. *Physical Review B*. 41 (4). Pages 1863-1877. 1990.

[44] Schuller, I. K., Hinks, D. G., Beno, M. A., Capone, D. W., Soderholm, L., Locquet, J.-P., Bruynseraede, Y., Segre, C. U. and Zhang, K. Structural phase transitions in $YBa_2Cu_3O_{7-\delta}$: The Role of dimensionality for high temperature superconductivity. *Solid State Communications*. 63 (5). Pages 385-388. 1987.

[45] Nakazawa, Y., Ishikawa, M., Takabatake, T., Takeya, H., Shibuya, T., Terakura, K. and Takei, F. Characterization of High T_c Superconductor $(Ba_{0.7}Y_{0.3})CuO_{3-\delta}$. *Japanese Journal of Applied Physics*. 26 (5). Pages L682-L684. 1987.

[46] Nakazawa, Y., Ishikawa, M., Takabatake, T., Koga., K. and Terakura, K. Characterization of Metamorphic Phases of $Ba_2YCu_3O_{9-\delta}$. *Japanese Journal of Applied Physics*. 26 (5). Pages L796-L798. 1987.

[47] Specht, E. D., Sparks, C. J., Dhere, A. G., Brynestad, J., Cavin, O. B. and Kroeger, D. M., Oye, H. A. Effect of oxygen pressure on the orthorombic-tetragonal transition in the high temperature superconductor $YBa_2Cu_3O_x$. *Physical Review B*. 37 (13). Pages 7426-7434. 1988.

[48] Breit, V., Schweiss, P., Hauff, R., Wühl, H., Claus, H., Rietschel, H., Erb, A. and Müller-Vogt, G. Evidence for chain superconductivity in near-stoichiometric $YBa_2Cu_3O_x$ single crystal. *Physical Review B*. 52 (22). Pages R15727-R15730. 1995.

[49] Beyers, R., Ahn, B. T., Gorman, G., Lee, V. Y., Parkin, S. S., Ramirez, M. L., Roche, K. P., Vazquez, J. E., Gür, T. M. and Huggins, R. A. Oxygen ordering, phase separation and the 60-K and 90-K plateaus in $YBa_2Cu_3O_x$. *Letters to Nature*. 340. Pages 619-621. 1989.

[50] Namgung, C., Irvine, J. T. S. and West, A. R. Absence of critical temperature plateaux in quenched samples of $YBa_2Cu_3O_x$. *Physica C*. 168. Pages 346-350. 1990.

[51] Ye, J. and Nakamura, K. Quantitative structure analysis of $YBa_2Cu_3O_{7-\delta}$ thin films: Determination of oxygen content from x-ray diffraction patterns. *Physical Review B*. 48 (10). 1993.

[52] Benzi, P., Botizzo, E., Rizzi, N. Oxygen determination from cell dinensions in YBCO superconductors. *Journal of Crystal Growth*. 269. Pages 625-629. 2004.

[53] Poulsen, H. F., Andersen, N. H. and Lebech, B. Twin-domain size and bulk oxygen in-diffusion kinetics of $YBa_2Cu_3O_{6+x}$ studied by neutron powder diffraction and gas volumetry. *Physica C*. 173. Pages 387-397. 1991.

[54] LaGraff, J. R. and Payne, D. A. Concentration-dependent oxygen diffusivity in $YBa_2Cu_3O_{6+x}$. III. Diffusion mechanisms. *Physica C*. 212. Pages 487-496. 1993.

[55] Kläser, M., Kaiser, J., Stock, F., Müller-Vogt, G., Erb, A. Comparative study of oxygen diffusion in rare earth $REBa_2Cu_3O_{7-\delta}$ single crystals (RE=Y, Er, Dy) with different impurity levels. *Physica C*. 306. Pages 188-198. 1998.

[56] Diko, P., Kanuchova, M., Chaud, X., Odier, P., Granados, X., Obradords, X. Oxygenation mechanism of TSMG YBCO bulk superconductors. *Journal of Physics: Conference Series*. 97. Pages 012160. 2008.

[57] Salomons, E. and de Fontaine, D. Monte Carlo study of tracer and chemical diffusion of oxygen in $YBa_2Cu_3O_{6+2c}$. *Physical Review B*. 41 (16). Pages 11159-11167. 1990.

[58] Pekalski, A., Auslos, M. Monte Carlo simulation of oxygen diffusion in planar model of 123 YBCO. Low-temperature model and effect of trapping barrier. *Physica C*. 224. Pages 188-198. 1994.

[59] Choi, J.-S., Sarikaya, M., Aksay, I. A. and Kikuchi, R. Theory of oxygen diffusion in the $YBa_2Cu_3O_{7-x}$ compound. *Physical Review B*. 42 (7). Pages 4244-4254. 1990.

[60] Aarnink, W. A. M., Ijsselstejn, R. P., Gao, J., van Silfhont, A. and Rogalla, H. Oxygen transport in c-axis-oriented high-T_c superconducting $YBa_2Cu_3O_{7-\delta}$ thin films, studied by in-situ ellipsometry. *Physical Review B*. 45 (22). Pages 13002-13007. 1992.

[61] Chen, L., Chen, C. L. and Jacobson, A. J. Electrical Conductivity relaxation Studies of Oxygen Transport in Epitaxial $YBa_2Cu_3O_{7-\delta}$ Thin Films. *IEEE Transactions on Applied Superconductivity*. 13 (2). Pages 2882-2885. 2003.

[62] Cayado, P., Sanchez-Valdes, C. F., Stangl, A., Coll, M., Roura, P., Palau, A., Puig, T. and Obradors, X. Untagling surface oxygen exchange effects in $YBa_2Cu_3O_{6+x}$ thin films by electrical conductivity relaxation. *Physical Chemistry Chemical Physics*. 19. Pages 14129-14140. 2017.

[63] Chikumoto, N., Machi, T., Tokunaya, Y., Izumi, T., Tajima, S. Optimization of oxygenation process in YBCO tapes fabricated by TFA-MOD method. *Physica C*. 426-431. Pages 1118-1121. 2005.

[64] Iida, K., Babu, N. H., Shi, Y. and Carduell, D. A. Seeded infiltration and growth of single-domain Gd-Ba-Cu-O bulk superconductors using a generic seed crystal. *Superconductor Science and Technology*. 19. Pages 1478-1485. 2006.

[65] Abrikosov, A. A. On the magnetic properties of superconductors of the second group. *Soviet Physics-Journal of Experimental and Theoretical Physics*. 5. Pages 1174-1182. 1957.

[66] Schmidt, V. V. The physics of superconductors. 1997. Springer Berlin, Heidelberg.

[67] Matsushita, T. Flux Pinning in Superconductors. 2014. Springer Series in Solid-State Sciences 178.

[68] Sharma, R. G. Superconductivity. 2021. Springer Series in Materials Science 214.

[69] Mangin, P., Kahn, R. Superconductivity. 2017. Springer.

[70] Blatter, G., Feigel'man, M. V., Geshkenbein, V. B., Larkin, A. I., Vinokur, V. M. Vortices in high-temperatures superconductors. *Reviews of Modern Physics*. 66 (4). Pages 1125-1388. 1994.

[71] Bean, C. P. Magnetization of Hard Superconductors. *Physical Review Letters*. 8 (6). Pages 250-253. 1962.

[72] Dew-Hughes, D. Flux pinning mechanism in type II superconductors. *Philosophical Magazine*. 30 (2). Pages 293-305. 1974.

[73] Crisan, A. Vortices and Nanostructured Superconductors. 2017. Springer Series in Materials Science 261.

[74] Pan, V.M., Pan, A.V. Vortex matter in superconductors. *Low Temperature Physics*. 27. Pages 732-746. 2001.

[75] Pan., V., Cherpak, Y., Komashko, V., Pozigin, S., Tretiatchenko, C., Semenov, A., Pashitskii, E., Pan, A. V. Supercurrent transport in YBa2Cu3O7-δ epitaxial thin films in a dc magnetic field. *Physical Review B*. 73. Pages 054508. 2006.

[76] Pan, A.V., Pysarenko, S. V. and Dou, S.X. Quantitative Description of Critical Current Density in YBCO films and Multilayers. *IEEE Transactions on Applied Superconductivity*. 19(3). Pages 3391-3394. 2009.

[77] Golovchanskiy, I. A., Pan, A. V., Shcherbakova, O. V., Fedoseev, S. A. and Dou, S. X. An all-field-range description of the critical current density in superconducting YBCO films. *Superconducting Science and Technology*. 24. Pages 105020. 2011.

[78] Pennycook, S. J., Chisholm, M. F., Jesson, D. E., Feenstra, R., Zhu, S., Zheng, X. Y. and Lowndes, D. J. Growth and relaxation mechanisms of $YBa_2Cu_3O_{7-\delta}$ films. *Physica C*. 202. Pages 1-11. 1992.

[79] Svetchnikov, V., Pan, V., Traeholt, C. and Zandbergen, H. Formation Of Edge Dislocations in Thin Epitaxial YBCO Films. *IEEE Transactions on Applied Superconductivity*. 7(2). Pages 13961398. 1997.

[80] Held, R., Schneider, C. W., Manhart, J., Allard, L. F., More, K. L. and Goyal, A. Low-angle grain boundaries in $YBa_2Cu_3O_{7-\delta}$ with high critical current densities. *Physical Review B*. 79. Pages 014515. 2009.

[81] Pan, V. M., Flis, V. S., Karasevska, O. P., Matsui, V. I., Peshko, I. I., Svetchnikov, V. L., Lorenz, M., Ivanyuta, A. N., Melkov, G. A., Pashitskii, E. A. and Zandbergen, H. W. Effect of Growth-Induced Linear Defects on High Frequency Properties of Pulse-Laser Deposited $YBa_2Cu_3O_{7-\delta}$ Films. *Journal of Superconductivity:Incorporating Novel Magnetism*. 14(1). 2001.

[82] Selvamanickam, V., Mironova, M., Son, S. and Salama, K. Flux pinning by dislocations in deformed melt-textured $YBa_2Cu_3O_x$ superconductors. *Physica C*. 208. PAges 238-244. 1993. ges 067009. 2004.

[83] Golovchanskiy, I. A., Pan, A. V., Fedoseev, S. A., Higgins, M. Significant tunability of thin films functionalities enabled by manipulating magnetic and structural nano-domains. *Applied Surface Science*. 311. Pages 549-557. 2014.

[84] Blatter, G., Geshkenbein, V. B. and Koopmann, J. A. G. Weak to strong pinning. *Physical Review Letters*. 92 (6). Pages 067009. 2004.

[85] Obradors, X. and Puig, T. Coated conductors for power applications: materials challenge. *Superconductor Science and Technology*. 27. Pages 044003. 2014.

[86] Feighan, J. P. F., Kursumovic, A. and MacManus-Driscoll, J. L. Materials design for artificial pinning centers in superconductor PLD coated conductors. *Superconductor Science and Technology*. 30. Pages 123001. 2017.

[87] Horide, T., Kawamura, T., Matsumoto, K., Ichinose, A., Yoshizumi, M., Izumi, T. and Shiohara, Y. J_c improvement by double artificial pinning centers of $BaSnO_3$ and Y_2O_3 nanoparticles in $YBa_2Cu_3O_7$ coated conductors. *Superconductor Science and Technology*. 26. Pages 075019. 2013.

[88] Ko, K.-P., Choi, S.-M., Lee, J.-W., Ko, R.-K., Moon, S.-H., Park, C. and Yoo, S.-I. Optimization of the $BaSnO_3$ Doping Content in $GdBa_2Cu_3O_{7-\delta}$ Coated Conductors by Pulsed Laser Deposition. *IEEE Transaction on Applied Superconductivity*. 24 (66). Pages 6600908. 2014.

[89] Horide, T., Taguchi, K., Matsumoto, K., Matsukida, N., Ishimaru, M., Mele, P. and Kita, R. Influence of matching field on critical current density and irreversibility temperature in $YBa_2Cu_3O_7$ films with $BaMO_3$ (M=Zr, Sn, Hf) nanorods. *Applied Physics Letters*. 108. Pages 082601. 2016.

[90] Kang, B., Tran, D. H., Kang, W. N. Scaling of pinning forces in $BaSnO_3$-added $GdBa_2Cu_3O_{7-x}$ superconducting thin films. *Thin Solid Films*. 624. Pages 16-20. 2017.

[91] Erbe, M., Hänisch, J., Hühne, R., Freudenberg, T., Kirchner, A., Molina-Luna, L., Damm, C., Van Tendeloo, G., Kakel, S., Schultz, L. and Holzapfel, B. $BaHfO_3$ artificial pinning centers in TFA-MOD-derived YBCO and GdBCO thin films. *Superconductor Science and Technology*. 28. Pages 114002. 2015.

[92] Awaji, S., Yoshida, Y., Suzuki, T., Watanabe, K., Hikawa, K., Ichino, Y. and Izumi, T. High-performance irreversibility field and flux pinning force density in $BaHfO_3$ doped $GdBa_2Cu_3O_y$ tape prepared by pulsed laser deposition. *Applied Physics Express*. 8. Pages 023101. 2015.

[93] Horide, T., Kametano, F., Yoshioka, S., Kitamura, T. and Matsumoto, K. Structural Evolution Induced by Onterfacial Lattice Mismatch in Self-Organized $YBa_2Cu_3O_{7-\delta}$ Nanocomposite Films. *ACS Nano*. 11. Pages 1780-1788. 2017.

[94] Cayado, P., Erbe, M., Kauffmann-Weiss, S., Bühler, C., Jung, A., Hänisch, J. and Holzapfel, B. Large critical current densities and pinning forces in CSD-grown superconducting $GdBa_2Cu_3O_{7-x}$-$BaHfO_3$ nanocomposite films. *Superconductor Science and Technology*. 30. Pages 094007. 2017.

[95] Matsumoto, K., Nishihara, M., Kimoto, T., Horide, T., Jha, A. K., Yoshida, Y., Awaji, S. and Ichinose, A. Temperature dependence of critical currents on REBCO thin films with aprtificial pinning centers. *Superconductor Science and Technology*. 30. Pages 104006. 2017.

[96] Maeda, T., Kaneko, K., Yamada, K., Roy, A., Sato, Y., Teranishi, R., Kato, T., Izumi, T., Shiohara, Y. Nanostructural characterization of artificial pinnign centers in PLD-processed $REBa_2Cu_3O_{7-\delta}$ films. *Ultramicroscopy*. 176. Pages 151-160. 2017.

[97] Kato, T., Sasaki, H., Gotoh, Y., Hirayama, T., Takahashi, K., Konishi, M., Kobayashi, H., Ibi, A., Muroga, T., Miyata, S., Watanabe, T., Yamada, Y., Izumi, T., Shiohara, Y. Nanosctuctural characterization of Y123 and Gd123 with $BaZrO_3$ rods fabricated by pulsed-laser deposition. *Physica C*. 445-448. Pages 628-632. 2006.

[98] Palau, A., Bartolome, E., Llordes, A., Puig, T. and Obradors, X. Isotropic and anisotropic pinning in TFA-grown $YBa_2Cu_3O_{7-x}$ films with $BaZrO_3$ nanoparticles. *Superconductor Science and Technology*. 24. Pages 124010. 2011.

[99] Goyal, A. and Wee, S. H. Optimal Nanodefect Configurations via Strain-Mediated Assembly for Optimized Vortex-Pinning Superconductong Wires from 5-77 K. *Journal of Physics: Conference Series*. 871. Pages 012039. 2017.

[100] Gharahcheshmeh, M. H., Galstyan, E., Xu, A., Kukunura, J., Katta, R., Zhang, Y., Majkic, G., Li, X.-F. and Selvamanickam, V. Superconducting transition width (ΔT_c) characteristics of 25mol% Zr-added (Gd, Y)$Ba_2Cu_3O_{7-\delta}$ superconducting tapes with high in-field critical current density at 30 K. *Superconductor Science and Technology*. 30. Pages 015016. 2017.

[101] Haruta, M., Fujita, N., Maeda, T., Horu, S. Influence of deposition temperature on critical current properties for Nd:YAG-PLD-$YBa_2Cu_3O_y$ thin films with nanorods. *Physics Procedia*. 36. Pages 1576-1581. 2012.

[102] Rizzo, F., Augeri, A., Armenio, A. A., Galuzzi, V., Mancini, A., Pinto, V., Rufoloni, A., Vannozzi, A., Bianchetti, M., Kursumovic, A., MacManus-Driscoll, J. L., Meledin, A., Van Tenderloo, G. and Celentano, G. Enhanced 77 K vortex-

pinning in $YBa_2Cu_3O_{7-x}$ films with Ba_2YTaO_6 and mixed Ba_2YTaO_6+Ba_2YNbO_6 nano-columnar inclusions with irreversibility field to 11 T. *APL Materials*. 6. Pages 061101. 2016.

[103] Opherden, L., Sieger, M., Pahlke, P., Hühne, R., Schultz, L., Meledin, A., Van Tenderloo, G., Nast, R., Holzapfel, B., Bianchetti, M., MacManus-Driscoll, J. L. and Hänisch, J. Large pinning forces and matching effects in $YBa_2Cu_3O_{7-\delta}$ thin films with $Ba_2Y(Nb/Ta)O_6$ nano-precipitates. *Scientific Reports*. 6. Pages 21188. 2016.

[104] Gapud, A. A., Kumar, D., Viswanathan, Cantoni, C., Varela, M., Abiade, J., Pennycook, S. J. and Christen, D. K. Enhancement of flux pinning in $YBa_2Cu_3O_{7-\delta}$ thin films embedded with epitaxially grown Y_2O_3 nanostructures using a multilayering process. *Superconductor Science and Technology*. 18. Pages 1502-1505. 2005.

[105] Campbell, T. A., Haugan, T. J., Martense, J., Murphy, J., Brukke, L., Barnes, P. N. Flux pinning effects of Y_2O_3 nanoparticulates dispersions in multilayered YBCO thin films. *Physica C*. 423. Pages 1-8. 2005.

[106] Tran, D. H., Putri, W. B. K., Wie, C. H., Kang, B., Lee, N. H., Kang, W. N., Lee, J. Y., Seong, W. K. Enhanced critical current density in $GdBa_2Cu_3O_{7-\delta}$ thin films with substrate surface decoration using Gd_2O_3 nanoparticles. *Thin Solid Films*. 526. Pages 241-245. 2012.

[107] Mele, P., Guzman, R., Gazquez, J., Puig, T., Obradors, X., Saini, S., Yoshida, Y., Mukaida, M., Ichinose, A., Matsumoto, K. and Adam, M. I. High pinning performance of $YBa_2Cu_3O_{7-x}$ films added with Y_2O_3 nanoparticulate defects. *Superconductor Science and Technology*. 28. Pages 024062. 2015.

[108] Oh, W.-J., Kim, J.-E. and Yoo, S.-I. Enhanced Pinning Properties of $GdBa_2Cu_3O_{7-\delta}$ Films With the Gd_2O_3 Nanoparticles. *IEEE Transactions on Applied Superconductivity*. 27 (4). Pages 8000605. 2017.

[109] Jha, A. K., Matsumoto, K., Horide, T., Saini, S., Mele, P., Ichinose, A., Yoshida, Y. and Awaji, S. Isotropic enhancement in the critical current density YBCO thin films incorporating nanoscale Y_2BaCuO_5 inclusions. *Journal of Applied Physics*. 122. Pages 093905. 2017.

[110] Chen, S., Sebastian, M. A., Gautam, B., Wilt, J., Haugan, T., Xing, Z. and Wu, J. Enchancement of Isotropic Pinning Force in YBCO Films With $BaZrO_3$ Nanorods and Y_2O_3 Nanoparticles. *IEEE Transactions on Applied Superconductivity*. 27 (4). Pages 8000205. 2017.

[111] Smith, H. M. and Turner, A. F. Vacuum Deposited Thin Films Using a Ruby Laser. *Applied Optics*. 4 (1). Pages 147-148. 1964.

[112] Lowndes, D. H., Geohegan, D. B., Puretzky, A. A., Norton, D. P., Rouleau, C. M. Synthesis of Novel Thin-Film Materials by Pulsed Laser Deposition. *Science*. 273. Pages 898-903. 1996.

[113] Singh, R. K., Biunno, N. and Narayan, J. Microstructural and compositional variations in laser-deposited superconducting thin films. *Applied Physics Letters*. 53. Pages 1013-1015. 1988.

[114] Schou, J. Physical aspects of the pulsed laser deposition technique: The stoichiometric transfer of material from target to film. *Applied Surface Science*. 255. Pages 5191-5198. 2009.

[115] Singh, R. K. and Narayan, J. Pulsed-laser evaporation technique for deposition of thin films: Physics and theoretical model. *Physical Review B*. 41 (13). Pages 8843-8859. 1990.

[116] Burger, J., Lippert, M., Dorsch, W., Bauer, P., Saemann-Ischenko, G. Observation of the early stages of growth and the formation of growth spirals in epitaxial $YBa_2Cu_3O_{7-\delta}$ thin films by AFM. *Applied Physics A*. 58. Pages 49-56. 1994.

[117] Wu, K. H., Wang, R. C., Chen, S. P., Lin, H. C., Juang, J. Y., Uen, T. M. and Gou, Y. S. Preparation of large area and investigation of initial film growth if $YBa_2Cu_3O_7$ by scanning pulsed laser deposition. *Applied Physics Letters*. 49. Pages 421-421. 1996.

[118] Eulenberg, A., Romans, E. J., Fan, Y. C., Pegrum, C. M. Pulsed laser deposition of $YBa_2Cu_3O_{7-\delta}$ and $NdBa_2Cu_3O_{7-\delta}$ thin films: a comparative study. *Physica C*. Pages 91-104. 1999.

[119] Kusumori, T. and Muto, H. Preparation of thin epitaxial YBCO films by ablation using fourth harmonic of Nd:YAG laser. *Physica C*. 282-287/ Pages 577-578. 1997.

[120] Kim, S.-M., Lee, S. Y. Characterization of YBCO superconducting thin films fabricated by pulsed laser deposition. *Thin Solid Films*. 355-356. Pages 461-464. 1999.

[121] Ono, I., Ichino, Y., Yoshida, Y., Yoshizumi, M., Izumi, T., Shiohara, Y. High-material yield fabrication of YBCO coated conductors by Nd:YAG-PLD system. *Physics Procedia*. 27. Pages 216-219. 2012.

[122] Horii, S., Fujita, N., Ogura, Y., Maeda, T., Haruta. Fabrication and critical current properties in Nd:YAG-P:D $REBa_2Cu_3O_y$ (RE=Y and Er) thin films. *Physics Procedia*. 27. Pages 220-223. 2012.

[123] Koren, G., Gupta, A., Baseman, R. J., Lutwyche, M. I. and Laibowitz, R. B. Laser wavelength dependent properties of $YBa_2Cu_3O_{7-\delta}$ thin films deposited by laser ablation. *Applied Physics Letters*. 55. Pages 2450-2452. 1989.

[124] Dam, B., Rector, J., Chang, M. F., Kars, S., de Groot, D. G. and Griessen, R. Laser ablation threshold of $YBa_2Cu_3O_{6+x}$. *Applied Physics Letters*. 65. Pages 1581-1583. 1994.

[125] Kim, H. S. and Kwok, H. S. Correlation between target-substrate distance and oxygen pressure in pulsed laser deposition of $YBa_2Cu_3O_7$. *Applied Physics Letters*. 61. Pages 2234-2236. 1992.

[126] Nelson, J. B. and Riley, D. P. An experimental investigation of extrapolation methods in the derivation of accurate unit-cell dimensions of crystals. *IOP Science*. Pages 160-177. 1945.

[127] Scherrer, P. Bestimmung der Grösse und der inneren Struktur von Kolloidteilchen mittels Röntgenstrahlen. 26. Pages 98-110. 1918.

[128] Matsumoto, K., Takahara, D., Horide, T., Ichinose, A., Horii, S., Yoshida, Y., Mukaida, M. and Osamura, K. High-J_c Gd-Ba-Cu-O Epitaxial Films Prepared by Pulsed Laser Depostion. *IEEE Transactions on Applied Superconductivity*. 15 (2). Pages 2719-2722. 2005.

[129] DeVero, J. C., Lee, D., Shin, H., Namuco, S. B., Hwang, I., Sarmago, R. V. and Song, J. H. Influence of deposition conditions on growth of micron-thick highly c-axis textured superconducting $GdBa_2Cu_3O_{7-\delta}$ films on $SrTiO_3$ (100). *Journal of Vacuum Science and Technology A.* 36. Pages 031506. 2018.

[130] Miyachi, K., Sudoh, K., Ichino, Y., Yoshida, Y., Takai, Y. The effect of the substitution Gd for Ba site on $Gd_{1+x}Ba_{2-x}Cu_3O_{6+\delta}$ thin films. *Physica C*. 392-396. Pages 1261-1264. 2003.

[131] Erbe, M., Cayado, P., Freitag, W., Ackermann, K., Langer, M., Meledin, A., Hänisch, J. and Holzapfel, B. Comparative study of CSD-grown REBCO films with different rare earth elements: processing windows and T_c. *Superconductor Science and Technology*. 33. Pages 094002. 2020.

[132] Rosenzweig, St., Hänisch, J., Hühne, R., Holzapfel, B. and Schultz, L. T_c Optimization of $GdBa_2Cu_3O_7$ Thin Films Grown by Pulsed Laser Deposition. *Journal of Physics: Conference Series*. 234. Pages 012035. 2010.

[133] Misra, D. S. and Palmer, S. B. Laser ablated thin films of $YBa_2Cu_3O_{7-\delta}$: the nature and origin of the particulates. *Physica C*. 176. Pages 43-48. 1991.

[134] Suh, J. P. and Sung, G. Y. Behavior of the droplets ejecting from the YBCO target during the pulsed laser deposition. *Physica C*. 235-240. Pages 571-572. 1994.

[135] Suh, J. D., Sung, G. Y. and Kang, K. Y. Influence of the Deposition Rate on Crystalline Structure and Cation Disordering of YBCO Thin Films. *IEEE Transactions on Applied Superconductivity*. 9 (2). 1999.

[136] El-Astal, A. H., Morrow, T., Graham, W. G. and Walmsley, D. G. The role of gas-phase oxidation and combination during laser deposition of $YBa_2Cu_3O_{7-x}$ in ambient oxygen. *Superconductor Science and Technology*. 8. Pages 529-533. 1995.

[137] Low, B. L., Xu, S. Y., Ong, C. K., Wang, X. B. and Shen, Z. X. Substrate temperature dependence of the texture quality in YBCO thin films fabricated by on-axis pulsed-laser ablation. *Superconductor Science and Technology*. 10. Pages 41-46. 1997.

[138] Shi, J. J. and Wu, J. Micromechanical model for self-organized secondary phase oxide nanorod arrays in epitaxial $YBa_2Cu_3O_{7-\delta}$ films. *Philosophical Magazine*. 92 (23). Pages 2911-2922. 2012.

[139] Ichino, Y., Yoshida, Y. and Miura, S. Three-dimensional Monte carlo simulation of nanorod self-organization in $REBa_2Cu_3O_y$ thin films grown by vapor phase epitaxy. *Japanese Journal of Applied Physics*. 56. Pages 015601. 2017.

[140] Cantono, C., Gao, Y., Wee, S. H., Specht, E. D., Gazquez, J., Meng, J., Pennycook, S. J. and Goyal, A. Strain-Driven Oxygen Deficiency in Self-Assembled Nanostructured Composite Oxide Films. *ACS Nano*. 5 (6). Pages 4783-4789. 2011.

[141] Palonen, H., Jäykka, J. and Paturi, P. Modeling reduced field dependence of critical current density in $YBa_2Cu_3O_{6+x}$ films with nanorods. *Physical Review B*. 85. 024510. 2012.

[142] Paturi, P., Malmivirta, M., Hynninen, T. and Huhtinen, H. Angle dependent molecular dynamics simulation of flux pinning in YBCO superconductors with artificial pinning centers. *Journal of Physics: Condensed Matter*. 30. Pages 315902. 2018.

[143] Xu, A., Braccini, V., Jaroszynski, J., Xin, Y. and Larbalestier, D. C. Role of weak uncorrelated pinning introduced by $BaZrO_3$ nanorods at low-temperature in (Y, Gd)$Ba_2Cu_3O_x$ thin films. *Physical Review B*. 86. Pages 115416. 2012.

[144] Aye, M. M., Khan, M. Z., Rivasto, E., Tikkanen, J., Huhtinen, H. and Paturi, P. Role of Columnar Defect Size in Angular Dependent Flux Pinning Properties of YBCO Thin Films. *IEEE Transactions on Applied Superconductivity*. 29 (5). Pages 8006805. 2019.

[145] Lindemer, T. B., Washburn, F. A., MacDougall, C.S., Feenstra, R. and Cavin, O. B. Decomposition of $YBa_2Cu_3O_{7-x}$ and Y248 for $pO_2 \leq 0.1$ MPa. *Physica C*. 178. Pages 93-104. 1991.

[146] Oh, W.-J., Park, I., Chung, K., Lee, J.-H., Moon, S.-H. and Yoo, S.-I. Effect of post-annealing on the pinning properties of $GdBa_2Cu_3O_{7-\delta}$ coated conductors prepared by RCE-DR. *Superconductor Science and Technology*. 33. Pages 085007. 2020.

[147] Shiomi, M., Ichino, Y., Tsuchiya, Y., Ichinose, A. and Yoshida, Y. Improvement of anisotropy of superconducting properties in Y-rich $YBa_2Cu_3O_y$ films in magnetic fields. *Journal of Physics: Conference Series*. 1293. Pages 012030. 2019.

[148] Pan, A. V., Golovchanskiy, I. A. and Fedoseev, S. A. Critical current density: Measurements vs. reality. *A Letters Journal Exploring the Frontiers of Physics*. 103. Pages 17006. 2013.

.

Publications

[1] Popov, R., Erbe, M., Hänisch, J., Holzapfel, B. Superconducting $BaHfO_3$-$GdBa_2Cu_3O_7$ nanocomposite Thin Films: Influence of Growth Temperature and Deposition Rate on Transport Properties. *IEEE Transactions on Applied Superconductivity*. 29(5). Pages 1-5. 2019.

[2] Popov, R., Ackermann, K., Rijckaert, H., Hänisch, J., Van Driessche, I., Holzapfel, B. Effect of oxygenation process on flux pinning in pristine and $BaHfO_3$ nanocomposite $GdBa_2Cu_3O_7$ superconducting thin films. *Journal of Physics: Conference series*. 1559. Pages 012038. 2020.

[3] Popov, R., Cayado, P., Grünewald, L., Rijckaert, H., Hänisch, J., Gerthsen D., Holzapfel, B. Dependence of microstructure and transport properties of PLD-grown $GdBa_2Ba_3O_{7-\delta}$ superconducting thin films on oxygenation procedure. *Manuscript in preparation.*

[4] Grünewald, L., Nerz, D., Langer, M., Meyer, S., Beisig, N., Cayado, P., Popov, R., Hänisch, J., Holzapfel, B. and Gerthsen, D. Analysis of superconducting thin films in a modern FIB/SEM dual-beam instrument. *Microscopy and Microanalysis*. 27. Supplement S1. Pages 1056-1058. 2021.

International conferences

[1] Popov, R., Holzapfel, B., Hänisch, J. Inlfuence of growth temperature and oxygen pressure on transport properties of BHO-doped *RE*BCO(*RE*=Y, Gd) superconducting thin films. *European Conference on Applied Superconductivity 2017*. Geneva, Switzerland. September 17-21. Page 133.

[2] Popov, R., Holzapfel, B., Hänisch, J. $BaHfO_3$-doped GdBCO superconducting thin films: Influence of dopant amount and growth temperature on transport properties. *Applied Superconductivity Conference 2018*. Seattle, Washington, USA. October 28-November 2. Page 132.

[3] Popov, R., Ackermann, K., Holzapfel, B., Hänisch, J., Flux pinning in $BaHfO_3$ and $Ba_2Gd(Nb,Ta)O_6$ nanocomposite $GdBa_2Cu_3O_7$ thin films. *European Conference on Applied Superconductivity 2019*. Glasgow, UK. September 1-5. Page 83.